Monopile foundation modeling in the frequency domain for Offshore Wind Turbines

V.S. Huigen

TU Delft

SIEMENS Gamesa
RENEWABLE ENERGY

Cover photo: Ocean Energy Resources

Monopile foundation modeling in the frequency domain for Offshore Wind Turbines

V.S. Huigen

A thesis presented for the degree of
Master of Science

Structural Engineering
Department of Civil Engineering and Geosciences
TU Delft
The Netherlands
To be defended publicly on July 20th, 2021

Graduation committee:

Dr. ir. K.N. van Dalen	TU Delft - Chair
Prof. dr. ir. A.V. Metrikine	TU Delft
Ir. A.B. Fărăgău	TU Delft
Dr. J. Zhang	TU Delft
Dr. ir. F.P. van der Meer	TU Delft
Ir. S. Panagoulias	Siemens Gamesa Renewable Energy and TU Delft
Dr. ir. W.G. Versteijlen	Siemens Gamesa Renewable Energy

TU Delft

SIEMENS Gamesa
RENEWABLE ENERGY

Abstract

The offshore wind industry is a quickly growing market because the increasing demand for clean energy sources. Large wind speeds and the abundance of potential wind farm locations make Offshore Wind Turbines an interesting solution. Because of high continuous dynamic loading and extreme environmental conditions, the structural design requires a detailed assessment, especially in the Fatigue Limit State. In this thesis, the focus lies on improving the modeling of monopile foundations for Offshore Wind Turbines, which could pave the way towards more efficient foundation design.

The conventional method of modeling the monopile foundation of an Offshore Wind Turbine is with a nonlinear elastic distributed spring stiffness along the monopile (using p-y curves). Damping related to the soil is considered through either global damping (like Rayleigh damping) or local viscous damping. However, the response of the soil around the monopile under wind and wave loading is better described through a nonlinear hysteretic (rate-independent) model, which is computationally demanding to model in the time domain. Next to that, a conventional frequency-domain method can not be combined with any nonlinearity. Therefore, linear elastic models are used to model the soil response in frequency-domain simulations.

The goal of this thesis is to combine a nonlinear hysteretic soil model with a frequency-domain analysis. Firstly, a nonlinear hysteretic element is assessed in 1 Degree of Freedom through a nonlinear frequency-domain algorithm. Results under harmonic loading match a nonlinear time-integration. However, an analysis of the complexity of the algorithm shows that the method is computationally challenging to extend to a large Finite Element model under multiharmonic loading. A simplification of the strategy is needed. Therefore, a response amplitude-dependent linearization of the nonlinear hysteretic element is made. This linearization captures both the secant stiffness and the hysteretic damping ratio of the generated hysteresis loops. The combination of the response amplitude-dependent element with an iterative solution strategy, the Equivalent Linear method, is shown to approximate a nonlinear time-integration under both harmonic and multiharmonic loading, as long as the nonlinearity is limited. Because of the linearization, this Equivalent Linear method is able to be extended to a large Finite Element model under multiharmonic loading.

A nonlinear hysteretic model is fit to available soil reaction data and a response amplitude-dependent linearization is generated. A Finite Element model that can be combined with the Equivalent Linear method is set up and verified with a case study structural model of an Offshore Wind Turbine. The model is subjected to (high) Fatigue Limit State wave loading. The results are compared to both a conventional frequency-domain method (with a linear elastic small-strain soil model) and a nonlinear time-domain method (with a nonlinear elastic soil model). The deflections and deflection spectra in the foundation found through the Equivalent Linear method correspond to results from the nonlinear time-domain method, provided the influence of higher harmonics is limited and the response has a similar amplitude throughout the analyzed time window.

Results from the Equivalent Linear method show that the main frequency of the first resonance peak is around 2% smaller than the first natural frequency of the system. This shifted resonance peak is consistent with the results found through the nonlinear time-domain method. Because of the local response amplitude-dependent hysteretic damping applied however, an increase of the soil damping is identified from the results of the Equivalent Linear method. The identified soil damping in the first mode is 0.64-0.8% critical (4-5% log. dec.), which is similar to other literature. By combining the observed system properties with literature about fatigue damage estimation, a hypothesis is stated: the fatigue damage in the foundation calculated through an Equivalent Linear method with a nonlinear hysteretic soil model will be lower than the fatigue damage calculated through a nonlinear time-domain method with a nonlinear elastic soil model.

Acknowledgements

I would like to thank the following people for their great support during this Master thesis. First of all, I would like to thank the committee members. Karel van Dalen, Andrei Metrikine, Pim Versteijlen and Frans van der Meer, thank you for your helpful comments during the progress meetings, and for helping me place the thesis into context with other current research. I want to also express my gratitude to my daily supervisors from the TU Delft, Andrei Fărăgău and Jiangyi Zhang. Thank you for your support and guidance during our meetings, the in-depth discussions we had in these meetings helped to make sense of all the Matlab code. I highly value your continued support throughout the entire project, even though we have only met through a computer screen.

Special thanks to my daily supervisor form Siemens Gamesa Renewable Energy, Stavros Panagoulias. Thank you for our weekly meetings, which were very helpful in structuring the project and keeping focus on the end goals. Your incredible knowledge about soil mechanics and design practice in the wind industry helped me a lot in the thesis as well. I would like to also thank other people from Siemens Gamesa Renewable Energy. Axel Nernheim, Sebastian Schafhirt and Matthias Brommundt, thank you for your support in the project by executing some of the simulations and providing the input data. Colinda Rog, thank you for being there for the students and interns of SGRE. I really enjoyed our conversations at the SGRE office. Aude Péchadre, thank you for our conversations as well, it was very nice to have you as a 'compagnon' during the thesis.

Finally, I want to thank my friends and family for their support this past year. Your support kept me going through the difficult period of doing a Master thesis in the middle of a global pandemic. Thank you for listening to me venting about the project, and for listening to me talk about algorithms and differential equations all the time.

Vincent Huigen
Delft, July 2021

Nomenclature

Latin symbols

A	Cross-sectional area	[m^2]
$\hat{a}/\hat{\mathbf{a}}$	Fourier coefficient of $\mathbf{f}$ (cosine)	[N] / [Nm]
$\mathbf{B}$	1st derivative of the shape function matrix $\mathbf{N}$	-
$\hat{b}/\hat{\mathbf{b}}$	Fourier coefficient of $\mathbf{f}$ (sine)	[N] / [Nm]
$\mathbf{C}$	Linear damping matrix	-
c	Viscous damping	[Ns/m]
$\hat{c}/\hat{\mathbf{c}}$	Fourier coefficient of $\mathbf{u}$ (cosine)	[m] / [rad]
D	Hysteretic damping ratio	-
$\hat{d}/\hat{\mathbf{d}}$	Fourier coefficient of $\mathbf{u}$ (sine)	[m] / [rad]
E	Young's Modulus	[N/m^2]
f/$\mathbf{f}$	Force	[N] / [Nm]
f_0	1st natural frequency of the structure	[Hz]
G	Shear modulus	[N/m^2]
$\mathbf{H}$	Dynamic compliance matrix	-
H	Amount of harmonics	-
h	Element length	[m]
$\mathbf{I}$	Identity matrix	-
I	Second moment of area	[m^4]
$\mathbf{J}$	Jacobian	-
$\mathbf{K}$	Linear stiffness matrix	-
$\hat{\mathbf{K}}$	Complex-valued stiffness matrix	-
k	Stiffness (or distributed stiffness)	[N/m^2] /[N/m^3]
$\hat{k}$	Complex-valued stiffness (or distributed stiffness)	[N/m^2] /[N/m^3]
k	k-th harmonic	-
$\mathbf{M}$	Linear mass matrix	-
M	Samples taken in the time-domain part of AFTHBM	-
m	mass	[kg]
$\mathbf{N}$	Shape function matrix	-
N	Axial load on element	[N]
n	Hysteresis loop parameter Bouc-Wen	-
$\hat{p}/\hat{\mathbf{p}}$	Fourier coefficient of $\mathbf{z}$ (cosine)	[m] / [rad]
$\hat{q}/\hat{\mathbf{q}}$	Fourier coefficient of $\mathbf{z}$ (sine)	[m] / [rad]
R	Reaction force Bouc-Wen	[N]
$r/\mathbf{r}$	Residual function Bouc-Wen	[m] / [rad]
$\mathbf{S}$	Spectrum	-
T	Length of time window	[s]
$t/\mathbf{t}$	Time	[s]
$u/\mathbf{u}$	Displacement	[m] / [rad]
$\dot{u}/\dot{\mathbf{u}}$	Velocity	[m/s] / [rad/s]
$\ddot{u}/\ddot{\mathbf{u}}$	Acceleration	[m/s^2] / [rad/s^2]
$\hat{v}/\hat{\mathbf{v}}$	Fourier coefficient of $\mathbf{r}$ (cosine)	[m] / [rad]
$\hat{w}/\hat{\mathbf{w}}$	Fourier coefficient of $\mathbf{r}$ (sine)	[m] / [rad]
$z/\mathbf{z}$	Hysteretic displacement	[m] / [rad]
z	Spatial coordinate	[m]
$\mathbf{0}$	Vector with all zeros	-
$\mathbf{1}$	Vector with all ones	-

Greek symbols

α	Ratio between post- and pre-yielding stiffness Bouc-Wen	-
β	Hysteresis loop parameter Bouc-Wen	-
γ	Hysteresis loop parameter Bouc-Wen	-
ϵ	Convergence criterion	-
ζ	Damping ratio	-
κ	Hysteresis loop parameter Bouc-Wen	-
ρ	unit weight	[kg/m^3]
ϕ	Regularization parameter LM-algorithm	-
Ω	Fundamental frequency	[rad/s]
Ω_e	Domain of finite element	[-]
ω	Frequency	[rad/s]
ω_0	1st natural frequency	[rad/s]
ω_1	Damped natural frequency	[rad/s]
$\check{\nabla}^{\mathbf{n}}$	n-th order derivative matrix	-

Superscripts

j	j-th iteration of the iterative algorithm	-
T	Transpose	
u	Deflection	
θ	Rotation	
$\hat{}$	Transformed to the frequency domain	

Subscripts

bb	Backbone
e	Element
ex	External
i	Initial
k	k-th harmonic
nl	Nonlinear
ref	Reference
s	Shear
y	yield

Abbreviations

AFTHBM	Alternating Frequency-Time Harmonic Balance Method
B-W	Bouc-Wen
BHawC	In-house nonlinear time-domain solver from SGRE
DFT	Discrete Fourier Transform
DOF	Degree of Freedom
EQL	Equivalent Linear
FE	Finite Element
FLS	Fatigue Limit State
HBM	Harmonic Balance Method
IDFT	Inverse Discrete Fourier Transform
LM	Levenberg-Marquardt
log. dec.	Logarithmic decrement
OWT	Offshore Wind Turbine
SGRE	Siemens Gamesa Renewable Energy
ULS	Offshore Wind Turbine

List of Figures

List of Tables

Contents

Section 1

Introduction

1.1 Offshore Wind Turbines

The wind energy industry is a growing market because of the increasing demand for renewable energy sources. One of the options for the placement of these wind turbines is offshore. Larger wind speeds and the abundance of potential offshore wind farm locations make Offshore Wind Turbines (OWTs) an interesting solution.

However, the offshore placement of these turbines does come with extra engineering challenges. High wind speeds, high wave loading and harsh environmental conditions bring the necessity for detailed structural assessment. Because the forcing frequencies of wind loading, wave loading and the blade passing frequencies (f_{1P} and f_{3P}) are close to the 1st natural frequency (f_0) of the structure, a dynamical analysis is necessary (see Figure 1.1). High loads also mean large strains are observed in the structure and in the surrounding soil. Therefore, nonlinearity must be taken into account in the analyses.

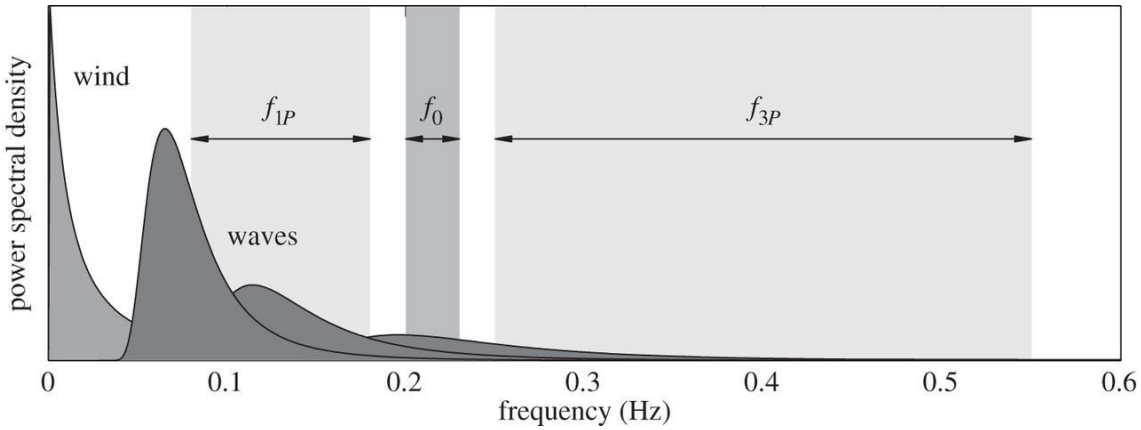

Figure 1.1: Relation of wave and wind loading spectra to f_0, f_{1P} and f_{3P}, [Kallehave et al., 2015].

2 load case groups are most important for OWT design: Ultimate Limit State (ULS) load cases and Fatigue Limit State (FLS) load cases. In ULS, one assesses the structure under extreme loading conditions. Under these extreme conditions, larger stresses and strains are allowed in the structure. Permanent deformations also occur in ULS load cases. In FLS, the behavior of the structure under regular conditions is observed. Continuous wind and wave loading will result in lower stresses and strains in the structure. Nonlinear behavior, although smaller, will still be present in FLS load cases. In this project, the focus lies on FLS analysis, as the fatigue lifetime is often a governing factor in the design of OWTs.

1.1.1 OWT support structures

Depending on site conditions, a big variety of support structures for OWTs can be used (see Figure 1.2). Because of the trend for sites to be situated further off the coast and the OWTs growing in power capacity and size, the sub-structures and foundations are growing as well. 81 % of the constructed OWTs in Europe have a monopile support structure ([Ramirez et al., 2020]). In this project we will investigate large-diameter monopile support structures. A schematization of an OWT on a monopile foundation along with some general definitions for a monopile support structure is shown in Figure 1.3.

The behavior of these monopile support structures is the subject of large research projects (like the PISA project [Byrne et al., 2017], the REDWIN project ([Aasen et al., 2017]) and the DISSTINCT project [Versteijlen et al., 2018])). Better understanding of the nonlinear dynamic behavior around these foundations allows for more efficient support structure design. The reason for this increase in efficiency is the possibility of less conservative assumptions for both the stiffness and the damping of the foundation. This efficiency will in turn allow for a stronger economic viability of Offshore Wind Energy.

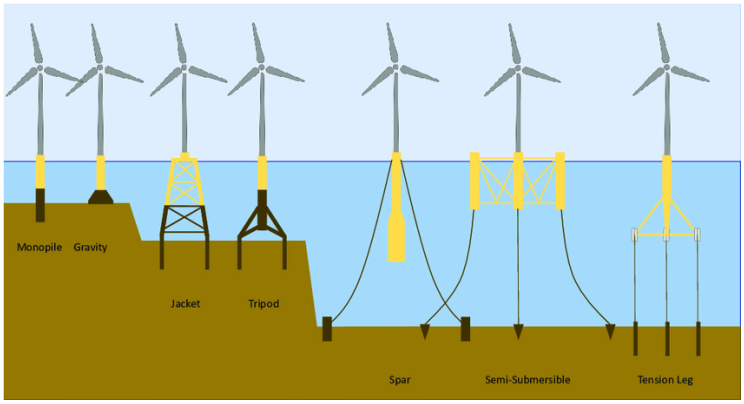

Figure 1.2: Different support structures for OWTs, [Dornhelm et al., 2019].

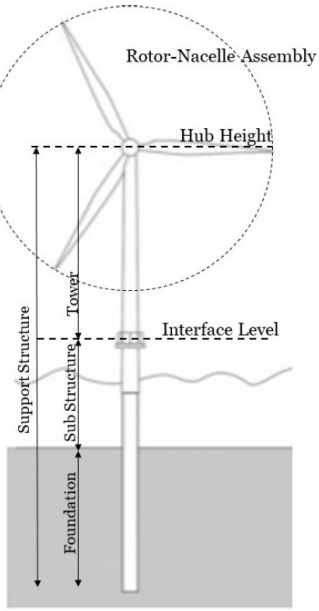

Figure 1.3: An Offshore Wind Turbine on a monopile foundation, [Hoogstraten, 2019].

1.2 Dynamical analysis

Dynamical analyses of complex structures like OWTs are generally carried out through a Finite Element Analysis (FEA). FEA is the process of discretizing a complex structure into smaller elements of which the approximate behavior is well defined. Such a discretization transforms the partial differential equations describing the system into a set of ordinary differential equations. In dynamical analysis, this system is described by the following formulation:

$$\mathbf{M} \cdot \ddot{\mathbf{u}}(t) + \mathbf{C} \cdot \dot{\mathbf{u}}(t) + \mathbf{K} \cdot \mathbf{u}(t) + \mathbf{f}_{nl}(t, \ddot{\mathbf{u}}, \dot{\mathbf{u}}, \mathbf{u}) = \mathbf{f}_{ex}(t) \tag{1.1}$$

with $\mathbf{M}$ being the (linear) mass matrix, $\mathbf{C}$ the (linear) damping matrix, $\mathbf{K}$ the (linear) stiffness matrix. In the case of added nonlinearities, an extra term of $\mathbf{f}_{nl}(t, \ddot{\mathbf{u}}, \dot{\mathbf{u}}, \mathbf{u})$ is added. Any nonlinear interaction in the system (like dry friction, slipping behavior, contact-dependency or hysteretic behavior) is summarized into this term. The system is excited by forces collected in $\mathbf{f}_{ex}(t)$. Displacements, velocities and accelerations of the system are represented by $\mathbf{u}(t)$,$\dot{\mathbf{u}}(t)$ and $\ddot{\mathbf{u}}(t)$.

1.2.1 Time-domain analysis

Two general families can be defined in solving systems of equations like Equation (1.1): Time-domain analyses and Frequency-domain analyses.

A Time-domain analysis starts off at a moment in time with predefined velocities and displacements in the structure. Based on the force at that moment in time, the accelerations, velocities and displacements at a next time-step is calculated. This procedure is repeated throughout the full time window. Elaborate time-stepping algorithms have been created to make sure an accurate solution is found. Next to that, this method can handle very complex (nonlinear) models. This accuracy and versatility does however come with relatively lengthy analyses. To ensure stability of the analysis, small time-steps are required at moments in time with large nonlinearities.

When analyzing the structural response of complex structures, analyses in the time domain can become too computationally costly. In the case of analyzing OWTs, analyses in the time domain are used for verification of the final design because of the nonlinearities in the system. However, the liberty of accepting the long computation times can not be taken for concept designs. Constant changes that are made to the structural design demand quicker calculations. For that reason, frequency-domain analyses are implemented in the initial design phase.

1.2.2 Frequency-domain analysis

Instead of splitting up the time window into discrete time steps, one can analyze the problem in the frequency domain. Separate frequency components of the forcing are found. A time window of finite length T is assumed. Any real-valued forcing that is periodic in T can be split up into a summation of sinusoids:

$$\mathbf{f}(t) = \sum_{\mathrm{k}=0}^{\infty} \hat{\mathbf{a}}_{\mathrm{k}} cos(\mathrm{k}\Omega t) + \hat{\mathbf{b}}_{\mathrm{k}} sin(\mathrm{k}\Omega t) \tag{1.2}$$

where Ω is the fundamental frequency $\Omega = 2\pi/T$. This summation can also be written in the complex form:

$$\mathbf{f}(t) = \sum_{\mathrm{k}=0}^{\infty} Re\left(\hat{\mathbf{f}}_{\mathrm{k}} e^{\mathrm{k}i\Omega t}\right) \tag{1.3}$$

Note here the choice for a single-sided spectral representation. This way, the absolute value of $\hat{\mathbf{f}}_{\mathrm{k}}$ (complex-valued) corresponds to the amplitude of the associated sinusoid. $\hat{\mathbf{f}}_{\mathrm{k}}$ are called the *Fourier coefficients* of the excitation, as they can be found through performing a Fourier-transform.

A maximum is set on the amount of harmonics needed to receive accurate results from the calculations. This maximum is called H.

$$\mathbf{f}(t) = \sum_{\mathrm{k}=0}^{H} Re\left(\hat{\mathbf{f}}_{\mathrm{k}} e^{\mathrm{k}i\Omega t}\right) \tag{1.4}$$

A particular solution for the deflections in the system is filled in. We assume a solution where the transient part of the solution is neglected and a stationary response is found. A nonlinear system does not always reach a steady-state solution however. Nonetheless, we assume that for the load levels under investigation, the OWT does reach a steady-state solution. The suggested solution of $\mathbf{u}(t)$ is:

$$\mathbf{u}(t) = \sum_{\mathrm{k}=0}^{H} Re\left(\hat{\mathbf{u}}_{\mathrm{k}} e^{\mathrm{k}i\Omega t}\right) \tag{1.5}$$

In a classical frequency-domain analysis, nonlinearities can not be taken into account. This means one can look at each forcing frequency separately. A substitution of (1.4) and (1.5) into (1.1) and subsequent rearranging leads to:

$$\hat{\mathbf{u}}_{\mathrm{k}} = (-\mathrm{k}^2\Omega^2\mathbf{M} + \mathrm{k}i\Omega\mathbf{C} + \mathbf{K})^{-1} \cdot \hat{\mathbf{f}}_{\mathrm{k}} = \mathbf{H}(\mathrm{k}\Omega) \cdot \hat{\mathbf{f}}_{\mathrm{k}} \tag{1.6}$$

where $\mathbf{H}$ is called the *dynamic compliance matrix*. This means a set of $(H+1)$ Matrix-vector multiplications is needed to find $\hat{\mathbf{u}}$. Now that the Fourier coefficients of the response are found, an Inverse Fourier transform is required for the response in the time domain.

Figure 1.4 shows a simplified flowchart of a conventional frequency domain analysis. As the analyses performed for OWT design are done with discrete-time signals over a finite length of time (force input from load calculation software is defined the same), the Fourier transform changes into a Discrete Fourier Transform (DFT), and the inverse Fourier transform changes into an Inverse Discrete Fourier Transform (IDFT). In further sections analysis strategies change the conventional frequency domain procedure. We show differences from the conventional analysis strategy through these flow charts.

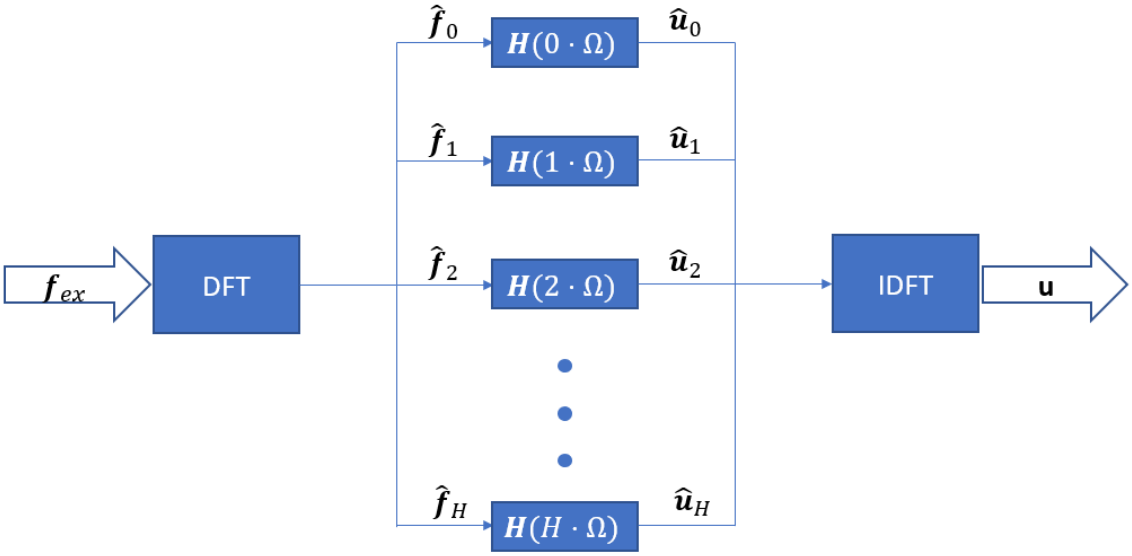

Figure 1.4: Flowchart of a conventional frequency domain analysis.

Every blue block is a separate calculation. This figure shows the disconnection between analysis of the different frequencies. Only limited calculations have to be performed. When compared to a time-domain analysis, where small time steps are required to ensure numerical stability of the solution, computational effort is significantly lower. The conventional frequency-domain analysis has a drawback, which is the inability to include nonlinearities into the model. In some engineering cases, linear modeling is not accurate. This is also the case for the analysis of OWTs on a monopile foundation.

1.3 Simplifying large dynamical systems with nonlinearity

Because of the large computational demand of a nonlinear dynamical analysis, a large part of research is devoted towards finding the right simplifications to speed up this process. One option to reduce the computational demand of a nonlinear dynamical analysis is to reduce the amount of elements in the finite element model that show nonlinearity. Specifically for the case of OWTs, the representation of the nonlinear foundation behavior of monopiles is captured with a single nonlinear macro-element [Krathe and Kaynia, 2016]. Especially for ULS conditions, such a model shows promise.

Whenever the nonlinearity in the system is limited, a linearization of the nonlinear effects can also be a viable solution strategy. [Corciulo et al., 2017a] shows that such a linearization can capture the behavior of such a large dynamical system. An important factor that plays a role however, as stated by [Corciulo et al., 2017a], is that the linearization applied fits the load level. Next to that, such a linearization strategy can not model permanent deformations. Therefore, such an analysis can not be performed when the structure is loaded under ULS conditions.

1.4 Foundation modeling

The focus area of this project is the modeling of an OWT on a monopile support structure. Figure 1.5 shows 3 popular methods of modeling the monopile foundation:

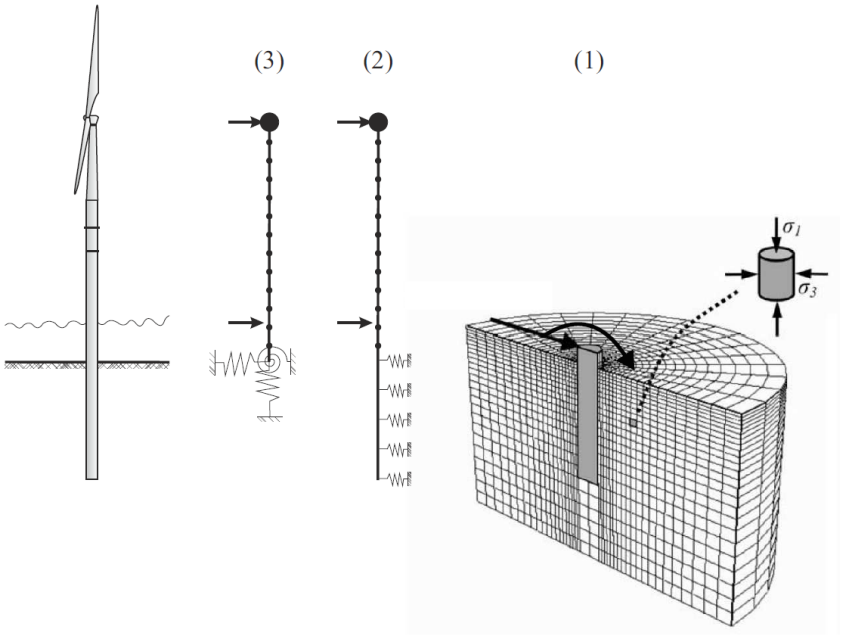

Figure 1.5: 3 strategies for OWT monopile foundations, [Abadie, 2015].

1. Modeling the soil reaction using a 3D soil medium
2. Modeling the soil reaction using a representative Winkler foundation
3. Modeling the soil reaction using representative coupled springs at mud-line level

The most elaborate model, the 3D soil medium, can be directly fitted to the local site response. In-situ soil investigation through for example a cone penetration test (CPT) is performed and soil samples are taken for further testing. By taking samples to a laboratory and performing cyclic (or dynamic) tests on the soil samples, soil parameters can be found to create a representative soil body. Stresses and strains in the soil can be calculated in the FE analyses, allowing for nonlinear soil behavior to be accounted for ([Corciulo et al., 2017b] and [Zhang et al., 2020]). The drawback however of this 3D soil medium is the large amount of degrees of freedom added to the FE model. Large amounts of degrees of freedom cause large computational problems. Further simplifications are often used to speed up the calculations.

The response of the soil body as a whole can also be represented by bedding spring elements along the foundation. An important step towards this new representation is the tuning of these bedding spring elements to the site response ([Versteijlen et al., 2016], [Versteijlen et al., 2017], [Versteijlen et al., 2018]).

Possible nonlinearity of the soil behavior can still be taken into account by adding nonlinearity to the bedding spring elements ([Byrne et al., 2017]). This Winkler-type foundation has significantly

less degrees of freedom when compared to a full 3D soil medium approach. At the same time however, deflections and rotations of the foundation can still be found. This information is useful for foundation design, especially for fatigue-driven checks.

Further simplifications can be made in representing the behavior of monopile foundation. A set of coupled (possibly nonlinear) springs can be substituted at mud-line ([Hoogstraten, 2019] and [Aasen et al., 2017]). That way, no extra degrees of freedom need to be added for either the foundation or the soil medium. We however lose information on deflections (and therefore stresses and moments) in the foundation.

1.4.1 Constitutive soil models

No matter what modeling strategy is picked, a constitutive model must be implemented to define the behavior of the soil. We will elaborate on 3 common types of constitutive models (as shown in Figure 1.6):

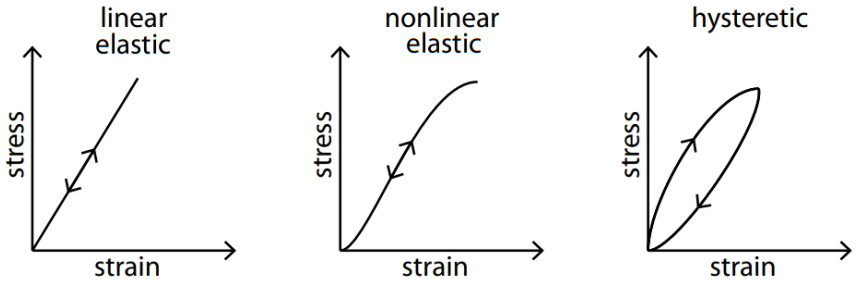

Figure 1.6: 3 common soil constitutive models, after [Stockhert, 2015].

1. A linear elastic model
2. A nonlinear elastic model
3. A nonlinear hysteretic model

Linear elastic models are most commonly used in small-strain dynamical analyses and in frequency-domain analyses. If local damping is added, linear viscous (in both frequency-domain and time-domain) or linear hysteretic damping (although only in frequency-domain methods) is applied as well.

Nonlinear elastic models allow for the stress-strain relation to change based on the amplitude of the strains in the soil. At reversal of strain direction however, the load path is exactly followed back. This means no damping is present in the nonlinear elastic constitutive model. Either local or global damping must be added to account for the damping in the soil.

Nonlinear hysteretic models also change stress-strain behavior dependent on the strain amplitude. As an extra condition however, the unloading path is different from the loading path. This means the model is dependent on its past loading history. Inherent hysteretic (rate-independent) damping is present in these hysteretic constitutive models. The damping in the soil around OWT when loaded with wind and wave loading is dominated by material damping [Malekjafarian et al., 2021], which is nonlinear hysteretic in nature. The combination of a nonlinear hysteretic soil model with a time-domain method is computationally demanding however. A highly nonlinear constitutive

model is needed to describe hysteretic behavior in the time domain. Therefore, small time steps needed to calculate the response of a nonlinear hysteretic soil model in the time domain.

More complex soil behavior like ratcheting [Abadie, 2015], pore pressure build-up, cyclic softening [Corciulo et al., 2017b] and scouring [Qi and Gao, 2014] could also be modeled. These effects require advanced constitutive models and generally affect the behavior of the soil at larger time spans than considered in dynamic analyses. These effects are not considered in this project.

1.4.2 The p-y method

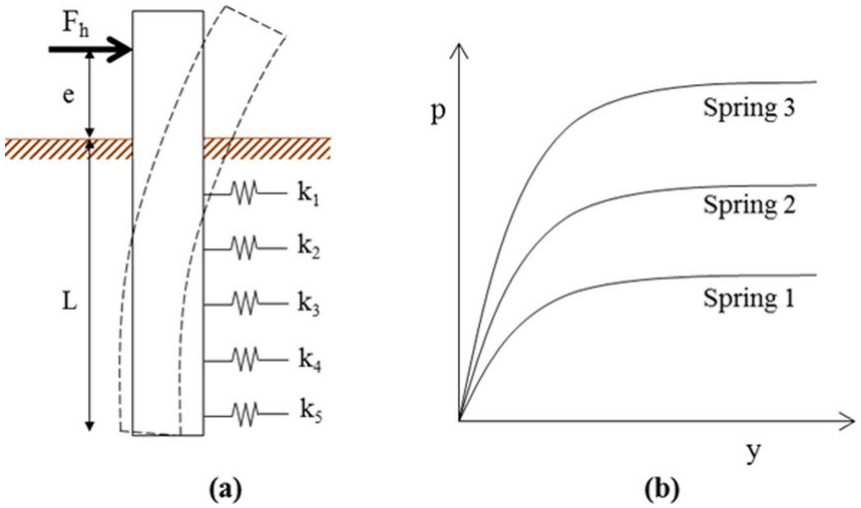

Figure 1.7: Representation of the p-y method, [Bayton and Black, 2016].

The industry standard for analysis of monopile foundations is the p-y method. This strategy combines a Winkler foundation with a nonlinear elastic constitutive soil model. The soil reaction is defined as depth-dependent distributed elements. The element behavior is a function of the deflections in the foundation. Originally derived for use in piles with small diameters, these p-y curves were fitted to piles with larger diameters using 3D FE simulations and full-scale tests [Byrne et al., 2017] or lab tests through centrifuge models [Bayton and Black, 2016]. The p-y curves were designed for monotonic loading. To ensure safe design, these p-y curves are reduced by a factor when applied in cyclic load cases [DNV, 2019]. Usage of the p-y method in cyclic and dynamic loading is challenged [Abadie, 2015], as cyclic and dynamic soil properties are currently not integrated into the method. Next to that, local soil damping is generally not taken into account (and is instead added through modal or Rayleigh damping).

Usage of the p-y method in the design of monopile foundations allows for consideration of reduced soil stiffnesses at larger foundation deflections. However, because of the nonlinear elastic constitutive model used, the method can not be integrated into conventional frequency-domain calculations. Initial designs are currently evaluated in the frequency domain with linear elastic constitutive soil models.

1.5 Fatigue damage calculation

As the area of focus is simulations in the Fatigue Limit State, the next step to take is to calculate the fatigue damage. Just as with the simulations, methods for calculation of fatigue damage exist in both the time domain and the frequency domain. Both methods revolve around calculation of the stresses in the structure, while taking into account the number of load cycles.

1.5.1 Time domain: Rainflow-counting method

Because of the multiharmonic nature of the loading for OWTs, one can not define a single stress amplitude for fatigue calculation. Different cycles of different stress amplitudes occur, while these cycles also overlap. The rainflow-counting method [Matsuishi and Endo, 1968] provides a solution to that problem, taking inspiration from rain flowing over Japanese pagoda roofs. Figure 1.8 shows how such a rainflow-counting method works. Firstly, the stress reversal points are isolated from the time-history of the stresses in the structure. Secondly, half-cycles are derived from the reversal points. From these half-cycles, a probability density function of the stress cycle amplitudes can be created.

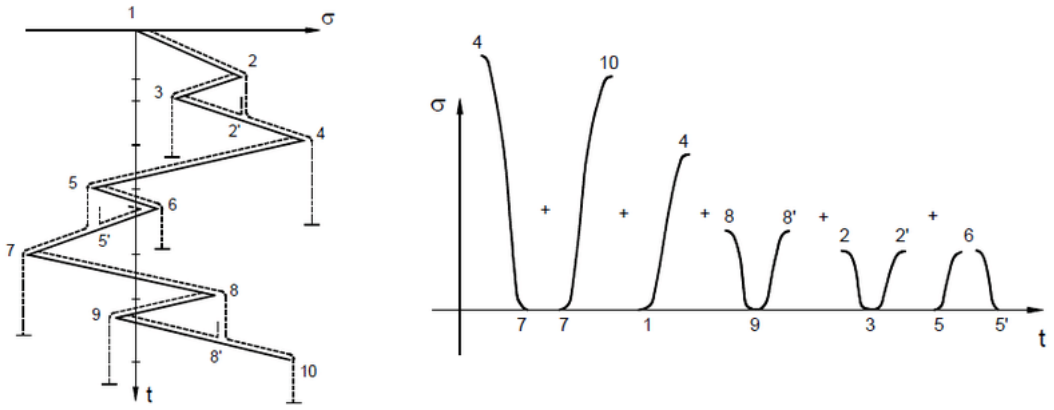

Figure 1.8: The rainflow-counting method, [Guilherme and Correia, 2016]

This procedure does not have any requirements on the system that is analyzed. Nonlinearities both the structure and the forcing can be taken into account. However, the method requires time-history results of the stresses in the structure. This means that probabilistic methods can not be directly used. A large amount of simulations are needed to find the appropriate probability density function of the stress cycles.

1.5.2 Frequency domain: Dirlik method

Just as with the simulations itself, simplified methods exist to approximate probability density functions of the stress amplitudes in the structure. A probabilistic approach exists in the frequency domain. Load spectra $\mathbf{S}_{FF}(\omega)$ are used as an input instead of time-histories of the load. Through the use of transfer functions (derived through the same method as the dynamic compliance matrix $\mathbf{H}(k\Omega)$) we transform the load spectra into stress spectra $\mathbf{S}_{\sigma\sigma}(\omega)$:

$$\mathbf{S}_{\sigma\sigma}(\omega) = \left(\mathbf{H}_{\sigma F}(\omega)\right)^2 \cdot \mathbf{S}_{FF}(\omega) \tag{1.7}$$

The Dirlik method then changes these stress spectra of the structure into probability density functions that can be used in fatigue damage calculation.

$$p(S) = \frac{\frac{D_1}{Q}\, e^{\left(-\frac{Z}{Q}\right)} + \frac{D_2 Z}{R^2}\, e^{\left(\frac{-Z^2}{2R^2}\right)} + D_3 Z\, e^{\left(\frac{-Z^2}{2}\right)}}{2\sqrt{m_0}}$$

Figure 1.9: The Dirlik formula.

$$D_1 = \frac{2*(x_m-\gamma^2)}{1+\gamma^2}, \quad D_2 = \frac{1-\gamma-D_1+D_1^2}{1-R}, \quad D_3 = 1 - D_1 - D_2, \quad Q = \frac{1{,}25*(\gamma-D_3-D_2*R)}{D_1}$$

$$R = \frac{\gamma-x_m-D_1^2}{1-\gamma-D_1+D_1^2}, \quad Z = \frac{S}{2*\sqrt{m_0}}, \quad x_m = \frac{m_1}{m_0} * \sqrt{\frac{m_2}{m_4}}, \quad \nu_p = \sqrt{\frac{m_4}{m_2}}, \quad \gamma = \frac{m_2}{\sqrt{m_0*m_4}}$$

Figure 1.10: The Dirlik formula parameters.

with spectral moments m_n defined as:

$$m_n = \int \mathbf{S}(\omega) \cdot \omega^n d\omega \tag{1.8}$$

As the Dirlik method directly uses spectra of the load, no information about the time-history of the load is needed for the calculations. The method of using a transfer function to find stress spectra however assumes steady-state behavior (no time-history dependent effects can be taken into account) and also assumes linearity of the structural response.

1.5.3 Palmgren-Miner rule

The probability density functions of the stress amplitudes in the structure are found (either through rainflow-counting method or Dirlik method). Such a probability density function looks like Figure 1.11:

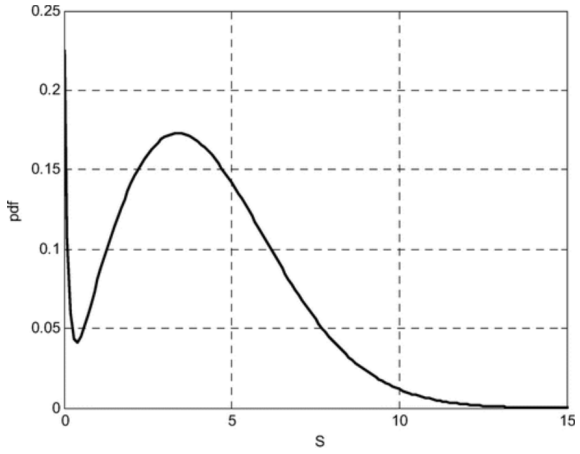

Figure 1.11: A probability density function of stress amplitudes, [Madhukar et al., 2018].

Accumulated fatigue damage can afterwards be calculated through the Palmgren-Miner rule:

$$\sum_{i=1}^{s} \frac{n_i(S_i)}{N_i(S_i)} \leq 1 \tag{1.9}$$

where s different cycles at stress level S_i are analyzed, n_i expresses the amount of cycles at stress level S_i and N_i expresses the maximum amount of cycles at that stress level. This method assumes the maximum amount of stress cycles is deterministic however. To ensure safety, design curves are used to set a safe limit for $N_i(S_i)$. These curves are called S-N curves, of which an example is given in Figure 1.12. In the case of OWT design, the S-N curves are often set up at cross-sectional level, which means that instead of stresses, shear forces and moments are used as input for S.

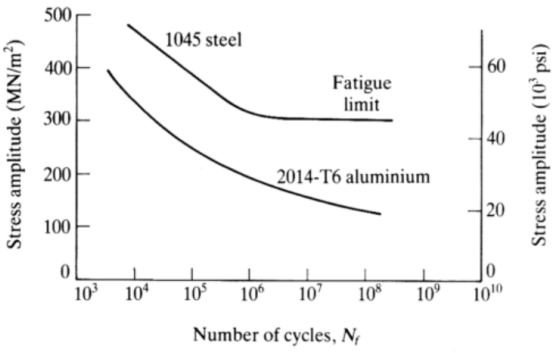

Figure 1.12: Example of S-N curves, [Sobczyk et al., 2010].

By increasing the analyzed time until the cumulative fatigue damage ratio reaches 1, the fatigue life time of the structure can be calculated.

1.6 Research question and goals

The main goal of the thesis is to improve the modeling of OWTs on a monopile support structure under FLS conditions, with a focus to the modeling of the foundation. The nonlinear hysteretic nature of the soil reaction can not be combined with conventional frequency-domain analyses. The main research question is therefore:

How to combine a nonlinear hysteretic constitutive soil model with a frequency-domain analysis to improve simulations of Offshore Wind Turbines on a monopile foundation under Fatigue Limit State conditions?

In order to answer this main research question, we define goals that are tackled separately:

- To **compare** different solution strategies in the frequency domain based on their ability to represent hysteretic behavior.
- To **evaluate** the solution strategies on their ability to be used in a full FE model under multiharmonic excitation.
- To **fit** hysteretic constitutive models to available soil reaction data.
- To **set up** an FE formulation that includes the suggested solution strategy and constitutive model.
- To **verify** the FE formulation with an available structural model of an OWT on a monopile foundation.
- To **quantify** the change in foundation response (in stiffness, damping and deflection shape) between a conventional frequency-domain analysis and the suggested solution strategy.
- To **compare** the suggested frequency-domain solution strategy to a time-domain strategy which uses a p-y formulation for the monopile foundation. The focus lies on the behavior of the monopile foundation.

1.7 Research outline

In Chapter 2 an investigation into a mathematical framework for the combination of nonlinearity with a frequency-domain calculation is laid out: The Harmonic Balance Method (HBM). For the case of a hysteretic constitutive model (specifically the Bouc-Wen model of hysteresis), a strategy called the Alternating Frequency-Time Harmonic Balance Method (AFTHBM) is needed. The performance of this method in 1DOF to a harmonic load is tested by comparing the results to a nonlinear time integration strategy. The feasibility of an AFTHBM strategy in NDOF subjected to multiharmonic loading is also assessed by identifying the complexity of the algorithm.

Chapter 3 presents a simplification of AFTHBM. The dependency of the Bouc-Wen element on its response amplitude is highlighted. Based on that dependency, a response-amplitude dependent linearization is defined. The set of linearizations is defined as an equivalent linear (EQL) element. Through this EQL method the Bouc-Wen element is analyzed in 1DOF to both harmonic and spectral loading. The results are compared to AFTHBM and to a nonlinear time integration strategy. The feasibility of the EQL strategy in NDOF subjected to multiharmonic loading is checked through identification of the complexity of the algorithm. and we decide to move forward with the EQL method.

In Chapter 4, a fitting procedure of 2 hysteretic constitutive soil models to available soil reaction curves is shown. The 2 models in question are the Bouc-Wen model of hysteresis and the Masing model. We assess the stiffness reduction and hysteretic damping curves and make a comparison between observed stiffness and damping and results from literature. Based on this assessment, the choice is made to move forward with the Masing model, but to apply a cap to the hysteretic damping to avoid overdamping at large response amplitudes.

A structural finite element model is set up in Chapter 5, where the different parts of the finite element definition are shown. We also show how the EQL method fits into this model, and how to add forcing and other sources of damping next to the soil damping.

In Chapter 6, this structural model is verified through a case study. A structural model used in Siemens Gamesa Renewable Energy (SGRE) is taken as reference. Mode shapes and resonance frequencies are compared, and differences in modeling strategy are elaborated on.

Chapter 7 presents a comparison between a conventional (linear) frequency-domain method, 2 versions of the EQL analysis and a nonlinear time-integration method. The subject of comparison is the structural model from Chapter 6 subjected to (high) FLS wave loading. Stiffness and damping properties of the foundation are compared and deflection spectra in the foundation are analyzed. The potential of an EQL analysis is assessed by stating its strengths and limitations. The usability of an EQL analysis for fatigue damage calculation is also evaluated.

The last chapter, Chapter 8, summarizes the drawn conclusions in the project and answers the main research question. Recommendations for future research are also stated.

Section 2

Nonlinear modeling in the frequency domain

2.1 Nonlinearity vs. modeling in the frequency domain

Nonlinearity and frequency domain methods are not trivial topics to combine. A conventional frequency domain analysis hinges on one core principle:

The superposition principle:
$F(X_1) + F(X_2) = F(X_1 + X_2)$ $(Additivity)$
$F(aX) = aF(X)$ $(Homogeneity)$

where X is an external force applied to the system, and $F(X)$ is the response of the system. This superposition principle is the base requirement of conventional frequency domain methods, because it allows an arbitrary load to be split up into components which are separately solvable. The components we take are the different harmonics in the external force, as the response of the system to a harmonic force is easier to calculate.

In the case of steady state solutions, this means each separate harmonic component of the force generates a harmonic response of the same frequency.

However, nonlinear hysteretic models do not follow the superposition principle. An input of a sinusoidal force will no longer produce an output of a sinusoid.

Because the goal is to do want to combine nonlinearity and a frequency domain analysis, either the nonlinear hysteretic model or the frequency-domain strategy has to change.

2.2 The Harmonic Balance Method

A technique for combining frequency domain analysis and nonlinearity exists. This technique is called the Harmonic Balance Method (HBM) and focusses on a change of the frequency-domain strategy. The combination between dynamics of soil continua and the Harmonic Balance Method is made in other research [Zhang et al., 2020]. Throughout this chapter, we follow definitions from [Krack and Gross, 2019]. For HBM to work, the superposition principle can not be used. HBM instead starts from a different, weaker assumption:

The response to a periodic load is also periodic with fundamental period T

This assumption feels natural: When a load is periodic, we expect the response to also be periodic. Right from the start however, a limitation that this assumption brings can be seen. In the case of high loads, permanent deformations could occur in a nonlinear system like the foundation of a monopile. Therefore, this approach is limited to small and medium strains levels at which the permanent deformations are limited.

We note here that the fundamental period of the response does not have to be the fundamental period of the force. This specific note is made to not exclude sub-harmonic responses (the effect that a force with fundamental period T results in a response with fundamental period which is a multiple T).

The goal is now to formulate a system of equations that can contain a nonlinear element in the frequency domain. For now, the investigation is restricted to one nonlinear element in isolation. As this element has 1 Degree of Freedom (1DOF), Equation 1.1 collapses to:

$$m\ddot{u}(t) + c\dot{u}(t) + ku(t) + \mathbf{f}_{nl}(t, \ddot{\mathbf{u}}, \dot{\mathbf{u}}, \mathbf{u}) = f_{ex}(t) \tag{2.1}$$

As said before, it is assumed that $u(t)$ is periodic with fundamental period T and can be described with H harmonics. We then define $f_{ex}(t)$ with the same fundamental period T. A Fourier series representation of both the external force and the deflection is defined. Because later algorithms rely on real-valued coefficients, a sine-cosine representation is used:

$$f_{ex}(t) = \sum_{\mathrm{k}=0}^{H} \hat{a}_{\mathrm{k}} cos(\mathrm{k}\Omega t) + \hat{b}_{\mathrm{k}} sin(\mathrm{k}\Omega t) \tag{2.2}$$

$$u(t) = \sum_{\mathrm{k}=0}^{H} \hat{c}_{\mathrm{k}} cos(\mathrm{k}\Omega t) + \hat{d}_{\mathrm{k}} sin(\mathrm{k}\Omega t) \tag{2.3}$$

The Fourier amplitudes of both forcing and response are stored in the following manner:

$$\hat{\mathbf{f}}_{\mathbf{ex}} = \begin{bmatrix} \hat{a}_0 & \hat{a}_1 & \hat{b}_1 & \hat{a}_2 & \hat{b}_2 & \cdots & \hat{a}_H & \hat{b}_H \end{bmatrix}^T \tag{2.4}$$

$$\hat{\mathbf{u}} = \begin{bmatrix} \hat{c}_0 & \hat{c}_1 & \hat{d}_1 & \hat{c}_2 & \hat{d}_2 & \cdots & \hat{c}_H & \hat{d}_H \end{bmatrix}^T \tag{2.5}$$

For Equation (2.1) to hold in combination with the assumptions made, $f_{nl}(t)$ **must** also be periodic with fundamental period T and able to be described with H harmonics. Its coefficients can be stored in the same way as $\hat{\mathbf{f}}_{\mathbf{ex}}$ and $\hat{\mathbf{u}}$, summarized as $\hat{\mathbf{f}}_{\mathbf{nl}}$.

The goal is to transform Equation (2.1) into the frequency domain. This means the time-derivatives $\ddot{u}(t)$ and $\dot{u}(t)$ also have to be transformed. Taking a derivative with respect to time in the frequency domain is relatively straightforward. This goal can be achieved by multiplying $\hat{\mathbf{u}}$ with Ω^n and a derivative matrix $\check{\nabla}^{\mathbf{n}}$, where n stands for taking the n-th derivative with respect to time:

$$\frac{d^n \hat{\mathbf{u}}}{dt^n} = \check{\nabla}^{\mathbf{n}} \cdot \hat{\mathbf{u}} \tag{2.6}$$

The content of this matrix can be derived by taking the derivative of Equation (2.3) and collecting the resulting coefficients:

$$\check{\nabla}^{\mathbf{0}} = \begin{bmatrix} 1 & 0 & 0 & 0 & 0 & & 0 & 0 \\ 0 & 1 & 0 & 0 & 0 & & 0 & 0 \\ 0 & 0 & 1 & 0 & 0 & \cdots & 0 & 0 \\ 0 & 0 & 0 & 1 & 0 & & 0 & 0 \\ 0 & 0 & 0 & 0 & 1 & & 0 & 0 \\ & & \vdots & & & \ddots & & \vdots \\ 0 & 0 & 0 & 0 & 0 & & 1 & 0 \\ 0 & 0 & 0 & 0 & 0 & \cdots & 0 & 1 \end{bmatrix} \tag{2.7}$$

$$\check{\nabla}^{\mathbf{1}} = \begin{bmatrix} 0 & 0 & 0 & 0 & 0 & & 0 & 0 \\ 0 & 0 & 1 & 0 & 0 & & 0 & 0 \\ 0 & -1 & 0 & 0 & 0 & \dots & 0 & 0 \\ 0 & 0 & 0 & 0 & 2 & & 0 & 0 \\ 0 & 0 & 0 & -2 & 0 & & 0 & 0 \\ & & \vdots & & & \ddots & & \vdots \\ 0 & 0 & 0 & 0 & 0 & & 0 & H \\ 0 & 0 & 0 & 0 & 0 & \dots & -H & 0 \end{bmatrix} \tag{2.8}$$

$$\check{\nabla}^{\mathbf{2}} = \begin{bmatrix} 0 & 0 & 0 & 0 & 0 & & 0 & 0 \\ 0 & -1 & 0 & 0 & 0 & & 0 & 0 \\ 0 & 0 & -1 & 0 & 0 & \dots & 0 & 0 \\ 0 & 0 & 0 & -4 & 0 & & 0 & 0 \\ 0 & 0 & 0 & 0 & -4 & & 0 & 0 \\ & & \vdots & & & \ddots & & \vdots \\ 0 & 0 & 0 & 0 & 0 & & -H^2 & 0 \\ 0 & 0 & 0 & 0 & 0 & \dots & 0 & -H^2 \end{bmatrix} \tag{2.9}$$

Note here that $\check{\nabla}^{\mathbf{0}}$ stands for taking the '0-th' derivative (not taking a derivative with respect to time). This operator (Basically $\mathbf{I}$) is useful in generalization of HBM to multiple degrees of freedom and in simplification of operation matrices.
Combining Equations (2.1 - 2.9) and reordering the terms creates the following set of equations:

$$\left(m\Omega^2\check{\nabla}^{\mathbf{2}} + c\Omega\check{\nabla}^{\mathbf{1}} + k\check{\nabla}^{\mathbf{0}}\right) \cdot \hat{\mathbf{u}} - \hat{\mathbf{f}}_{\mathbf{ex}} + \hat{\mathbf{f}}_{\mathbf{nl}} = \mathbf{0} \tag{2.10}$$

Equation (2.10) shows where nonlinearity is added in the system of equations. The most important part however is to describe the nonlinearity in $\hat{\mathbf{f}}_{\mathbf{nl}}$. Through this component, different harmonics in the response will be linked to each other. Our system can no longer be separated into $H+1$ separate calculations, which means we have to solve for all harmonics **at the same time**.

This change in strategy changes the solution flow chart from Figure (1.4). Figure (2.1) shows the interconnected nature of the calculation. We have to find a model that can represent the nonlinear soil reaction around monopile foundations **and** can be combined with the Harmonic Balance method to form $\hat{\mathbf{f}}_{\mathbf{nl}}$.

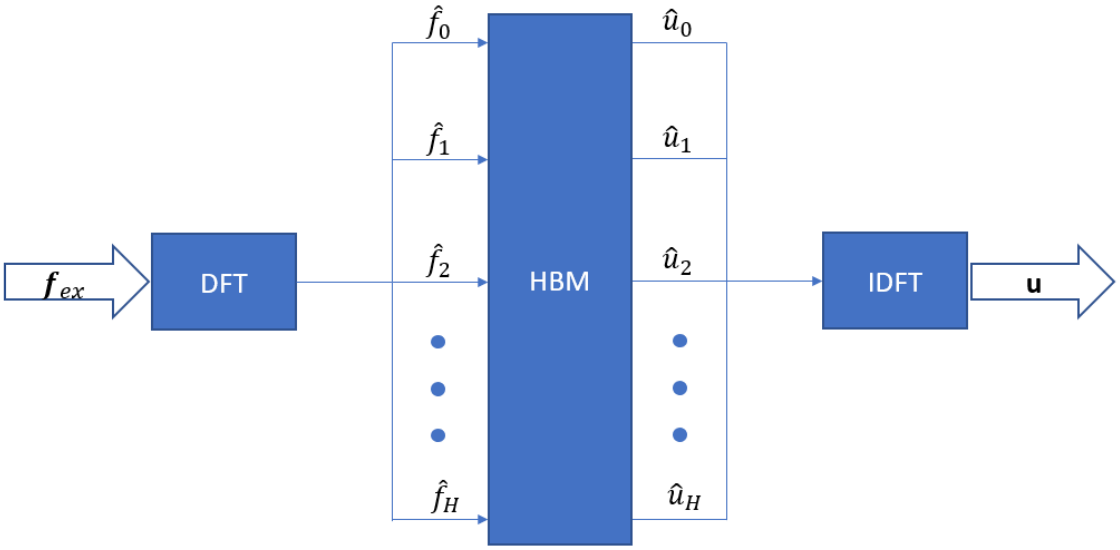

Figure 2.1: Flowchart of the Harmonic Balance Method.

2.3 Requirements for the nonlinear hysteretic element

A nonlinear hysteretic element must be chosen to represent the soil response in the foundation. The requirements for this element are:

- The element must show strain-dependent behavior.
- The element must generate hysteresis loops in cyclic/dynamic loading.
- The element must be versatile in fitting.
- The element must have a representation in the time domain.
- The element must be compatible with the Harmonic Balance Method.

The first 2 requirements reflect the type of element we are looking for. The description of nonlinearity should focus on strain-dependency and should show hysteretic behavior in cyclic or dynamic loading conditions. Nonlinear elastic models (like the p-y formulation) for example do not fulfill the second requirement.

The 3rd requirement is based on the varying behavior of the soil reaction we are emulating. Differing soil composition, depth and other factors influence the reaction of the soil element. The simplest models might not be able to capture small differences in behavior.

The last 2 requirements focus on the ability to validate the behavior of the element. When a model has a proven solution strategy in both the time domain and the Harmonic Balance Method, we can draw conclusions from the found results more easily.

2.4 The Masing model

A common choice for modeling the cyclic response of a foundation is the following: a Masing model. An example in modeling cyclic plasticity through a Masing model is shown by [Chiang, 1999]. 3 rules are linked to Masing models, commonly called the original and extended Masing rules. Firstly, a backbone curve (force-deformation relationship) $f_{bb}(u)$ is defined.
In the case of modeling a foundtion, this relationship is defined by p-y curves introduced in Section 1.4.2. The original Masing rule states that, in steady state cyclic behavior, the loading and unloading branches are defined as:

$$p(u) = \begin{cases} 2\mathrm{f}_{bb}(\frac{u+u_0}{2})) - p_0 & \text{if} \quad \dot{u} > 0 \\ 2\mathrm{f}_{bb}(\frac{u-u_0}{2})) + p_0 & \text{if} \quad \dot{u} < 0 \end{cases} \tag{2.11}$$

where (u_0, p_0) denotes the load reversal point. An example of a hysteresis loop generated by this model is given in Figure (2.2).

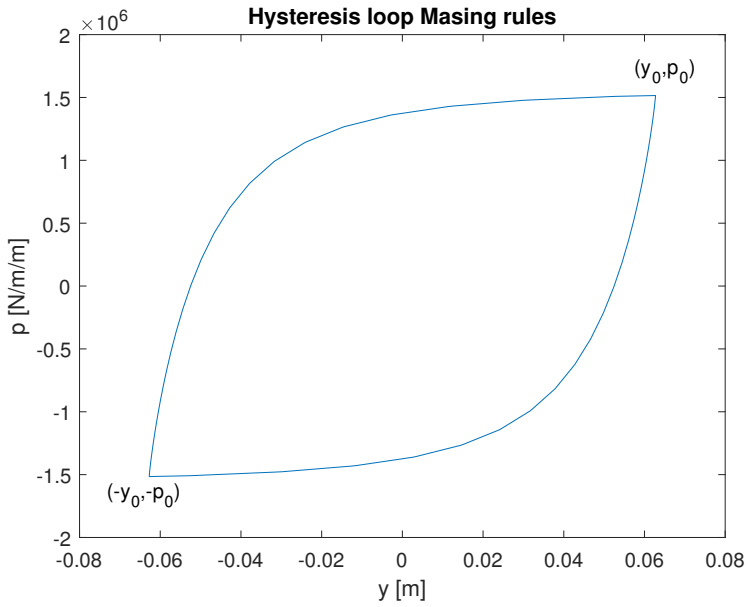

Figure 2.2: A hysteresis loop generated through Masing rules.

The original Masing rule only defines response in steady-state behavior under harmonic loading. As a multiharmonic loading is added to the system, the definition of the Masing rules needs an extension. Therefore, two extra rules are added (cited from [Chiang, 1999]):

Rule 1. The equation of any hysteretic response curve can be obtained by applying the original Masing rule to the virgin loading curve using the *latest* point of load reversal.

Rule 2. If an interior curve under continued loading or unloading crosses a curve described in a previous load cycle, the force-deformation curve follows that of the previous cycle.

Addition of these rules means the element is capable of handling arbitrary loading. The extended Masing model is now assessed based on the requirements set in Section (2.3). Strain-dependent behavior is indeed modeled, and hysteresis loops are generated. Through custom input of the backbone curve, one can control the element behavior. A time-domain solution strategy (following the original and extended Masing rules) exists as well (for example [Lacarbonara and Vestroni, 2003]).

In the implementation of extended Masing rules, a history of load reversal points has to be stored and used in the model. This history of load reversal points, a set of state variables of which nothing is known a priori, can not be treated in the frequency domain. This rules out a solution strategy of the extended Masing rules through HBM. The original Masing rules are compatible with the Harmonic Balance Method [van der Esch, 2020]. Ease of implementation of the method does depend on the definition of the backbone curve however.

2.5 The Bouc-Wen element

Another suitable candidate for our nonlinear element is the Bouc-Wen model of hysteresis. This model is broadly used in various academic fields (including civil engineering) and has a relatively simple setup. An abundance of modifications is available should the need arise for added complexity.

We begin with stating the basic equations related to the Bouc-Wen model. We start from Equation (2.1) and add our Bouc-Wen element $R(t)$ in the place of $\mathrm{f}_{nl}(t)$:

$$m\ddot{u}(t) + c\dot{u}(t) + ku(t) + R(t) = \mathrm{f}_{ex}(t) \tag{2.12}$$

with the element specification:

$$R(t) = \alpha k_i u(t) + (1-\alpha) k_i z(t) \tag{2.13}$$

Here, k_i represents the initial stiffness of the element and α represents the (constant) ratio between the post-yielding stiffness and the initial stiffness. As soil does not have any post-yielding stiffness (soil fails when the yield strength is reached), α is theoretically 0. However, due to numerical reasons related to the HBM solution strategy, α can not be 0. Therefore, this post-yielding stiffness part is included in the formulation of the element. k is added to the system of equations as in the case of multiple degrees of freedom linear elements can also be present in the system. Addition of this extra linear stiffness term allows for easier generalization to more degrees of freedom.

$z(t)$ is a newly introduced state variable. This variable is called the hysteretic displacement and controls the degree of yielding. Just as the other time-dependent variables the relation of $z(t)$ and $\hat{\mathbf{z}}$ is defined:

$$z(t) = \sum_{\mathrm{k}=0}^{H} \hat{p}_{\mathrm{k}} cos(\mathrm{k}\Omega t) + \hat{q}_{\mathrm{k}} sin(\mathrm{k}\Omega t) \tag{2.14}$$

$$\hat{\mathbf{z}} = \begin{bmatrix} \hat{p}_0 & \hat{p}_1 & \hat{q}_1 & \hat{p}_2 & \hat{q}_2 & \cdots & \hat{p}_H & \hat{q}_H \end{bmatrix}^T \tag{2.15}$$

The behavior of $z(t)$ is controlled through a separate nonlinear ordinary differential equation:

$$\dot{z}(t) = \dot{u}(t) \left(\kappa - [\gamma + \beta \cdot sgn(\dot{u}(t)) \cdot sgn(z(t))] \cdot |z(t)|^n \right) \tag{2.16}$$

Four parameters control the final shape of the hysteresis: κ, γ, β and n. Take note here that γ and β are sometimes interchanged in literature. The effect of the different parameters on the final hysteresis loop was investigated ([Wong et al., 1994a] and [Wong et al., 1994b]). Next to that, constraints on said parameters when applied to physical springs were summarized [Charalampakis, 2010].

An overview of the Bouc-Wen element in monotonic loading is given in Figure 2.3.

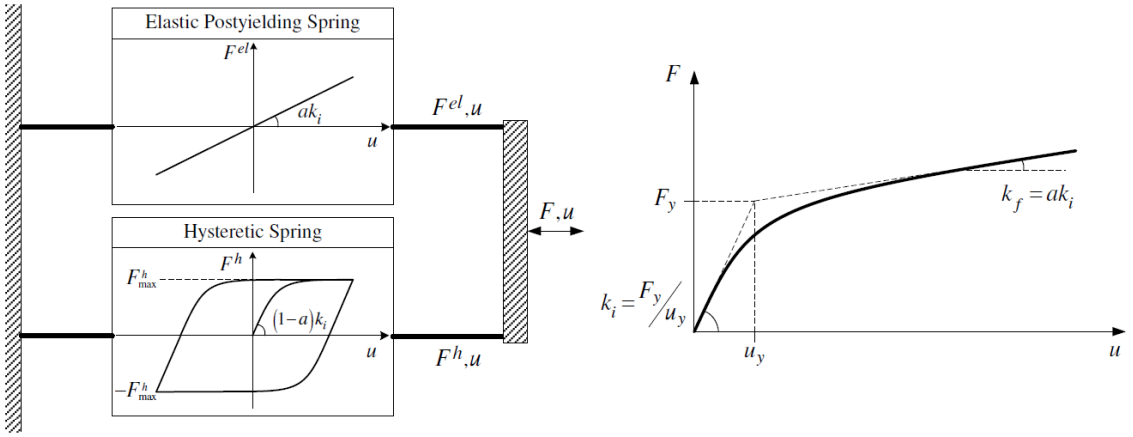

Figure 2.3: The Bouc-Wen model in monotonic loading, [Charalampakis, 2010].

Figure 2.4 shows the hysteresis loop generated by the Bouc-Wen element in cyclic loading.

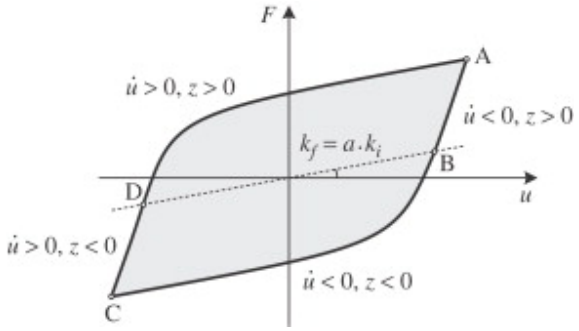

Figure 2.4: The Bouc-Wen model in cyclic loading, [Charalampakis, 2010].

The Bouc-Wen element is now assessed with respect to the requirements set in Section 2.3. The Bouc-Wen element is indeed strain-dependent. The degree of nonlinearity varies with the amplitude of $z(t)$, as can be seen from Equation 2.16. The element does indeed create hysteresis loops in dynamic loading and can create a wide variety of hysteretic behavior. A solution strategy in the time domain is relatively straightforward (a set of ODE's, of which one is non-linear).

The main advantage of the Bouc-Wen element with respect to the extended Masing element, is the addition of only one state variable $z(t)$. Also, this state variable is defined by a nonlinear ODE. This means the Bouc-wen element can be more easily combined with HBM than the extended Masing element. The Bouc-Wen element also theoretically allows for the application of arbitrary loading (contrary to the original Masing element). Therefore, the decision is made to move forward with the Bouc-Wen model.

Nevertheless, there is no closed form definition for $\hat{\mathbf{f}}_{\mathbf{nl}}$ when the Bouc-Wen model is implemented through classical HBM. A numerical approximation $\hat{\mathbf{f}}_{\mathbf{nl}}$ is necessary. The Alternating Frequency-Time Harmonic Balance Method (AFTHBM) is a solution strategy that does exactly that.

2.6 Alternating Frequency-Time Harmonic Balance Method

2.6.1 Initial linear calculation

AFTHBM tries to solve the problem of finding $\hat{\mathbf{f}}_{\mathbf{nl}}$. The calculation will switch to the time domain whenever an operation can not be performed in the frequency domain. Once the result of this operation is found, the calculation is continued in the frequency domain again. This process is iterative, which means wthe AFTHBM is constantly alternating between the time domain and the frequency domain until a satisfactory result is found. An explanation of AFTHBM can be found in [Krack and Gross, 2019]. Next to that, Wong describes in [Wong et al., 1994a] an AFTHBM strategy directly applied to the Bouc-Wen element. We will follow and carry out the strategy of Wong in order to see whether the strategy is useful within the scope of the thesis.

The first task is to make a first calculation. In every iterative procedure, a good first guess is vital for convergence tof the algorithm. The derivation of AFTHBM in combination with a Bouc-Wen element start with Equations 2.12 - 2.13 and rewriting them into HBM form:

$$\left(m\Omega^2\breve{\nabla}^{\mathbf{2}} + c\Omega\breve{\nabla}^{\mathbf{1}} + k\breve{\nabla}^{\mathbf{0}}\right)\cdot\hat{\mathbf{u}} + \alpha k_i\breve{\nabla}^{\mathbf{0}}\cdot\hat{\mathbf{u}} + (1-\alpha)k_i\breve{\nabla}^{\mathbf{0}}\cdot\hat{\mathbf{z}} = \hat{\mathbf{f}}_{\mathbf{ex}} \tag{2.17}$$

For the first calculation, the Bouc-Wen element is assumed to act linearly k_i. T This changes the equation to:

$$\left(m\Omega^2\breve{\nabla}^{\mathbf{2}} + c\Omega\breve{\nabla}^{\mathbf{1}} + k\breve{\nabla}^{\mathbf{0}}\right)\cdot\hat{\mathbf{u}} + k_i\breve{\nabla}^{\mathbf{0}}\cdot\hat{\mathbf{u}} = \hat{\mathbf{f}}_{\mathbf{ex}} \tag{2.18}$$

The solution to this problem is:

$$\hat{\mathbf{u}} = \left(m\Omega^2\breve{\nabla}^{\mathbf{2}} + c\Omega\breve{\nabla}^{\mathbf{1}} + k\breve{\nabla}^{\mathbf{0}} + k_i\breve{\nabla}^{\mathbf{0}}\right)^{-1}\cdot\hat{\mathbf{f}}_{\mathbf{ex}} \tag{2.19}$$

Equation 2.19 is equivalent to a conventional frequency-domain analysis with slightly different formulation of the Fourier coefficients. The stiffness of the Bouc-Wen element is not completely linear however, it is split in a linear and a hysteretic component. To find a good first guess for $\hat{\mathbf{z}}$, Equation 2.17 is used. Equation 2.17 on its own is linear and can be solved for $\hat{\mathbf{z}}$ when $\hat{\mathbf{u}}$ is known. After a reordering of the terms Equation 2.17 changes to:

$$\hat{\mathbf{z}} = \left((1-\alpha)k_i\breve{\nabla}^{\mathbf{0}}\right)^{-1}\cdot\left(\hat{\mathbf{f}}_{\mathbf{ex}} - \left(m\Omega^2\breve{\nabla}^{\mathbf{2}} + c\Omega\breve{\nabla}^{\mathbf{1}} + k\breve{\nabla}^{\mathbf{0}} + \alpha k_i\breve{\nabla}^{\mathbf{0}}\right)\cdot\hat{\mathbf{u}}\right) \tag{2.20}$$

The first guesses for $\hat{\mathbf{u}}$ and $\hat{\mathbf{z}}$ are now calculated. These guesses satisfy Equation 2.17 but will almost certainly not satisfy Equation 2.16. This is where AFTHBM will come into play.

2.6.2 Inverse Fourier transform and calculation of the residual

Equation 2.16) can not be directly solved in the frequency domain, as was concluded before. $\hat{\mathbf{f}}_{\mathbf{nl}}$ is numerically approximated, by calculating $\hat{f}_{nl}$ in the time domain first. Important here is the discretization of time. Enough samples are needed for a good estimation (to prevent aliasing). The time vector is defined as:

$$\mathbf{t} = \begin{bmatrix} 0 & T/M & 2T/M & \dots & (M-1)T/M \end{bmatrix}^T \tag{2.21}$$

Where T is still the fundamental period and M denotes the amount of samples taken in the time domain. $\hat{\mathbf{u}}$ is transformed back into $\mathbf{u}$ (and $\dot{\mathbf{u}}$) and $\hat{\mathbf{z}}$ is transformed back into $\mathbf{z}$ (and $\dot{\mathbf{z}}$):

$$\mathbf{u} = \sum_{\mathrm{k}=0}^{H} \hat{c}_{\mathrm{k}} cos(\mathrm{k}\Omega\mathbf{t}) + \hat{d}_{\mathrm{k}} sin(\mathrm{k}\Omega\mathbf{t}) \tag{2.22}$$

$$\dot{\mathbf{u}} = \sum_{\mathrm{k}=0}^{H} -\mathrm{k}\Omega \cdot \hat{c}_{\mathrm{k}} sin(\mathrm{k}\Omega\mathbf{t}) + \mathrm{k}\Omega \cdot \hat{d}_{\mathrm{k}} cos(\mathrm{k}\Omega\mathbf{t}) \tag{2.23}$$

$$\mathbf{z} = \sum_{\mathrm{k}=0}^{H} \hat{p}_{\mathrm{k}} cos(\mathrm{k}\Omega\mathbf{t}) + \hat{q}_{\mathrm{k}} sin(\mathrm{k}\Omega\mathbf{t}) \tag{2.24}$$

$$\dot{\mathbf{z}} = \sum_{\mathrm{k}=0}^{H} -k\Omega \cdot \hat{p}_{\mathrm{k}} sin(\mathrm{k}\Omega\mathbf{t}) + \mathrm{k}\Omega \cdot \hat{q}_{\mathrm{k}} cos(\mathrm{k}\Omega\mathbf{t}) \tag{2.25}$$

The state vectors are now defined in the time domain and Equation 2.16 can be used. This Equation is turned into an optimization problem:

$$r(t) = \dot{z}(t) - \dot{u}(t)\left(\kappa - [\gamma + \beta \cdot sgn(\dot{u}(t)) \cdot sgn(z(t))] \cdot |z(t)|^n\right) \tag{2.26}$$

In order to fill in the guesses for the state vectors, the shift to discrete time is made. This changes Equation 2.26 to:

$$\mathbf{r} = \dot{\mathbf{z}} - \dot{\mathbf{u}} \circ \left(\kappa - [\gamma + \beta \cdot sgn(\dot{\mathbf{u}}) \circ sgn(\mathbf{z})] \circ |\mathbf{z}|^{\circ n}\right) \tag{2.27}$$

Where $\circ$ stands for element-wise multiplication and $^{\circ n}$ refers to element-wise raising to the n-th power. $\mathbf{r}$ is defined as the discrete-time residual of Equation 2.16. When the size of $\mathbf{r}$ is minimized, the best solution of the response of the element is found. This shift in perspective opens up numerous optimization algorithms.

Based on Equation 2.27, the guess for the solution of $\hat{\mathbf{u}}$ can be updated. For that, AFTHBM moves back to the frequency domain.

2.6.3 Fourier transform and the LM-procedure

Just as a custom IDFT is defined in Equations 2.22-2.25, a custom DFT is defined to get $\mathbf{r}$ back to the frequency domain:

$$\hat{\mathbf{r}} = \begin{bmatrix} \hat{v}_0 & \hat{v}_1 & \hat{w}_1 & \hat{v}_2 & \hat{w}_2 & \cdots & \hat{v}_H & \hat{w}_H \end{bmatrix}^T \tag{2.28}$$

$$\hat{v}_0 = \frac{1}{M} \cdot \mathbf{r}^T \cdot \mathbf{1} \tag{2.29}$$

$$\hat{v}_{\mathrm{k}} = \frac{2}{M} \cdot \mathbf{r}^T \cdot cos(\mathrm{k}\Omega\mathbf{t}) \tag{2.30}$$

$$\hat{w}_{\mathrm{k}} = \frac{2}{M} \cdot \mathbf{r}^T \cdot sin(\mathrm{k}\Omega\mathbf{t}) \tag{2.31}$$

where $\mathbf{1}$ is a vector with all ones. $\hat{\mathbf{r}}$ shows the distribution of the calculation error over the different analysis frequencies. With this information, we will update our guess of $\hat{\mathbf{u}}$. A relation between $\hat{\mathbf{r}}$ and $\hat{\mathbf{u}}$ is needed. A Newton-like method is used to solve this piece of the puzzle, which is why a Jacobian $\hat{\mathbf{J}}$ is needed:

$$\hat{\mathbf{J}} = \frac{\delta\hat{\mathbf{r}}}{\delta\hat{\mathbf{u}}} \tag{2.32}$$

Again, $\hat{\mathbf{J}}$ can not be found directly. $\hat{\mathbf{J}}$ can not be defined in the frequency domain, because Equation 2.27 can not be defined in the frequency domain. The Jacobian is calculated at each moment in time:

$$\mathbf{J} = \frac{\delta\mathbf{r}}{d\hat{\mathbf{u}}} \tag{2.33}$$

We then transform the result into the frequency domain with a similar IDFT as Equations 2.28-2.31. $\mathbf{r}$ is not directly dependent on $\hat{\mathbf{u}}$. $\mathbf{r}$ is dependent on $\dot{\mathbf{u}}$, $\mathbf{z}$ and $\dot{\mathbf{z}}$ however, which means the chain rule of differentiation is applied:

$$\frac{\delta\mathbf{r}}{\delta\hat{\mathbf{u}}} = \frac{\delta\mathbf{r}}{\delta\dot{\mathbf{u}}} \cdot \frac{\delta\dot{\mathbf{u}}}{\delta\hat{\mathbf{u}}} + \frac{\delta\mathbf{r}}{\delta\mathbf{z}} \cdot \frac{\delta\mathbf{z}}{\delta\hat{\mathbf{u}}} + \frac{\delta\mathbf{r}}{\delta\dot{\mathbf{z}}} \cdot \frac{\delta\dot{\mathbf{z}}}{\delta\hat{\mathbf{u}}} \tag{2.34}$$

Derivation of these separate parts of the Jacobian $\mathbf{J}$ and transformation to $\hat{\mathbf{J}}$ are included as Appendix A.

The classical Newton method uses the Jacobian $\hat{\mathbf{J}}$ in the following way:

$$\hat{\mathbf{u}}^{j+1} = \hat{\mathbf{u}}^j - \hat{\mathbf{J}}^{-1} \cdot \hat{\mathbf{r}} \tag{2.35}$$

where j indicates the j-th iteration of the result.

A large weakness can be spotted here: when $\hat{\mathbf{J}}$ is singular or near-singular. Especially during early iterations, this turns out to be the case for the Bouc-Wen element. [Wong et al., 1994a] suggests to therefore apply another Newton-like method designed for singular and near-singular problems. This method is called the Levenberg-Marquardt (LM) procedure and follows the following equation:

$$\hat{\mathbf{u}}^{j+1} = \hat{\mathbf{u}}^j - \left(\hat{\mathbf{J}}^T \cdot \hat{\mathbf{J}} + \phi^j \cdot \mathbf{I}\right)^{-1} \cdot \hat{\mathbf{J}}^T \cdot \hat{\mathbf{r}} \tag{2.36}$$

ϕ^j indicates a regularization parameter. When $\phi^j = 0$, we are basically following the classical Newton method. As the other limit (ϕ^j very large), a method of gradient descent is performed. The method of gradient descent is very stable but very slow. The LM-procedure is a mix of the 2 methods and will adapt to what degree both methods are used to find the next iteration step.
An updated guess for $\hat{\mathbf{u}}$ is now found. The updated guess is used in Equation 2.20 and procedure is repeated from there. Whenever the solution has converged, the algorithm is terminated and the final $\hat{\mathbf{u}}$ is stored. The convergence criterion used is:

$$||\hat{\mathbf{r}}|| < \epsilon \tag{2.37}$$

where ϵ is chosen based on the accuracy required from the calculation.

2.6.4 Summary

With all calculation steps laid out in previous chapters, a broader overview of AFTHM is presented. All segments of the solution strategy are listed, highlighting core outcomes, warnings and bottlenecks of each segment. Figure 2.5 (after [van der Esch, 2020]) summarizes the AFTHBM procedure in a flow chart.

Step 1: Linear calculation $\hat{\mathbf{u}}$
This initial step involves a relatively easy frequency-domain calculation. The linear solution is the starting point of the procedure because linear result will be sufficiently close to the final answer. The correct frequency domain representation has to be chosen however (sine-cosine representation), as other steps require real-valued state variables.

Step 2: Calculate $\hat{\mathbf{z}}$
In this step, the response of the Bouc-Wen element is split up into a linear stiffness and a hysteretic stiffness. This step is again linear, $\hat{\mathbf{u}}$ and $\hat{\mathbf{f}}_{\mathbf{ex}}$ can be directly used to get the answer.

Step 3: IDFT, calculate $\hat{\dot{\mathbf{u}}}$, $\hat{\mathbf{z}}$, $\hat{\dot{\mathbf{z}}}$
Through a custom IDFT, the state variables are defined in the time domain. An important variable is M, which defines the amount of samples to evaluate in the time domain. M directly influences accuracy of further steps, but is also the main bottleneck for calculation speed.

Step 4: Calculate J and r
A quantification of how well approximation of $\hat{\mathbf{z}}$ matches the nonlinear ODE of the Bouc-Wen model is made. Next to that, we calculate in what direction to look for a better solution. Both are done in the time domain, as a frequency-domain representation is impossible. The main bottleneck is the calculation of J. For each time moment $6 \cdot (2H+1)$ different derivatives have to be calculated.

Step 5: DFT, Calculate $\hat{\mathbf{J}}$ and $\hat{\mathbf{r}}$
As preparation for the LM-procedure, both $\mathbf{J}$ and $\mathbf{r}$ are transformed to the frequency domain. Whereas calculating $\hat{\mathbf{r}}$ is quick, $\hat{\mathbf{J}}$ is again slowing down the calculation.

Step 6: Update $\hat{\mathbf{u}}$ with LM-procedure
All of the components to update the guess for $\hat{\mathbf{u}}$ are now calculated. The LM-procedure adaptively applies regularization to the optimization in order to solve the ill-conditioned problem of updating $\hat{\mathbf{u}}$. Picking the correct constraints on when to add more or less regularization is key here.

Step 7: Is $||\hat{\mathbf{r}}||$ small enough?
Lastly, $||\hat{\mathbf{r}}||$ is calculated and judge if our fit is good enough. If we meet the convergence criterion, we terminate the algorithm. Otherwise the algorithm returns to Step 2 and the procedure is repeated from there. Determining the correct convergence criterion is important here, as a too loose criterion creates inaccurate results and a too strict criterion can never be met.

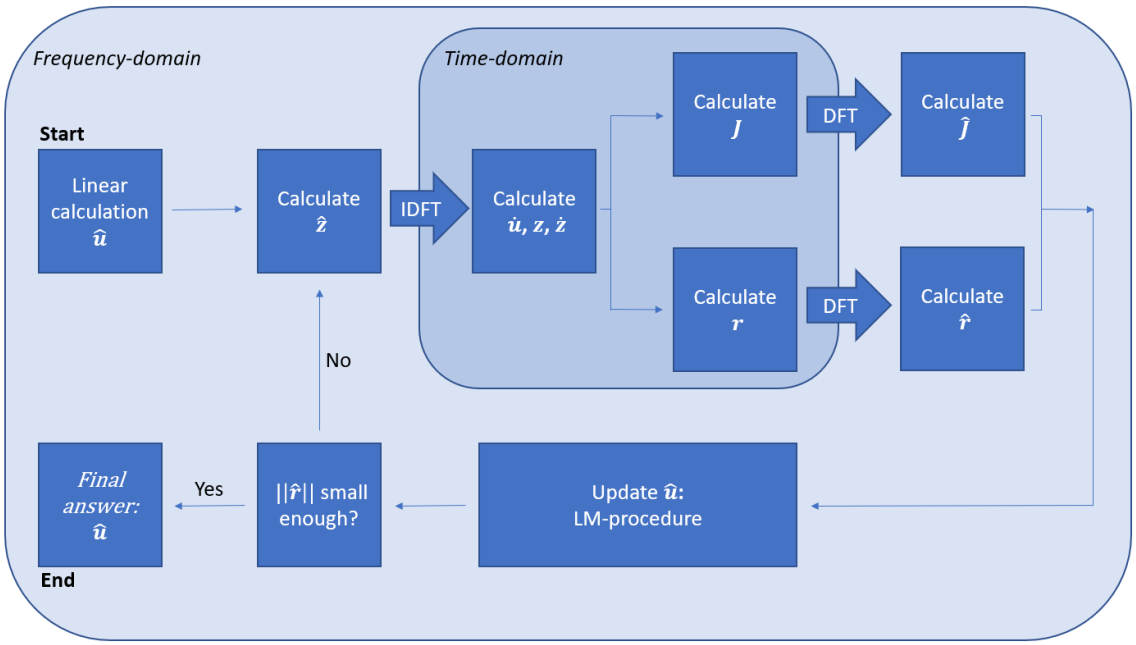

Figure 2.5: Summary of the AFTHBM procedure.

2.7 Comparing AFTHBM and time-integration

The AFTHBM solution strategy is tested with a 1DOF setup. Firstly, the performance of the Bouc-Wen element is tested in isolation (without other sources of damping or attached masses) under harmonic loading. The Bouc-Wen element can be tuned to foundation response data, which means that the stiffness and ultimate strength of the element varies. To assess the behavior of the element for all cases, the physical parameters are chosen such that the yield force (F_y), yield displacement (u_y) and small-strain stiffness (k_i) are all equal to 1.

The Bouc-Wen element also allows control of the post-yielding stiffness (through the parameter α). As soil does not have a post-yielding stiffness, the Bouc-Wen element should also not show this behavior. α can not be set to 0 due to the AFTHBM solution strategy, which is why a very small value of $1E-10$ is chosen.

The shape of the Bouc-Wen hysteresis loop can be changed through the parameters β and γ. The assumption is made that the hysteresis loops generated by the Bouc-Wen element should show linear behavior around reversal points. This assumption is met when β is equal to γ and κ is equal to 1 [Charalampakis, 2010].

2 parameters have the biggest influence on the AFTHBM solution method: H , which is the amount of harmonics considered, and M, which defines the amount of samples taken in the time domain. In order to capture the shape of the hysteresis loop at higher load levels, H is set to 7. Higher amounts of harmonics can be considered, but will both slow down the solution strategy and can cause convergence issues at higher load levels. M is chosen to be 512, which is a large amount of samples to be taken. As no convergence issues arise when M is increased, the choice of this parameter is linked to the computational power available. As long as $M > 2 \cdot H$, calculation errors related to aliasing are prevented. However, to capture the full shape of the Bouc-Wen hysteresis loop in the AFTHBM calculation as best as possible, it is advised to choose an as high as possible M.

The model and solution parameters are summarized in Table 2.1:

Variable	m	c	k	k_i	α	β	γ	κ	n	H	M
Value	0	0	0	1	1E-10	0.5	0.5	1	1	7	512

Table 2.1: Parameter setup for evaluation of a 1DOF Bouc-Wen element.

A harmonic load is applied to the element. Because of the dependency of Bouc-Wen element on the response amplitude, 3 different load levels are applied:

- Low load level: $||\hat{f}_{ex}|| = 0.05$
- Medium load level: $||\hat{f}_{ex}|| = 0.4$
- High load level: $||\hat{f}_{ex}|| = 0.8$

The Bouc-Wen element is rate-independent. Therefore, the frequency of the harmonic excitation has no influence on the response when the element is analyzed in excitation.

Figure 2.6 shows the results of this analysis. The response is investigated with both the AFTHBM strategy and a nonlinear time-integration algorithm. The steady-state behavior of the element is of interest here, therefore the transient response from the nonlinear time-integration results is removed. The left figures of Figure 2.6 show the force in the Bouc-Wen element, set out against the displacement of the element. The right figures show the harmonics of the response (with the 1st harmonic being in the frequency of excitation).

Upon comparing the AFTHBM strategy with the nonlinear time-integration strategy, similar results are found. Whenever a sufficient amount of harmonics are modelled in the AFTHBM strategy, the shape of the hysteresis loop is identical to the time-integration strategy.

With increasing load level, a decreasing secant stiffness and a larger relative size of the hysteresis loop is observed. The 3rd and 5th harmonic in the response also grow with increasing load level. Activation of just the odd harmonics is a common phenomenon for hysteretic systems under harmonic loading, as long as the response shows half-wave symmetry (or equivalently, point-symmetry of the hysteresis loop) [Massopust, 2002]. Important to note here is that the behavior of the Bouc-Wen element is not directly dependent on amplitude of the force but on amplitude of the response. When a mass and a viscous damper are added to the element, this note will become even more important.

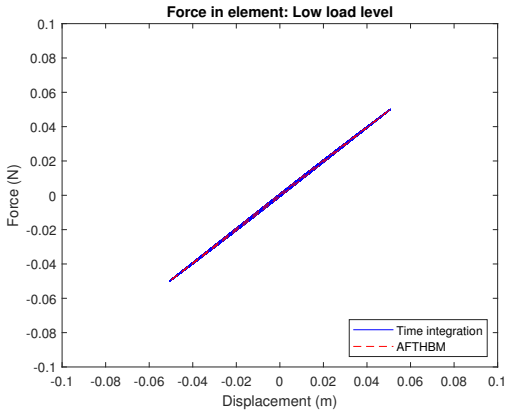

(a)

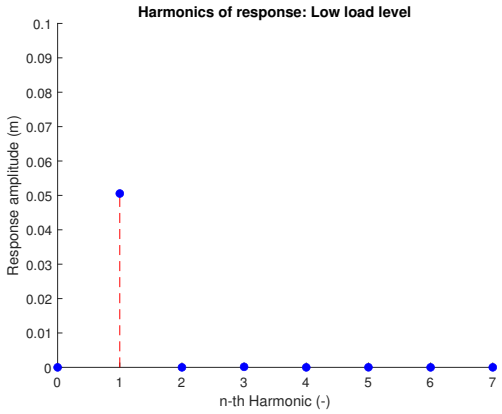

(b)

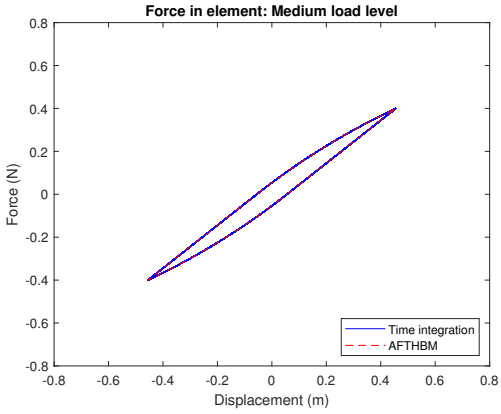

(c)

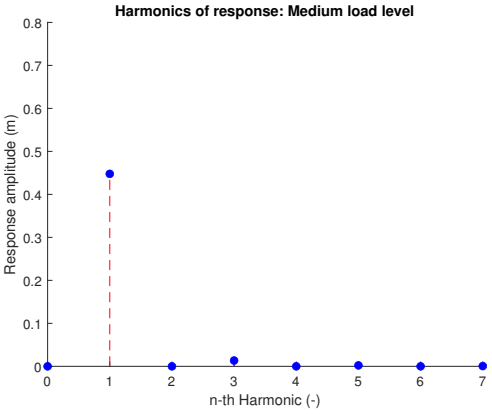

(d)

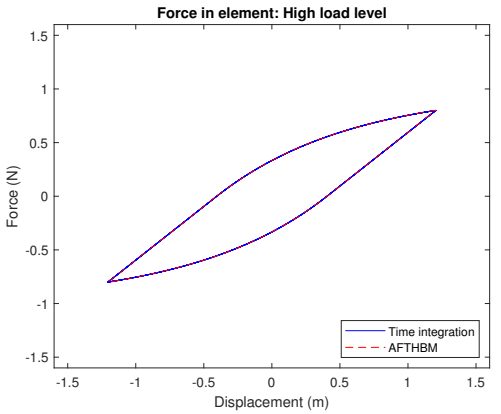

(e)

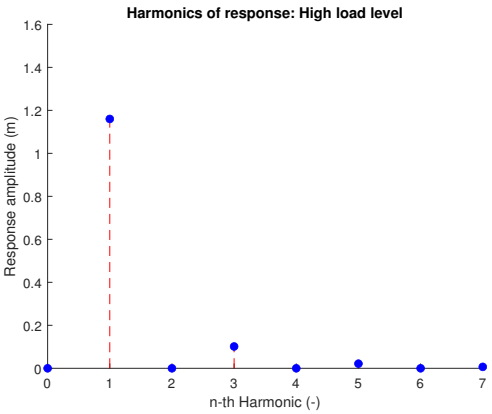

(f)

Figure 2.6: Analyzing the Bouc-Wen element for 3 load levels. The right figures show the harmonics of the response. There is no significant difference in amplitude of the harmonics between the time-integration results and the AFTHBM results.

A mass and a viscous damper are now added to the test setup. The parameters have been chosen such that the resonance frequency ω_0 of the (small-strain) linear system is equal to 1 rad/s. 5 % critical viscous damping is added to the setup.
The model parameters for this updated test setup are summarized in Table 2.2:

Variable	m	c	k	k_i	α	β	γ	κ	n	H	M
Value	1	0.1	0	1	1E-10	0.5	0.5	1	1	7	512

Table 2.2: Parameter setup for evaluation of a 1DOF Bouc-Wen element, including mass and viscous damping.

The same 3 load levels are applied as in the previous test setup. Because of the inclusion of mass and viscous damping however, the system behaves differently with changing frequency of the applied load. The element is again subjected to a harmonic load, where the frequency of the excitation is varied between 0 and 2 rad/s. Results were checked with time-integration analyses. The results were a match for every check performed, for all 3 load levels.

Figure 2.7 shows the results of this test setup. A clear pattern can be observed in Figure 2.7a. At higher load levels, the nonlinear resonance frequency becomes lower. The generated hysteresis loops at higher load levels have a lower secant stiffness, and therefore the structure behaves softer, reducing the nonlinear resonance frequency. Next to that, the hysteresis loop grows in relative size, increasing the hysteretic damping in the system. This results in a wider resonance peak at higher load levels.

As discussed in the setup without added mass and viscous damping, higher load levels also activate higher harmonics. This can be observed in Figure 2.7b. Another effect pops up however, where a resonance peak in the Medium load level is present at $\Omega \approx 0.33\ rad/s$. At the High load level,even more peaks are observed. Similar peaks are observed in Figure 2.7a, although smaller in relative size. These peaks stem from an effect called super-harmonic resonance. Because higher (odd) harmonics are generated, the system can also resonate to those higher harmonics. The placement of the larger peak at $\Omega \approx 0.33\ rad/s$ can be explained by the linear resonance frequency of the system of 1 rad/s In this case, the 3rd harmonic causes resonance. Resonance of the 5th and even the 7th harmonic also shows up in Figure 2.7a.

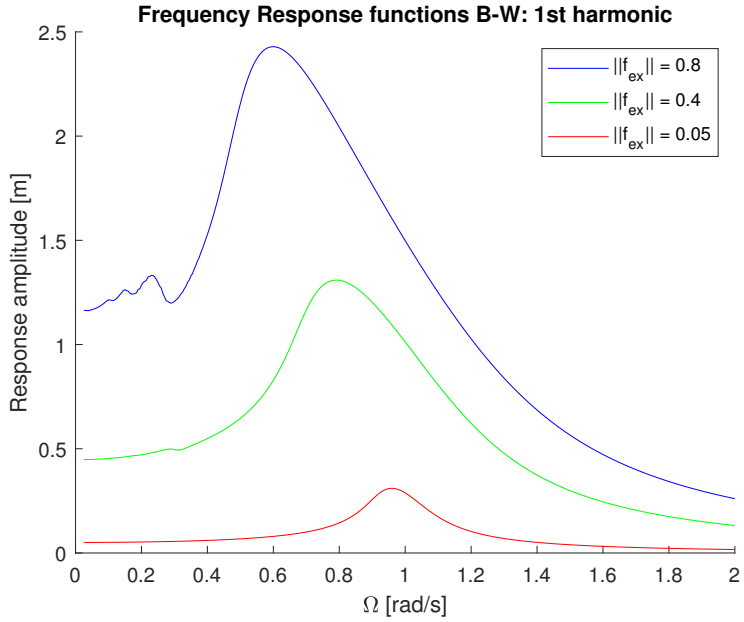

(a)

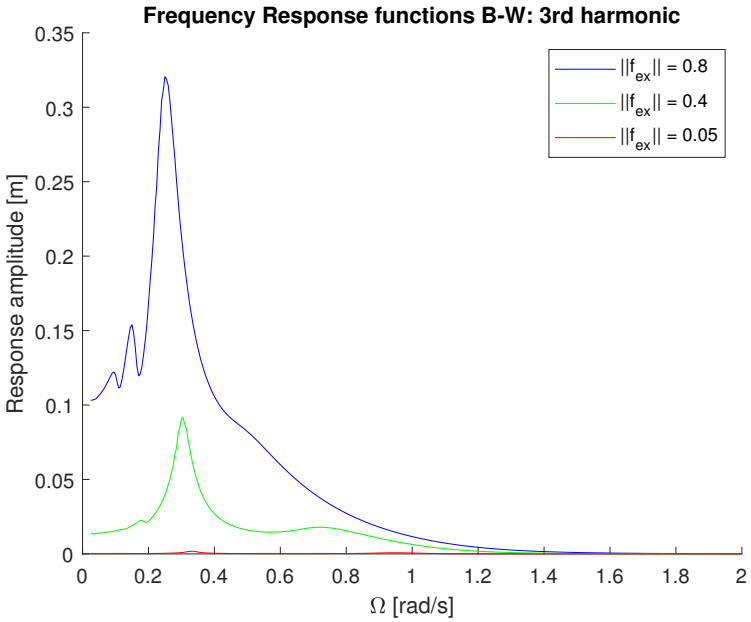

(b)

Figure 2.7: 1st and 3rd Harmonic of the B-W element with added mass and viscous damping.

2.8 Scalability of AFTHBM

Because of the elaborate solution strategy of AFTHBM, these analyses (of 1DOF with 1 harmonic force) already take significant computing power. The interlinked nature of the calculations, all analysis frequencies are solved at the same time, do not allow for time saving strategies like parallel computing. A doubling of the amount of DOFs of the model will approximately octuple the computational effort required, $O(n^3)$. This relation stems from the (fully populated) matrix inversion required in Step 6 of the AFTHBM algorithm (Equation 2.36). A doubling of the amount of analysis frequencies also results in 8 times the computation time because of the same matrix inversion. The end goal is to analyze a full OWT FE model (>100 DOFs), with spectral loading like wave and wind loading (>1000 analysis frequencies). To model the hysteretic behavior of the foundation through AFTHBM at that bigger scale is a large computational challenges. The question also comes up if this level of complexity is needed for the problem at hand. The generation of superharmonics only occurs at higher load levels, while in the Fatigue Limit State such load levels are generally not reached. A simplification of the method could save significant computational effort.

Section 3

Equivalent Linear modeling in the frequency domain

3.1 Simplifying AFTHBM - Equivalent Linear characteristics

The root cause of the high complexity of AFTHBM is the generation of higher harmonics. A closer look at Figure 2.6 reveals that the response of a nonlinear hysteretic element is dominated by the 1st harmonic. The assumption is now made that these higher harmonics can be neglected. For each response amplitude, a single linear complex element $\hat{k}$ (with a real part and an imaginary part) can then describe the response. Analysis of the response can then be split into separate frequencies again, allowing for faster calculations.

Important parameters can be derive from this complex stiffness $\hat{k}$, defining the behavior, are the following:

- The linear stiffness, $Re(\hat{k})$
- The hysteretic damping ratio, $Im(\hat{k})/(2 \cdot Re(\hat{k}))$

A range of load amplitudes is applied to the Bouc-Wen element, which leads to a range of equivalent linear approximations. The linear stiffness and hysteretic damping ratio of the equivalent lienar element are shown in Figure 3.1.

Figure 3.2 compares Bouc-Wen hysteresis loops found through the AFHBM algorithm wih the equivalent linear (EQL) approximation. The test setup is the same as in Table 2.1, where no mass and viscous damper are added. Especially for the Low and the Medium load level, the hysteresis loops generated look very similar. Only in the High load level a difference can be seen, because of the influence of the higher harmonics.

Performing a full AFTHBM procedure to find the response of the nonlinear hysteretic element is not necessary anymore. The most important characteristics of the element, namely its stiffness and hysteretic damping, can now be looked up in Figures 3.1a and 3.1b. The only issue is now that the element is dependent on the amplitude of the response, which is not known a priori. The Equivalent Linear Method provides a way of dealing with this issue.

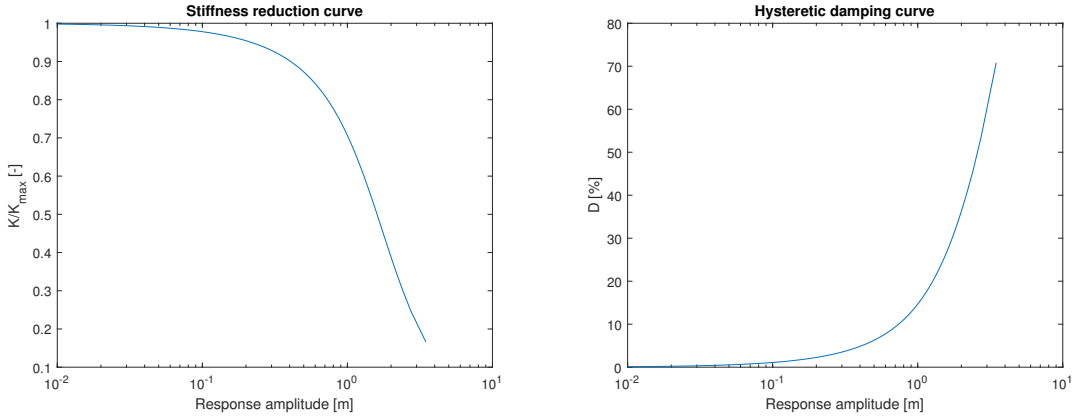

(a) (b)

Figure 3.1: Stiffness reduction and hysteretic damping curves for the Bouc-Wen element.

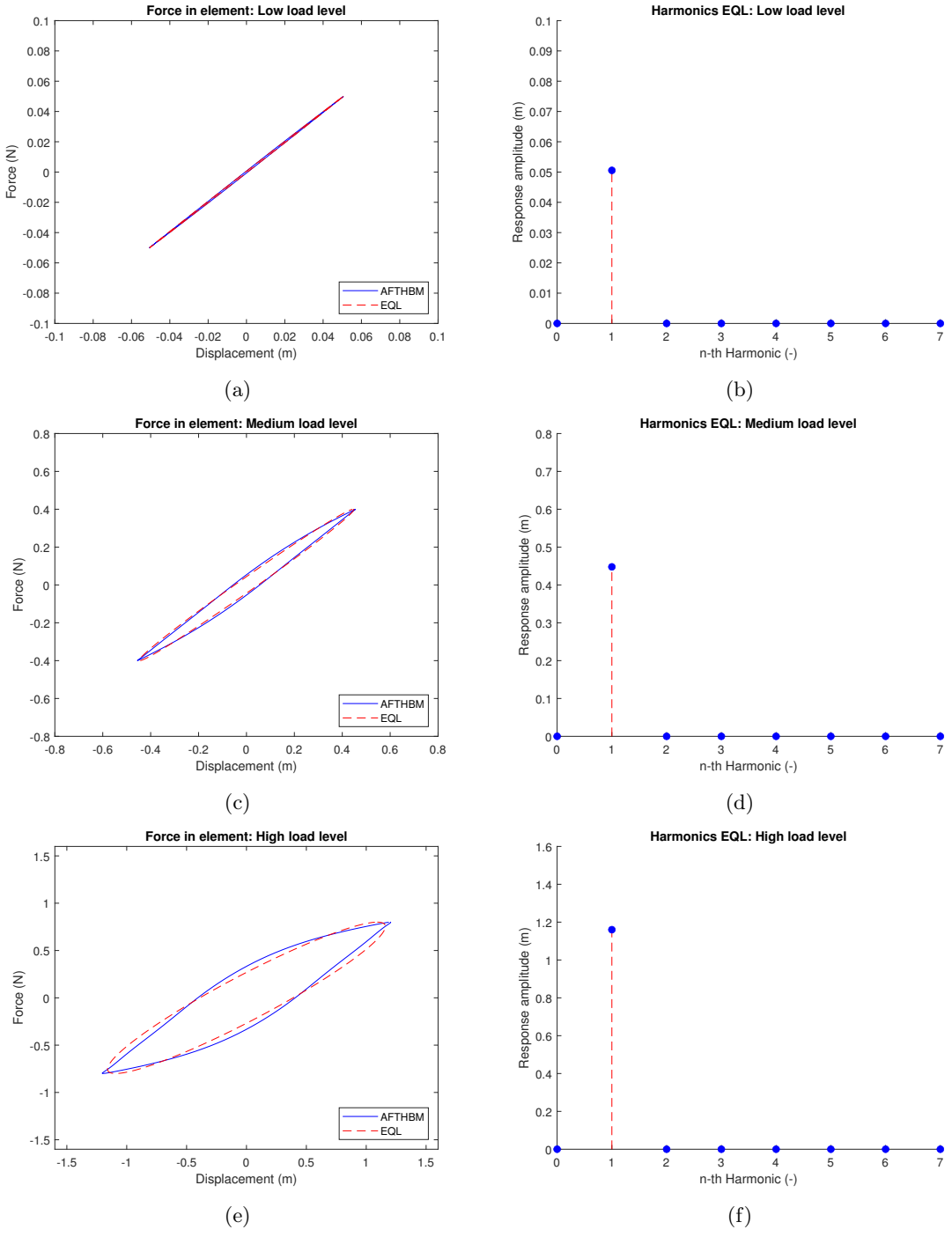

Figure 3.2: Comparing hysteresis loops AFTHBM and EQL for 3 load levels. The figures on the right show the harmonic decomposition of the EQL approximation. Figure 2.6 shows the harmonic decomposition of the AFTHBM results.

3.2 The Equivalent Linear Method

The Equivalent Linear (EQL) Method assumes no higher harmonics are generated and that the response of a nonlinear hysteretic element is dependent on its response amplitude. This allows us to split up the response in the frequency domain. An NDOF formulation for the EQL method is set up, based on a change of Equation 1.6 into:

$$\hat{\mathbf{u}}_k = \left(-k^2\Omega^2\mathbf{M} + ki\Omega\mathbf{C} + \mathbf{K} + \hat{\mathbf{K}}(\mathbf{u}_{ref})\right)^{-1} \cdot \hat{\mathbf{f}}_k = \mathbf{H}(k\Omega, \mathbf{u}_{ref}) \cdot \hat{\mathbf{f}}_k \tag{3.1}$$

where $\hat{\mathbf{K}}(\mathbf{u}_{ref})$ contains all EQL elements with complex stiffness $\hat{k}$ that are dependent on the response amplitudes $\mathbf{u}_{ref}$ in the system. We do however not know the response amplitudes of the system a priori. Also, the definition of a 'response amplitude' is unclear in the case of multiharmonic loading like wind and wave loading.

The issue of not knowing the response amplitudes in advance can be solved by iteratively solving Equation 3.1. A linear response (related to small-strain behavior) is assumed in the first iteration. We evaluate the calculated response, and based on that result the EQL elements in the system are updated. This procedure is repeated until the changes of the deflections in the system drop below an accuracy threshold.

In the case of harmonic loading, the response is also of harmonic nature. $\mathbf{u}_{ref}$ is taken to be the amplitude of the harmonic response. In the case of multiharmonic loading, the deflections in the system are also multiharmonic. A reference response amplitude is chosen that describes the average degree of nonlinearity in the EQL elements over the time window. As the EQL method is also used in earthquake engineering, where spectral loads are also common, a metric for finding this reference response amplitude is known ([Villalobos and Romanel, 2019] and [Pruiksma, 2016]). The deflections are observed in the time domain and 65 % of the observed maximum deflection is taken as $\mathbf{u}_{ref}$.

The EQL method changes the solution flow chart from Figure 1.4 and Figure 2.1. Figure 3.3 shows the iterative nature of the calculation. Next to that, instead of solving for all frequencies at the same time like in HBM, each harmonic component can be analyzed separately in each iteration.

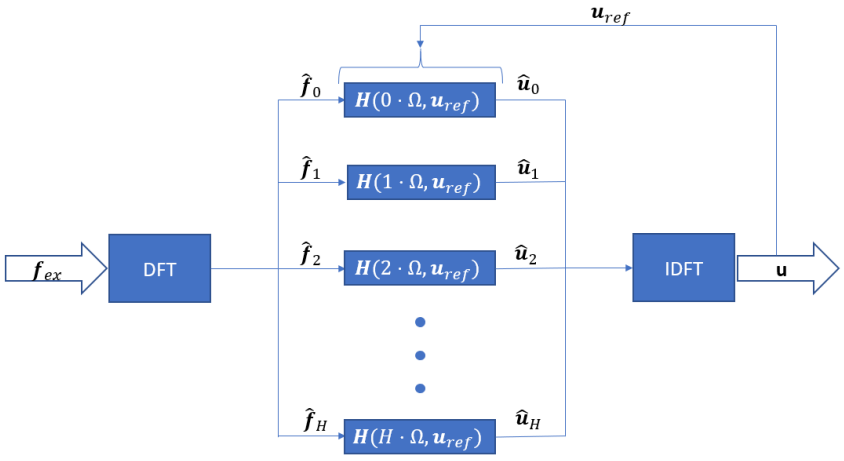

Figure 3.3: Flowchart of the Equivalent Linear Method.

3.3 Comparing EQL to nonlinear methods

3.3.1 Comparison for harmonic loading

In Figure (3.4) the results are shown of an AFTHBM and an EQL investigation. A 1DOF Bouc-Wen element with an added mass and viscous damper is chosen as the test setup (with the properties of Table (2.2)). Harmonic loading is applied, for the same 3 load levels as before. A sweep over forcing frequencies between 0-2 rad/s is again made. Solid lines indicate the AFTHBM results, while dashed lines correspond to the EQL results. Only the response in the 1st harmonic is compared, as EQL assumes no superharmonics are present in the solution.

At a low load level, EQL and AFTHBM find very similar results. The influence of higher harmonics on the response is negligible. For all load levels, EQL captures the softening behavior of the Bouc-Wen element (as can be seen by the peak response amplitude being situated at a lower forcing frequency). For the High load level however, AFTHBM and EQL results differ. The main peaks do not line up and superharmonic resonance is not present in the EQL results. Above 1 rad/s alignment for AFTHBM and EQL is observed. The lower response amplitude at higher frequencies causes higher harmonics in the nonlinear hysteretic element.

The harmonics found through AFTHBM are analyzed. The following areas are investigated: 0-1 rad/s for the High load level, and 0.6-1 rad/s for the Medium load level. These areas show a difference in response amplitude of the 1st harmonic. These regions have one property in common: EQL and AFTHBM differ in response whenever the amplitude of the higher harmonics is larger than 5-10 % of the 1st harmonic. We state a general observation where EQL and AFTHBM find similar results whenever the amplitude of the higher harmonics in the response is **at least one order of magnitude smaller** than the amplitude of the 1st harmonic.

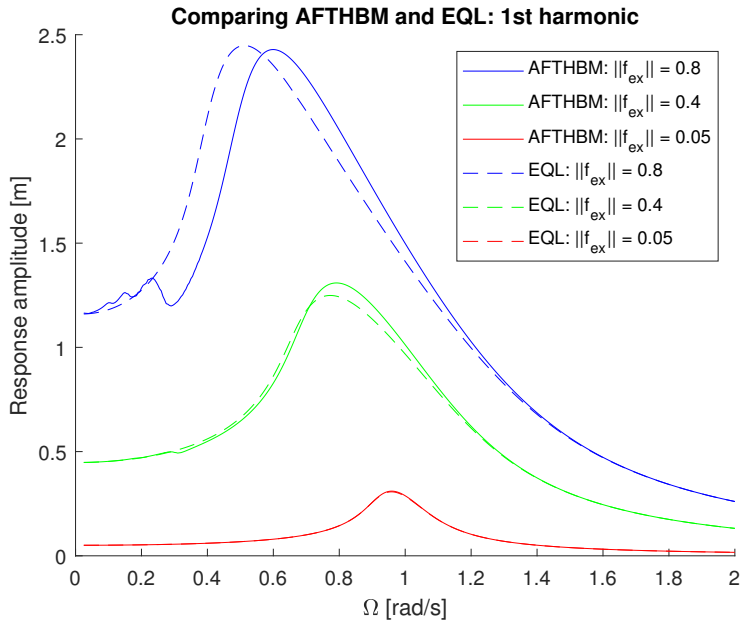

Figure 3.4: Comparing FRF's AFTHBM and EQL for 3 load levels.

3.3.2 Comparison for multiharmonic loading

The forcing that is applied to the OWT is wave and wind loading, which are both multiharmonic loads. Therefore, the EQL solution strategy is checked in 1DOF for multiharmonic loads as well. As mentioned before, the response of the element will also be of multiharmonic nature. Therefore, one can not simply define the response amplitude as the amplitude of a harmonic. The measure of 65 % of the maximum observed deflection in the time domain ([Villalobos and Romanel, 2019] and [Pruiksma, 2016]) is used.

The multiharmonic loading that is applied is a zero mean white noise load. All analysis frequencies have the same force amplitude, apart from the force at 0 Hz. Figure 3.5 shows the load in both the time domain and the frequency domain.

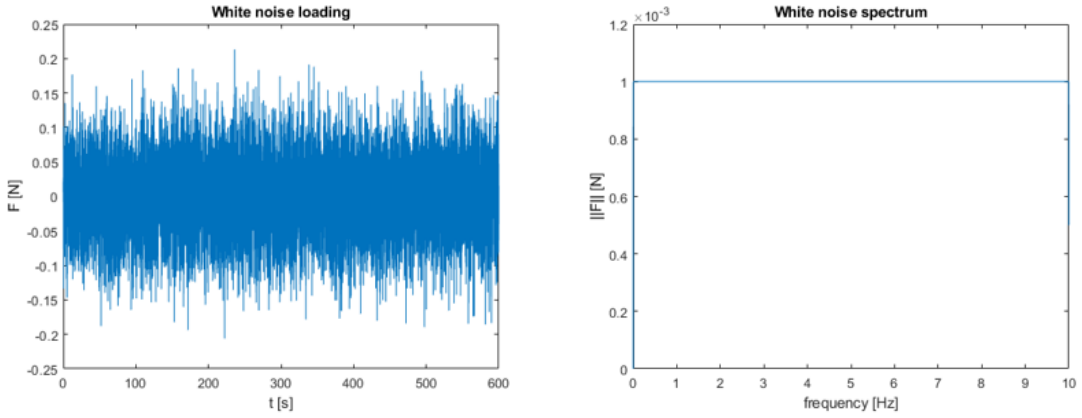

(a) (b)

Figure 3.5: Applied white noise loading.

Figure 3.6 shows the deflection spectra for the Bouc-Wen element with added mass and viscous damping under white noise loading. Figure 3.6a shows the result of a Linear analysis, while Figure 3.6b shows the result of an EQL analysis. The reference used is from a nonlinear time integrator. The EQL method shows a better fit for the main resonance peak.

One part of the response can not be replicated, which is the larger amplitudes at very low analysis frequencies. As the nonlinear time integrator models the hysteretic behavior directly, permanent deformations occur when larger response amplitudes are reached. As the element is evaluated in isolation, this permanent deformation is not counteracted. The EQL method can not replicate these permanent deformations. It is not expected for these permanent deformations to affect the results of the EQL analysis in NDOF however. At FLS load levels, permanent deformations do not have a large effect on the foundation response. Larger deflection amplitudes are reached in the foundation close to mud-line, possibly causing permanent deformations, but soil elements deeper into the foundation will counteract this deformation by reacting linearly and bringing the foundation back to equilibrium.

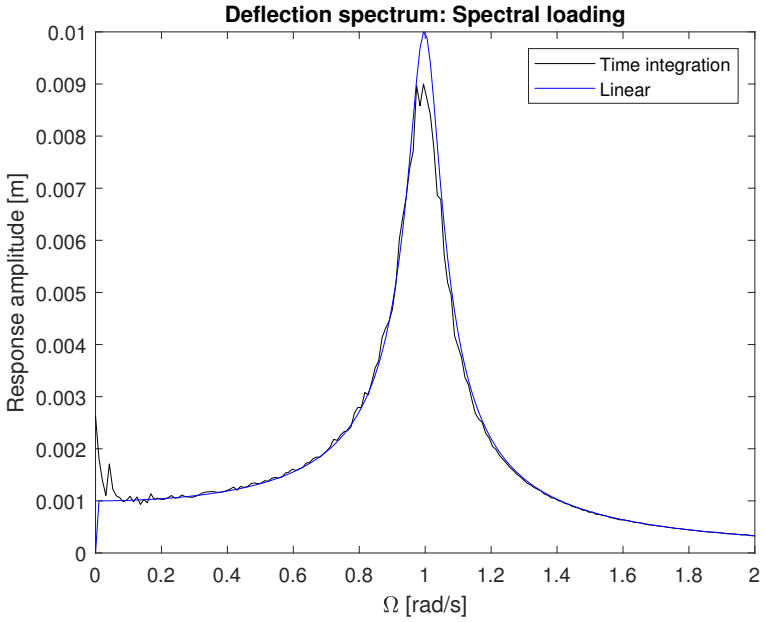

(a)

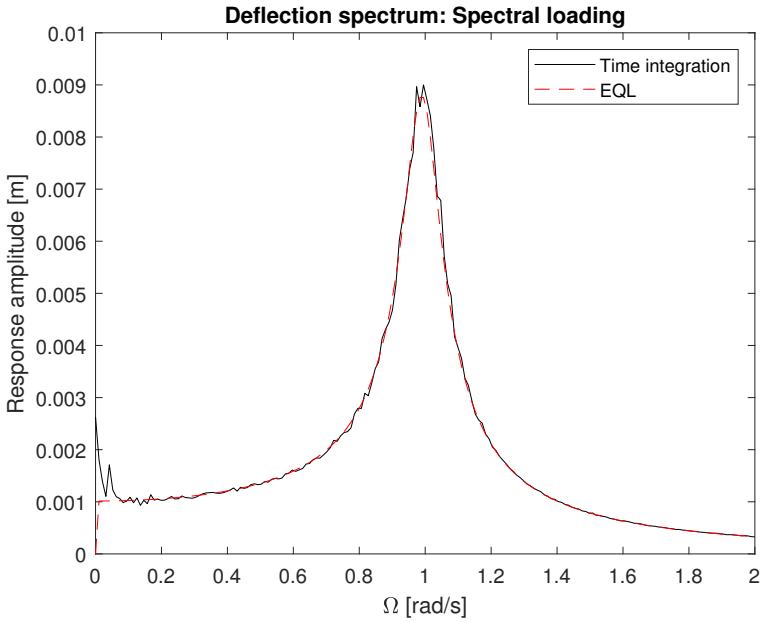

(b)

Figure 3.6: Comparing response spectra for white noise loading.

3.4 Scalability of EQL

In Section 2.8 the complexity of the AFTHBM is analyzed. The complexity to both DOFs and analysis frequencies of AFTHBM is $O(n^3)$, meaning a doubling of either DOFs or analysis frequencies would take 8 times as much computational power. The EQL algorithm has a reduced complexity because of 2 reasons:

- The matrices in the EQL algorithm, which are the matrices from Equation 3.1 are all sparse (with a limited maximum bandwidth). The origin of the sparse matrices is the limited amount of entries coming from the FE formulation in combination with the 1D nature of the OWT. Elements are only connected to their neighbours. Sparse matrix solvers allow for an efficient solution method.
- The core frequency-domain part of the algorithm can be calculated for each analysis frequency separately.

Because of the sparse matrices, more efficient solvers can be used to calculate the responses per analysis frequency. Instead of $O(n^3)$ with respect to DOFs, this algorithm has a complexity of $O(n^2)$ (Equation 3.1 requires solving a sparse system of equations, which has this complexity). Although the core EQL frequency-domain iterations are of complexity $O(n)$ with respect to analysis frequencies, the complexity of the full algorithm with respect to analysis frequencies is $O(nlogn)$. Each iteration we also need the deflections in the time domain to determine the reference deflection amplitude. The transformation to the time domain requires an IDFT which is of complexity $O(nlogn)$.

An EQL strategy is therefore more suitable analyzing a dynamical system with $>$100 DOFs for $>$1000 analysis frequencies. The algorithm has a significantly reduced complexity with respect to AFTHBM, has a good performance with respect to multiharmonic loading and is a proven concept in other domains ([Villalobos and Romanel, 2019] and [Pruiksma, 2016]). It is also expected that higher harmonics do not dominate the response for OWTs under FLS conditions, allowing for the EQL approximation to be made. The EQL method is chosen as the solution strategy for the full OWT support structure.

Section 4

Fitting a nonlinear hysteretic model to soil reaction data

4.1 Available soil reaction data

With the chosen EQL solution strategy, a nonlinear hysteretic model has to be chosen that represents soil behavior around an OWT monopile foundation. The available soil reaction data consists of a set of p-y curves (Section 1.4.2) that were fitted to a monopile foundation in sandy soil conditions. A 3D soil body was evaluated in monotonic loading and was then used to calibrate the p-y curves. An extra reduction factor was applied to take the cyclic behavior of the foundation into account.

Two nonlinear hysteretic constitutive models are fitted to the p-y curves: the Masing model and the Bouc-Wen model of hysteresis. Both fitting strategies are explained and an EQL approximation is made of both models. The stiffness and hysteretic damping curves are extracted and compared to existing literature.

4.2 Fitting the Masing model

As discussed in Section 2.4, the Masing rules define the generation of a hysteresis loop by directly looking at the virgin loading curve. The virgin loading curve is defined to be the p-y curve.
The EQL approximation of the Masing model is made by finding the secant stiffness and hysteretic damping ratio of the generated hysteresis loops. The hysteretic damping ratio is based on an energy formulation, following Figure (4.1). As a last step, the complex stiffness $\hat{k}$ is generated from the linear stiffness and hysteretic damping ratio as in Section 3.1.

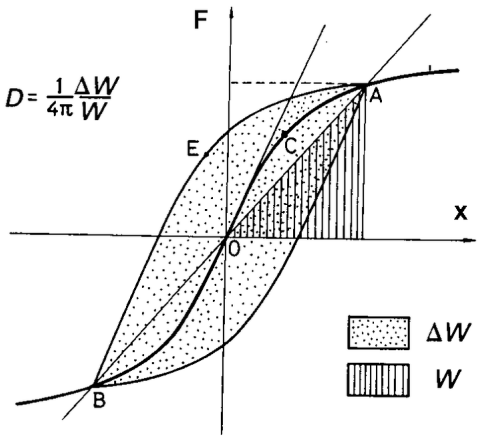

Figure 4.1: Calculating the hysteretic damping ratio, [Bratosin and Sireteanu, 2002].

4.3 Fitting the Bouc-Wen model

Similar the Masing element, the backbone curve of the Bouc-Wen element is fitted to the p-y curves. As the fit is made in monotonic virgin loading, the Bouc-Wen model reduces to a time-independent nonlinear ODE ([Wong et al., 1994a]):

$$\frac{dF}{du} = \alpha k_i + \left(\kappa - [\gamma + \beta] \cdot \left|\frac{F - \alpha k_i \cdot u}{k_i}\right|^n\right) \cdot (1 - \alpha) k_i \tag{4.1}$$

with as boundary condition:

$$F(u = 0) = 0 \tag{4.2}$$

A fitting procedure is followed similar to [Charalampakis, 2010]. The nonlinear ODE is compared to a bilinear model (shown in Figure 4.2). At small deflections (where u approaches 0), F should reduce to the line $k_i \cdot u$. At the same time, at large deflections F should approach the line $F_y + \alpha k_i \cdot u$. Filling in these lines into the ODE, the corresponding constraints are found:

$$\kappa = 1 \tag{4.3}$$

$$\gamma + \beta = \left(\frac{F_y}{k_i}\right)^{-n} \tag{4.4}$$

The shape of the hysteresis loop is determined by the ratio between γ and β. If the stiffness at load reversal is assumed to be equal to k_i (which is also the case for Masing rules), the last constraint is found:

$$\gamma = \beta = \frac{1}{2}\left(\frac{F_y}{k_i}\right)^{-n} \tag{4.5}$$

A bilinear model is firstly fit to the p-y curve. With that bilinear model, all Bouc-Wen parameters can be defined except for one: n. Based on the area under the Bouc-Wen curve and the p-y curve, a bisection method is used to fit the last parameter n. Figure 4.3 shows the bilinear approximation of the p-y curve and the comparison between the fitted Bouc-Wen model and the p-y curve. The steps of Section 3.1 are repeated to find the corresponding stiffness reduction and hysteretic damping curves.

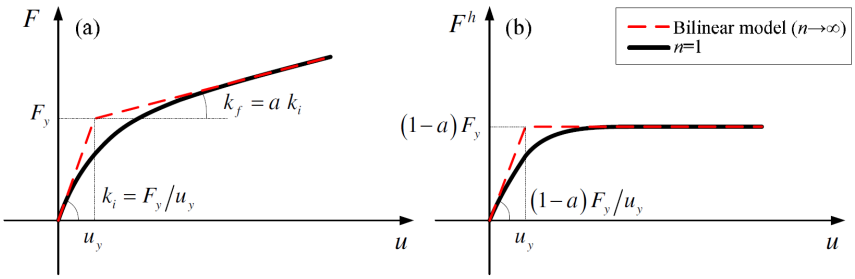

Figure 4.2: The Bouc-Wen model in monotonic loading, when compared to a bilinear model. [Charalampakis, 2010] (a) shows the full Bouc-Wen element, while (b) shows just the hysteretic part.

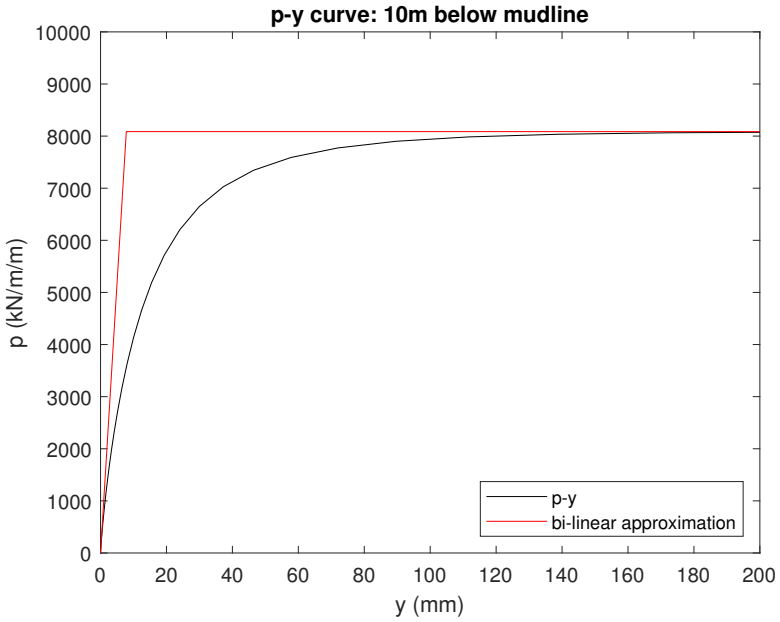

(a)

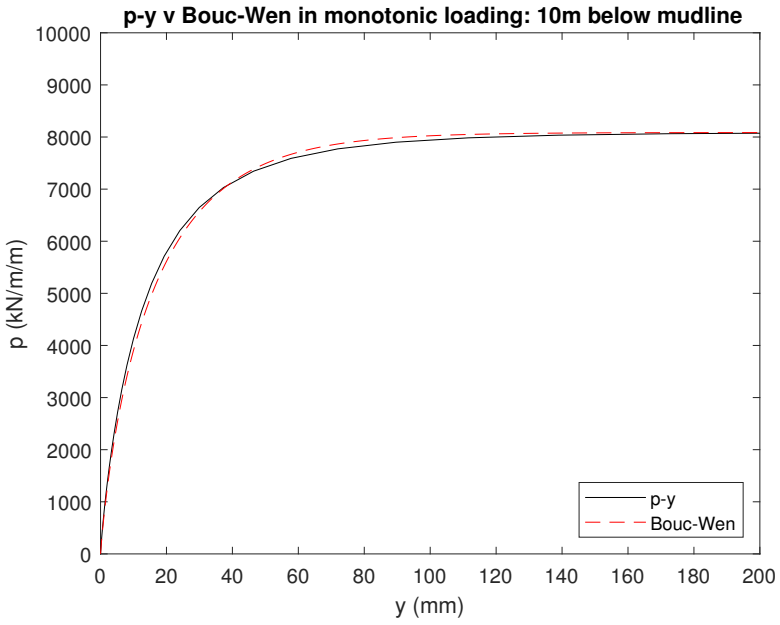

(b)

Figure 4.3: Fitting a B-W model to a p-y curve in monotonic loading.

4.4 Comparing the Bouc-Wen model to the Masing model

The fitted nonlinear hysteretic models are compared for a p-y curve at 10m below mudline. Similar results are found at all foundation depths. Figure 4.4 shows the EQL stiffness reduction curves and hysteretic damping curves of the fitted models.

The stiffness reduction curve of the EQL Masing model is by definition the same as the secant stiffness of the p-y curve itself. Because of the limited amount of datapoints in the p-y curve, the element behaves linearly for all response amplitudes at or below 0.1 mm. This property is made clear by K/K_{max} being 1 at a response amplitude of 10E-4.

The EQL Bouc-Wen model shows a similar stiffness reduction curve. As the behavior at very small strains is fitted to the p-y curves, the Bouc-Wen element already shows some stiffness reduction at a response amplitude of 0.1 mm. An abrupt stop of the curve for the EQL Bouc-Wen element is also observed. Because the method used is **force-controlled**, the behavior of the element can not be modeled past full yielding. No unique solution exists at full yielding of the element in a force-controlled test. A displacement-controlled method is necessary to model the Bouc-Wen model for larger response amplitudes.

The biggest difference between the Masing model and the Bouc-Wen model of hysteresis is the hysteretic damping curve. The EQL Bouc-Wen element consistently yields a higher hysteretic damping ratio than the Masing rules. Damping ratios even increase to over 70 % at larger response amplitudes. The EQL Masing element yields lower damping ratios, but still hits damping ratios above 50 % for extreme response amplitudes.

The overdamping of the Masing rules at larger strain levels is a well-known disadvantage [Yniesta and Brandenberg, 2015]. Observed damping ratios in monopile foundations generally lie between 5 - 15 % [Beuckelaers, 2017], with maximum damping ratios at large strains reaching up to 20 % [Yniesta and Brandenberg, 2015].

Although the stiffness reduction curves of both models behave similarly to the p-y curves, too high damping ratios are observed for both models. We choose to move forward with the Masing model due to the perfect match of the stiffness curve and a lower hysteretic damping curve. To make sure no unrealistic damping ratios are reached in the NDOF analysis, a cap of 20 % is applied to the hysteretic damping curves generated by the Masing model.

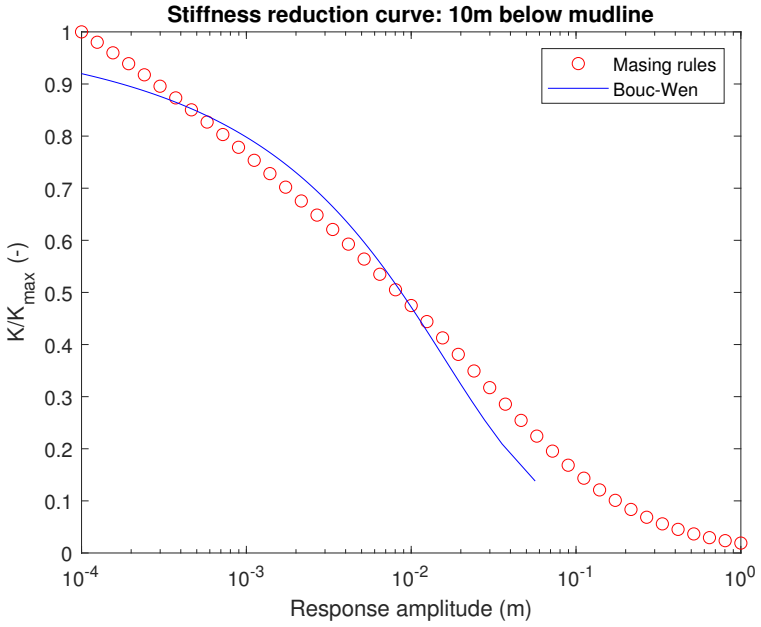

(a)

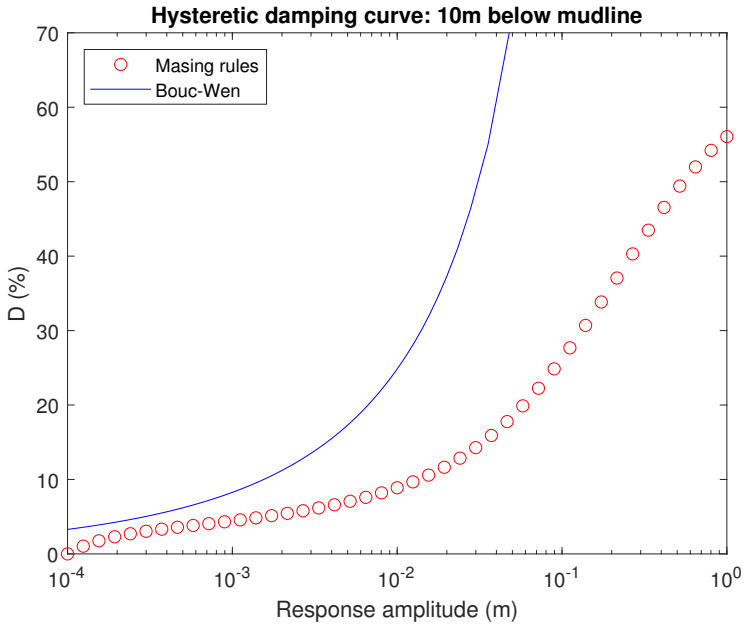

(b)

Figure 4.4: Comparison between B-W and Masing in cyclic loading.

Section 5

Setting up a suitable Finite Element formulation

5.1 The Finite Element setup

The next step towards assessing a full OWT is made. A fitting finite element formulation is needed that can be used in an EQL analysis. With a proper finite element definition, an accurate discretization of the spatial domain is reached. The following aspects should be included in the element:

- Stiffness of the monopile and tower (with Timoshenko beam elements), with associated distributed mass and distributed mass moment of inertia.
- The effect of the dead weight of structure on the behavior of the system, negatively effecting the resistance of the structure to bending and shear deformations. This effect is called the geometric stiffness effect.
- Added distributed masses (due to for example displaced water mass and soil mass).
- Added nodal masses and mass moments of inertia.
- Distributed (complex-valued) soil stiffness, changing every iteration of the equivalent linear calculation.
- Nodal and distributed external loads on the structure.

The element can be defined as follows:

$$\mathbf{M}_e \cdot \ddot{\mathbf{u}}_e + (\mathbf{K}_{e,struc} + \mathbf{K}_{e,geom}) \cdot \mathbf{u}_e + \hat{\mathbf{K}}_{e,soil} \cdot \mathbf{u}_e = \mathbf{f}_{e,ex} \tag{5.1}$$

Notation from [Wells, 2009] is followed. The derivation starts at the integrals required for calculation of the elements.

5.1.1 Displacement and acceleration vectors

Vital to every finite element method is definition of the shape functions used. Shape functions related to both deflections and rotations are needed. As Timoshenko beam elements are used, C_0-continuous shape functions are required [Wells, 2009]. To keep further implementation relatively straightforward, 1st-order shape functions are used. To make sure an accurate discretization is made, a small element size is recommended. The shape functions between node 1 and node 2 of an element are defined as follows:

$$N_1^u = N_1^\theta = \frac{\mathrm{z}_2 - \mathrm{z}}{h}, \mathrm{z}_1 \leq \mathrm{z} \leq \mathrm{z}_2 \tag{5.2}$$

$$N_2^u = N_2^\theta = \frac{\mathrm{z} - \mathrm{z}_1}{h}, \mathrm{z}_1 \leq \mathrm{z} \leq \mathrm{z}_2 \tag{5.3}$$

$$\mathbf{N} = \begin{bmatrix} N_1^u & N_2^u & N_1^\theta & N_2^\theta \end{bmatrix} \tag{5.4}$$

Where h stands for the element length. As derivatives of the shape functions with respect to z are also used, these are defined as well:

$$B_1^u = B_1^\theta = -\frac{1}{h} \tag{5.5}$$

$$B_2^u = B_2^\theta = \frac{1}{h} \tag{5.6}$$

$$\mathbf{B} = \begin{bmatrix} B_1^u & B_2^u & B_1^\theta & B_2^\theta \end{bmatrix} \tag{5.7}$$

With the specified shape functions, element deflection and rotation fields are defined:

$$u_e^h = \mathbf{N} \cdot \mathbf{u}_e, \mathbf{u}_e = \begin{bmatrix} u_1^u & u_2^u & u_1^\theta & u_2^\theta \end{bmatrix}^T \tag{5.8}$$

$$\ddot{u}_e^h = \mathbf{N} \cdot \ddot{\mathbf{u}}_e, \ddot{\mathbf{u}}_e = \begin{bmatrix} \ddot{u}_1^u & \ddot{u}_2^u & \ddot{u}_1^\theta & \ddot{u}_2^\theta \end{bmatrix}^T \tag{5.9}$$

5.1.2 The Mass matrix

The integrals required for the elemental mass matrix are as follows:

$$\mathbf{M}_e = \begin{bmatrix} \mathbf{M}_e^{uu} & \mathbf{0} \\ \mathbf{0} & \mathbf{M}_e^{\theta\theta} \end{bmatrix} \tag{5.10}$$

$$\mathbf{M}_e^{uu} = \int_{\Gamma_{e,M}} \mathbf{N}^{uT} M_n \mathbf{N}^u d\Gamma + \int_{\Omega_e} \mathbf{N}^{uT} \rho A \mathbf{N}^u d\Omega \tag{5.11}$$

$$\mathbf{M}_e^{\theta\theta} = \int_{\Gamma_{e,I}} \mathbf{N}^{\theta T} I_n \mathbf{N}^\theta d\Gamma + \int_{\Omega_e} \mathbf{N}^{\theta T} \rho I \mathbf{N}^\theta d\Omega \tag{5.12}$$

with M_n and I_n being the nodal masses and mass moments of inertia that have to be added to the structure. Added distributed masses and mass moments of inertia are summed up in ρA and ρI. Evaluation of these integrals (assuming constant ρA and ρI over the element) results in the following elemental mass matrix:

$$\mathbf{M}_e = \begin{bmatrix} M_1 + \frac{\rho A h}{3} & \frac{\rho A h}{6} & 0 & 0 \\ \frac{\rho A h}{6} & M_2 + \frac{\rho A h}{3} & 0 & 0 \\ 0 & 0 & I_1 + \frac{\rho I h}{3} & \frac{\rho I h}{6} \\ 0 & 0 & \frac{\rho I h}{6} & I_2 + \frac{\rho I h}{3} \end{bmatrix} \tag{5.13}$$

5.1.3 The Structural Stiffness matrix

The integrals required for the elemental stiffness matrix related to the structure (from [Wells, 2009]) are as follows:

$$\mathbf{K}_{e,struc} = \begin{bmatrix} \mathbf{K}_e^{uu} & \mathbf{K}_e^{u\theta} \\ \mathbf{K}_e^{\theta u} & \mathbf{K}_e^{\theta\theta} \end{bmatrix} \tag{5.14}$$

$$\mathbf{K}_e^{uu} = \int_{\Omega_e} \mathbf{B}^{uT} G A_s \mathbf{B}^u d\Omega \tag{5.15}$$

$$\mathbf{K}_e^{u\theta} = -\int_{\Omega_e} \mathbf{B}^{uT} G A_s \mathbf{N}^\theta d\Omega \tag{5.16}$$

$$\mathbf{K}_e^{\theta u} = -\int_{\Omega_e} \mathbf{N}^{\theta T} G A_s \mathbf{B}^u d\Omega \tag{5.17}$$

$$\mathbf{K}_e^{\theta\theta} = \int_{\Omega_e} \mathbf{B}^{\theta T} E I \mathbf{B}^\theta d\Omega + \int_{\Omega_e} \mathbf{N}^{\theta T} G A_s \mathbf{N}^\theta d\Omega \tag{5.18}$$

To counteract possible shear locking, reduced (1-point) integration is applied to the component related to shear deformation in $\mathbf{K}_e^{\theta\theta}$. Evaluating the integrals results in the following elemental stiffness matrix:

$$\mathbf{K}_{e,struc} = \begin{bmatrix} \frac{GA_s}{h} & -\frac{GA_s}{h} & \frac{GA_s}{2} & \frac{GA_s}{2} \\ -\frac{GA_s}{h} & \frac{GA_s}{h} & -\frac{GA_s}{2} & -\frac{GA_s}{2} \\ \frac{GA_s}{2} & -\frac{GA_s}{2} & \frac{EI}{h} + \frac{GA_s h}{4} & -\frac{EI}{h} + \frac{GA_s h}{4} \\ \frac{GA_s}{2} & -\frac{GA_s}{2} & -\frac{EI}{h} + \frac{GA_s h}{4} & \frac{EI}{h} + \frac{GA_s^2 h}{4} \end{bmatrix} \tag{5.19}$$

5.1.4 The Geometric stiffness matrix

Because of the dead weight on the elements of the tower and the monopile, the resistance to bending and shear deformation of the elements is decreased. [Wilson, 2000] explains a strategy to take this geometric stiffness effect into account in dynamic analyses, as long as the axial loads are constant. Another simplification that is made is that the axial load in an element is defined by the axial load of the node with the highest elevation. Distributed masses associated with the element itself are therefore not taken into account. The integral required for the geometric stiffness matrix is as follows:

$$\mathbf{K}_{e,geom} = \begin{bmatrix} \mathbf{K}^{uu}_{e,geom} & \mathbf{0} \\ \mathbf{0} & \mathbf{0} \end{bmatrix} \tag{5.20}$$

$$\mathbf{K}^{uu}_{e,geom} = \int_{\Omega_e} \mathbf{B}^{u\,T} N \mathbf{B}^u d\Omega \tag{5.21}$$

Note here that the axial load N is defined to be positive in extension. After evaluation of the integrals, the resulting geometric stiffness matrix becomes:

$$\mathbf{M}_e = \begin{bmatrix} \frac{N}{h} & \frac{-N}{h} & 0 & 0 \\ \frac{-N}{h} & \frac{N}{h} & 0 & 0 \\ 0 & 0 & 0 & 0 \\ 0 & 0 & 0 & 0 \end{bmatrix} \tag{5.22}$$

5.1.5 The Soil Stiffness matrix

The integrals required for the elemental soil matrix are as follows:

$$\hat{\mathbf{K}}_{e,soil} = \begin{bmatrix} \hat{\mathbf{K}}^{uu}_{e,soil} & \mathbf{0} \\ \mathbf{0} & \mathbf{0} \end{bmatrix} \tag{5.23}$$

$$\hat{\mathbf{K}}^{uu}_{e,soil} = \int_{\Omega_e} \mathbf{N}^{u\,T} \hat{k}_{soil}(\mathrm{z}, \mathbf{u}_{ref}) \mathbf{N}^u d\Omega \tag{5.24}$$

Important to note here is the nature of the term $\hat{k}_{soil}(\mathrm{z}, \mathbf{u}_{ref})$. As discussed in Section 3.2, the complex stiffness of the soil at a specific elevation is influenced by calculating $\mathbf{u}_{ref}$ at that elevation. As these soil stiffnesses are only defined in the nodes, a (linear) interpolation is needed to express the stiffness over the element. This interpolation is only valid if the elements are small enough and the reference deflections are similar in amplitude. Evaluation of the integral results in the following soil stiffness matrix:

$$\hat{\mathbf{K}}_{e,soil} = \begin{bmatrix} \frac{\hat{k}_1 h}{4} + \frac{\hat{k}_2 h}{12} & \frac{\hat{k}_1 h}{12} + \frac{\hat{k}_2 h}{12} & 0 & 0 \\ \frac{\hat{k}_1 h}{12} + \frac{\hat{k}_2 h}{12} & \frac{\hat{k}_1 h}{12} + \frac{\hat{k}_2 h}{4} & 0 & 0 \\ 0 & 0 & 0 & 0 \\ 0 & 0 & 0 & 0 \end{bmatrix} \tag{5.25}$$

with $\hat{k}_n$ being the complex soil stiffness at node n.

5.1.6 The Force vector

In our calculations, we will deal with both nodal loads and distributed loads. Important to note here is the nature of the wave load we will apply to the structure. This wave loading is defined as a piecewise linear distributed load, with a changing wave head in each time step. This means that we need a variable integration scheme. Luckily, we only have to convert these wave loads to nodal loads once in our calculation. The integrals we will need to solve are:

$$\mathbf{f}_{e,ex} = \begin{bmatrix} \mathbf{f}^u_{e,ex} \\ \mathbf{0} \end{bmatrix} \tag{5.26}$$

$$\mathbf{f}^u_{e,ex} = \int_{\Omega_e} \mathbf{N}^{uT} f_{wave}(z,t) d\Omega + \int_{\Omega_e} \mathbf{N}^{uT} f_n(t) d\Omega \tag{5.27}$$

With $f_n(t)$ being the applied nodal load at node n. Because $f_{wave}(z,t)$ is piecewise linear, we can solve each linear part separately with a 2-point Gaussian integration scheme. The nodal loads can simply be added to each respective node.

5.2 Adding other sources of damping

Other sources of damping are present in the system as well, like aerodynamic damping and structural damping. Damping ratios are identified for these other damping sources per structural mode. Applying modal damping is not possible however, as the system can not be solved in the modal domain (foundation stiffness and damping properties are dependent on the response amplitude, changing the stiffness matrix with each iteration). A transformation of this modal damping matrix would result in a fully populated damping matrix, severely slowing down the calculation. Therefore, another form of damping called Rayleigh damping is applied. Rayleigh damping is a combination of mass-proportional and stiffness-proportional damping on a global structural scale. Using modal damping ratios of the modes of the structure, the appropriate amount of damping is applied.

Section 6

Verifying the structural model

6.1 Case study setup

In order to evaluate effectiveness of the EQL method in the analyses of OWTs, a custom FE model (called the EQL model) has to be built. To verify the model, a case study FE model by SGRE is used. This case study is directly related to the p-y curves used to fit a nonlinear hysteretic model to soil reaction data. Table 6.1 shows general properties of the case study OWT. The definition of the different properties is related to Figure 6.1.

Tower	
Tower height	125 m
Tower diameter	5-7.5 m
RNA mass	800000 kg
RNA moment of inertia	260000000 kgm^2
Sub structure	
Sub structure height	50 m
Sub structure diameter	7.5-10 m
Submerged height	17 m
Foundation	
Foundation depth	30 m
Foundation diameter	10 m

Table 6.1: General dimensions of the case study OWT.

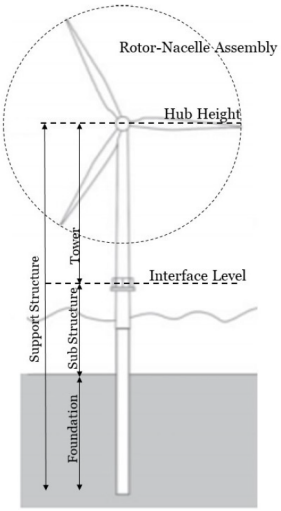

Figure 6.1: Schematization of an OWT, [Hoogstraten, 2019].

The EQL model treats the RNA as a single mass with associated mass moment of inertia. This mass is not located directly at the top of the tower. A rigid link is used to connect the RNA to the rest of the structure. This is a small deviation from the SGRE model, where an empirical stiffness is used to connect the RNA to the tower.

An extra geometric stiffness matrix is used in the EQL model to add the effect of the dead weight of the structure on the resistance to bending deformation and shear deformation. This is also a simplification the SGRE model, where a coupled stiffness matrix is used to couple the horizontal and vertical deflections. This however adds an extra DOF in each node.

Next to the basic structure, the EQL model includes added distributed masses due to the soil plug in the foundation, the entrained water (the body of water inside the structure) and the displaced water (approximated body of water that moves with the structure). Additional point masses are added to model miscellaneous structural elements like ladders and platforms. The SGRE model adds one extra mass we do not include in our model: the marine growth around the sub structure. This marine growth adds a small bit of mass, but it also plays a role in the exact calculation of the wave loading on the structure. As the calculated wave loading is taken as an input, this marine growth is left out of the EQL model.

One final difference is observed between the EQL model and the SGRE model: the order of the shape functions used in the finite element definition. Where the SGRE model uses 3rd order shape functions, the EQL model uses 1st order shape functions. This means that a smaller element size is required in the EQL model in order to achieve the same accuracy. The SGRE model uses a maximum element size of 5 m while the EQL model uses a maximum element size of 1 m in the tower and sub structure, and 0.25 m in the foundation.

6.2 Mode shapes and resonance frequencies

The modal parameters of the SGRE model and the EQL model are now compared. The small-strain behavior of both models, which means that the Winkler foundation behaves linearly with the small-strain stiffness. The results are as follows:

1st tower mode	
SGRE resonance frequency	0.156 Hz
Modal damping (logdec.)	5 %
Modal damping (critical.)	0.80 %
2nd tower mode	
SGRE resonance frequency	0.826 Hz
Modal damping (logdec.)	5.5 %
Modal damping (critical.)	0.80 %
3rd tower mode	
SGRE resonance frequency	1.625 Hz
Modal damping (logdec.)	5.5 %
Modal damping (critical.)	0.80 %

Table 6.2: Modal parameters of the SGRE model.

Figure 6.2 shows the comparison in modeshapes between the SGRE model and the EQL model. The left figures show the modeshapes of the full structure, while the right figures show a zoom on the modeshape in the foundation. When the resonance frequencies of both models are compared, absolute and relative errors as in Table 6.3 are found.

1st tower mode	
EQL resonance frequency	0.156 Hz
Abolute error	0.05 mHz
Relative error	0.03 %
2nd tower mode	
EQL resonance frequency	0.826 Hz
Abolute error	0.35 mHz
Relative error	0.04 %
3rd tower mode	
EQL resonance frequency	1.609 Hz
Abolute error	16 mHz
Relative error	0.98 %

Table 6.3: Absolute and relative error: EQL model vs. SGRE model.

The conclusion is made based on the small relative errors that for the purpose of this thesis the EQL model is verified with the SGRE model.

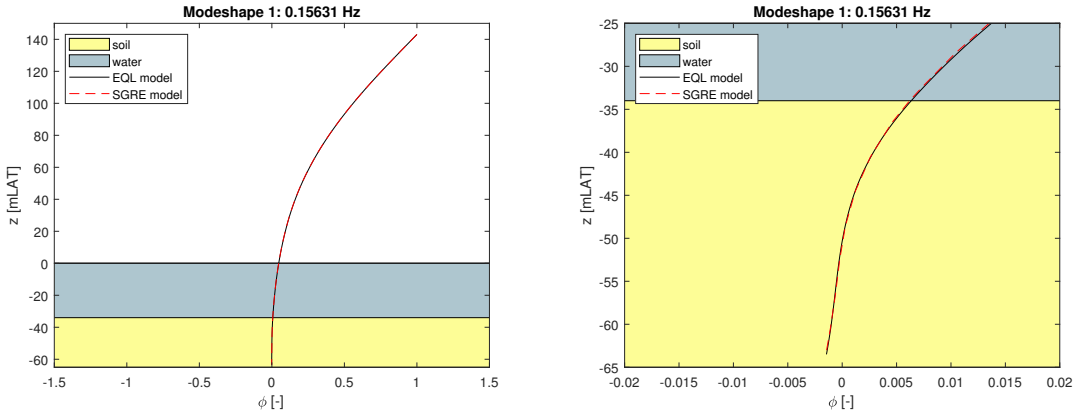

(a)

(b)

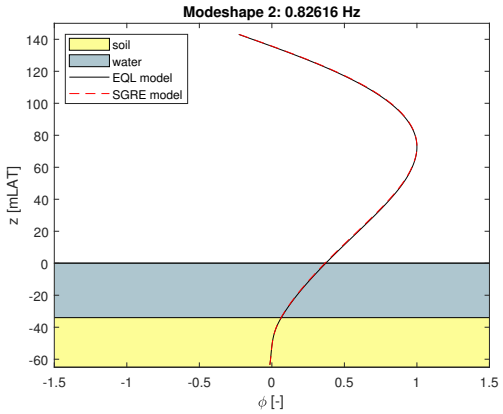

(c)

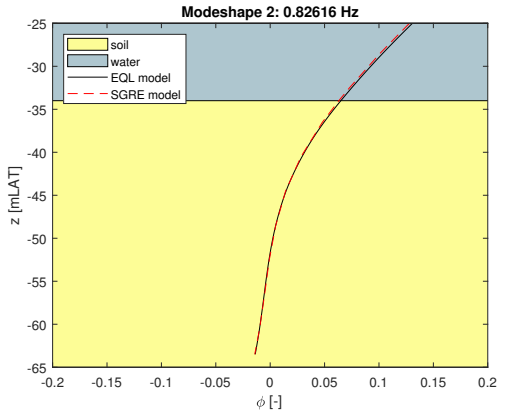

(d)

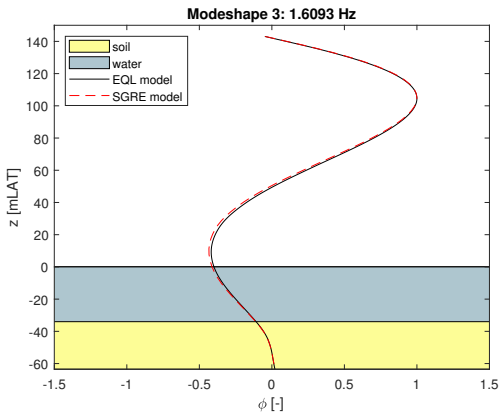

(e)

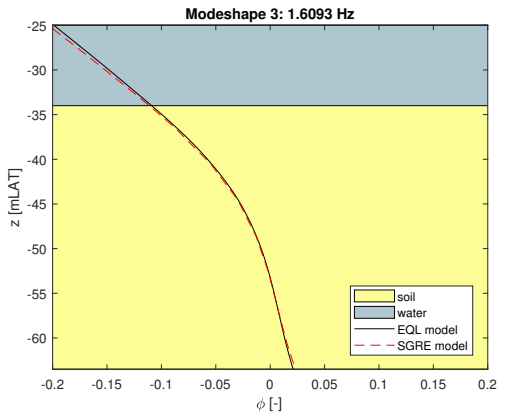

(f)

Figure 6.2: Comparing modeshapes SGRE structural model and tuned EQL model.

Section 7

Comparing Equivalent Linear analysis to other strategies for a full structural model

7.1 Key differences in analysis strategies

Four different analysis strategies are applied to find the response of a case study OWT under FLS loading.
Firstly, a **Linear** frequency-domain analysis is performed, where the stiffness of the soil around the monopile foundation is equal to the small strain stiffness. Damping originated from soil hysteresis is approximated through Rayleigh damping, exactly like the other sources of damping.

Two different types of Equivalent Linear analyses are also performed: **EQLa** and **EQLb**. The EQLa analysis defines the stiffness around the monopile foundation to be dependent on the reference deflection amplitude ($\mathbf{u}_{ref}$). Soil damping is continued to be modeled through Rayleigh damping. EQLb changes the way foundation damping is applied, by adding local hysteretic damping which is also dependent on $\mathbf{u}_{ref}$.

The final analysis performed is a nonlinear time-domain analysis using SGRE in-house software: **BHawC**. The foundation is modeled through p-y curves, while damping originating from the soil is considered through Rayleigh damping.

Table 7.1 shows the key differences between the 4 analyses performed. An important value to find is the added damping related to the soil around the monopile foundation. Only the baseline damping of the OWT is known, which is a combination of hydrodynamic, structural and soil damping. In order to not take the soil damping into account twice, the contribution of soil damping has to be removed in the EQLb case. We make an assumption in this thesis that soil damping is defined by identification of the soil damping for a loadcase with a $\mathbf{u}_{ref}$ of 2 mm at mudline. The identified soil damping ratio is **1.35 %** log. dec. (**0.21 %** critical).

	Linear	**EQLa**	**EQLb**	**BHawC**
Domain	Frequency	Frequency	Frequency	Time
Soil stiffness	Linear Elastic (small-strain)	Equiv. Linear ($\mathbf{u}_{ref}$)	Equiv. Linear ($\mathbf{u}_{ref}$)	Nonlinear Elastic (p-y curves)
Soil damping	Rayleigh (global)	Rayleigh (global)	Hysteretic (local, $\mathbf{u}_{ref}$)	Rayleigh (global)
Other damping	Rayleigh (global)	Rayleigh (global)	Rayleigh (global)	Rayleigh (global)

Table 7.1: Key differences between the analysis strategies.

7.2 Definition of the forcing on the system

The OWT is tested under a (high) FLS wave loading related to a wind speed of 25 m/s which hits the wind turbine head on (in the fore-aft direction). Because BHawC uses complex aerodynamic calculations in determining both wind loading and aerodynamic damping, both wind loading and aerodynamic damping are neglected. In order for this assumption to hold, the turbine is modeled in an idling state.

Six simulations are performed, related to 6 wave load time series. The time series are generated by SGRE in-house load calculation software. Although all 6 simulation results are included in Appendix (), the discussion in further sections focusses on Simulation 5 and Simulation 6. Simulation 5 is representative result for the first 5 analyses performed, while Simulation 6 is a clear outlier.

7.3 EQL analysis vs. Linear analysis

7.3.1 Foundation stiffness and local hysteretic damping

The results of Simulation 5 are shown in this section. As the difference in the frequency-domain strategies lies in the modeling of the soil, we naturally look at the properties of the foundation first. Figure 7.1 shows the stiffness and damping properties of the foundation with depth. For the Linear case, no reduction of stiffness and no addition of local hysteretic damping is observed (as this is a linear soil model). Both EQLa and EQLb show significant stiffness reduction over the foundation, especially close to mud-line. Key to note is the relatively large wave loading (associated with 25 m/s). Load cases with smaller loading result in less stiffness reduction. The presence of different soil layers can be observed from the blocks of similar stiffness reduction and damping results. We can also spot the presence of a pivot point around 18-19 m below mud-line. Only EQLb adds local hysteretic damping, as again it is the only constitutive model with that property.

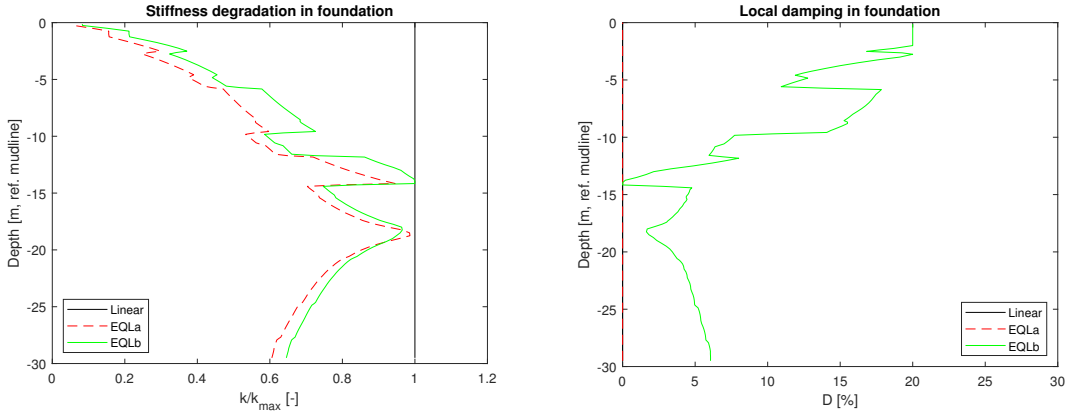

(a) (b)

Figure 7.1: Stiffness reduction and local hysteretic damping over the foundation.

A difference in the stiffness curves can be observed between EQLa and EQLb, even though both soil stiffnesses are modeled through an equivalent linear constitutive model. The added hysteretic damping in EQLb is greater than the Rayleigh damping added in EQLa. This produces smaller reference amplitudes $\mathbf{u}_{ref}$ in EQLb, which yields a higher foundation stiffness.

Specifically looking at Figure 7.1b, a large damping contribution of the soil layers from mud-line to 5-10 m depth can be observed for the EQLb care. The soil is weaker in these layers (due to lower confinement stress and other soil properties) and shows the largest deflections (due to the deflection shape of the foundation). Both of these effects cause larger soil hysteresis loops to be generated. The localized addition of soil damping is a more realistic way than adding global Rayleigh damping, as different parts of the foundation should provide different amounts of damping. One important note to make is that the cap of 20 % hysteretic damping is clearly visible in the top 2 m of soil. These weaker soil layers reach larger strains, which would apply unrealistically high hysteretic damping if the cap was not applied. The method for determining the right amount of hysteretic damping is dependent on the input damping curves. Although the Masing rules applied approximate stiffness of the soil quite well, the performance of Masing rules at higher strain amplitudes with respect to damping is worse. Further research into resembling the foundation response in other ways than with p-y curves and Masing rules is necessary.

7.3.2 EQLb: Global soil damping estimation

To estimate contribution of the soil damping in the first mode for the EQLb method, a method of logarithmic decay is used. To directly estimate damping from the wave load simulations is relatively difficult. Therefore, a pulse load is applied to the foundation found through applying wave load simulations. The decay of the system is evaluated afterwards. The deflection of the RNA over time is shown in Figure 7.2a. A logarithmic fit is applied to the peaks of this decaying function, as shown in Figure 7.2b.

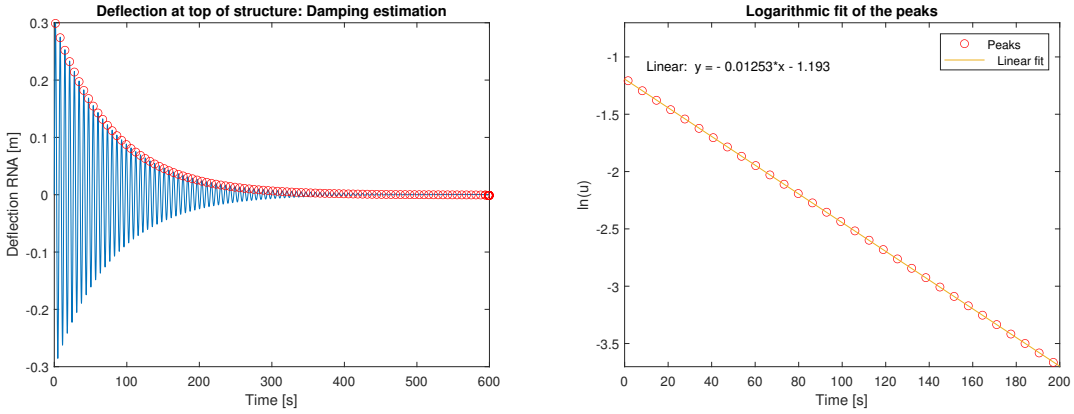

(a) (b)

Figure 7.2: Estimation of damping in the 1st mode through logarithmic decay.

We can compare this logarithmic fit to the general solution for a 1DOF damped free vibration:

$$u(t) = Ae^{-\zeta\omega_0 t}cos(\omega_1 t - \varphi) \tag{7.1}$$

From the slope of the logarithmic fit the damping ratio of the 1st mode can be deduced. This method of identification has been validated with a damping identification of the Linear model. As soil damping is not the only damping source, other sources like hydrodynamic and structural damping are subsracted from the identified damping ratio. The EQLb method produces a foundation damping ratio in the 1st mode between **0.64-0.80 %** critical (**4-5 %** log. dec.). This value is a range due to the 6 different simulations. In simulations where the foundation shows higher reference deflection amplitudes $\mathbf{u}_{ref}$, the identified soil damping is higher.

These foundation damping ratios are compared to other research, similar damping ratios are found. Numerical analyses in the time domain (using rotor stop tests) for similar conditions show 1.0-1.5 % critical soil damping in the 1st mode [Dilas, 2018], while modal analysis of experimental rotor stop tests shows up to 1.5 % critical soil damping in the 1st mode [Versteijlen et al., 2011]. A frequency-domain analysis where a degraded soil stiffness and local damping are applied showed 0.5-0.7 % critical soil damping in the 1st mode [Chen and Duffour, 2018]. We have to keep in mind however that more research is necessary into the hysteretic damping curves in dynamic loading before local response amplitude-dependent hysteretic damping can be reliably applied through the EQL method.

7.3.3 Foundation deflections

The solution strategies in the frequency domain, Linear, EQLa and EQLb, are now evaluated on the basis of deflections in the foundation. Figure 7.3 shows the cumulative distributions of the deflections at mud-line in the time domain. For the Linear results for example, 50 % of the time deflections are at or below 2.5 mm. The maximum observed deflection at mud-line is about 9 mm. For EQLa and EQLb, a circle indicates the reference deflection used to determine the equivalent linear foundation stiffness at mud-line. This circle is placed by taking 65 % of the observed maximum deflection.

In general, EQLa and EQLb both show larger deflections than the Linear method. A decreased stiffness of the foundation means the foundation will indeed deflect more. We do see that EQLb shows smaller deflections than EQLa. The added hysteretic damping causes smaller deflections in the foundation.

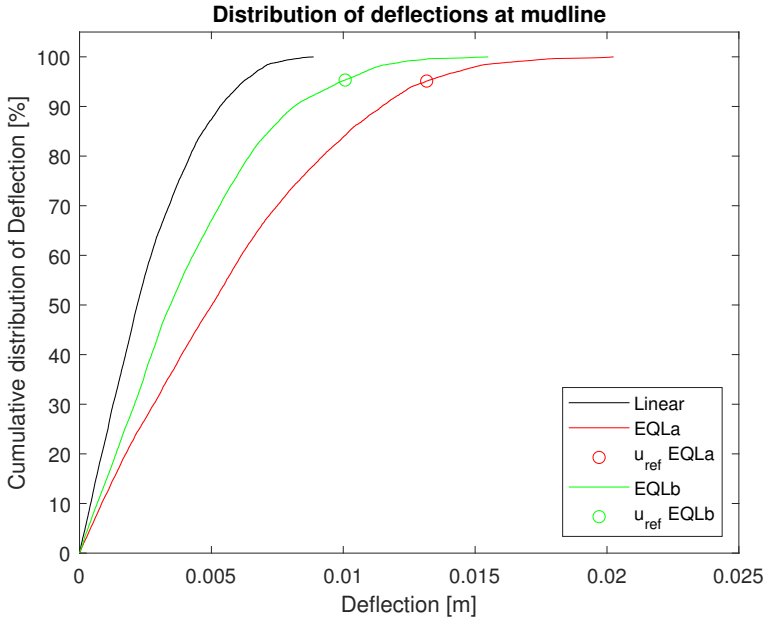

Figure 7.3: Cumulative distribution of deflections at mudline.

We take a closer look at deflection spectra in the foundation in Figure 7.4. The left figures show the spectra at mud-line, 10m into the foundation and at pile tip (30m into the foundation). The right figures show a zoom in around the first mode of the structure. The first natural frequency of the structure is 0.156 Hz. The peak of the Linear results is indeed situated at 0.156 Hz, but this is not the case for EQLa and EQLb. A degradation of the foundation stiffness causes a shift of resonance frequency to about 0.152 Hz. The amplitudes of both EQLa and EQLb are also significantly higher than Linear, caused by both the shift in resonance frequency (causing the resonance frequency of the structure to be closer to the frequency content of the wave loading) and a decreased foundation stiffness.

Again, the lower amplitude of the EQLb spectra can be attributed to added damping in the 1st mode.

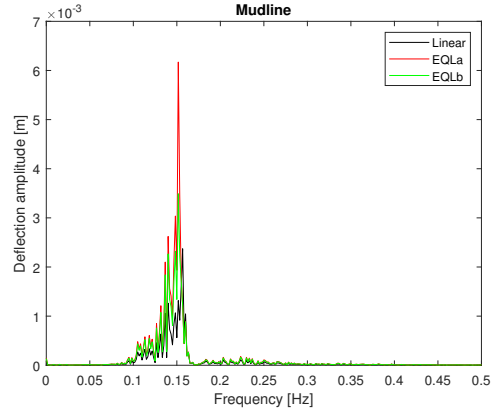

(a) 0-0.5 Hz

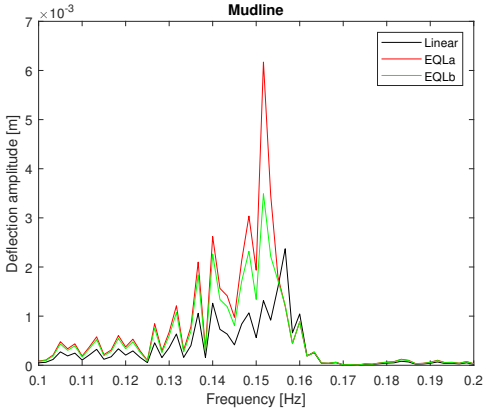

(b) 0.1-0.2 Hz

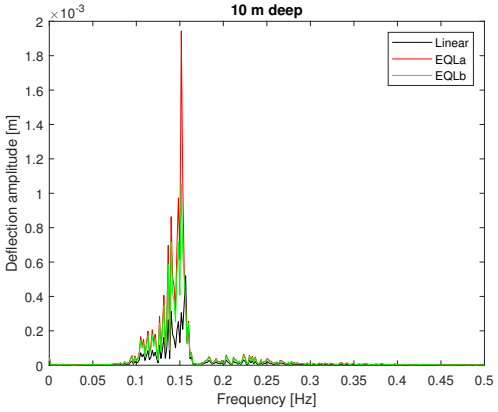

(c) 0-0.5 Hz

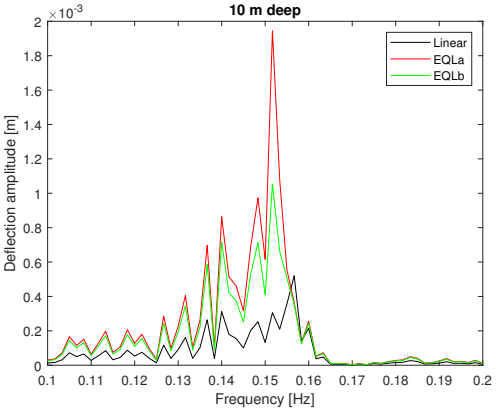

(d) 0.1-0.2 Hz

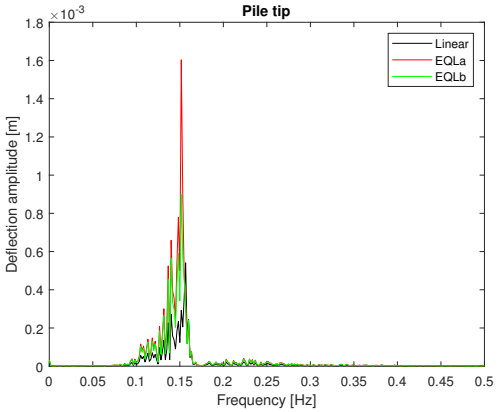

(e) 0-0.5 Hz

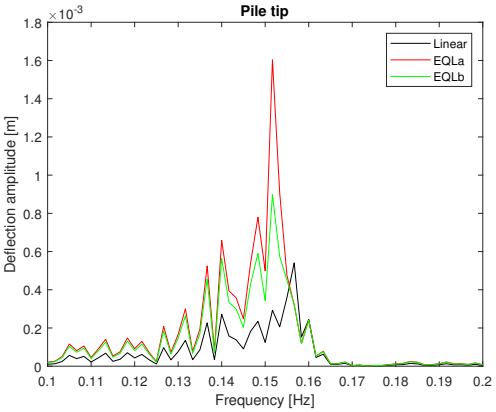

(f) 0.1-0.2 Hz

Figure 7.4: Comparing deflection spectra in foundation. Linear v EQLa v EQLb.

7.4 Comparing the frequency-domain strategies to nonlinear time-integration

Two simulations are shown in this section: Simulation 5 and Simulation 6. Simulation 5 shows a representative results for Simulations 1-5, while Simulation 6 is an outlier. The main comparison is made between EQLa and BHawC. As soil damping is modeled in the same way (through Rayleigh damping), the only difference between these 2 strategies lies in the soil stiffness.

7.4.1 Simulation 5

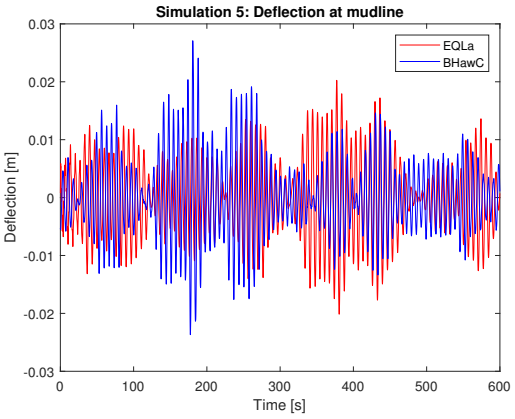

Figure 7.5: Deflection at mudline: Simulation 5.

Both Figure 7.5 (the deflection at mud-line over time) and Figure 7.6 (the cumulative distribution of deflections at mud-line over time) show that the EQLa method and BHawC find similar results for Simulation 5. Apart from an outlier around 200s, the deflections at mud-line show similar amplitudes. The reference deflection $\mathbf{u}_{ref}$ used in the EQLa analysis of about 14 mm at mud-line is representative of the deflections found in BHawC.

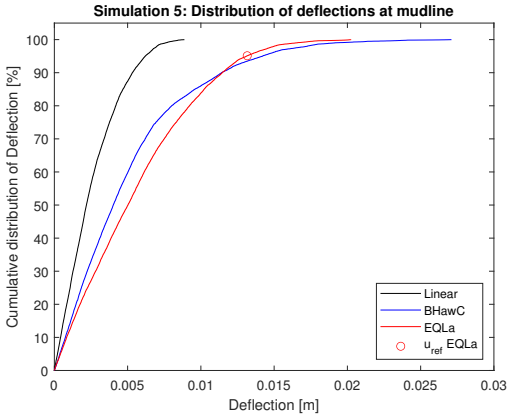

Figure 7.6: Cumulative distribution of deflections at mud-line. Simulation 5.

Figure 7.7 shows a comparison of the deflection spectra at 3 points in the foundation: at mud-line, 10 m below mud-line and at the pile tip. The left figures again show the spectrum from 0-0.5 Hz, while the right figures show a zoomed in version around the 1st mode.

Looking at the peaks around the 1st resonance frequency, close similarities are observed between BHawC and EQLa. The amplitudes of the spectra are similar and the peak is situated at the same frequency (about 2 % lower than the linear resonance frequency). The EQL model shows a significantly closer resemblance to BHawC than the Linear model.

Looking at the frequency ranges from 0-0.5 Hz a small peak is observed around 0.42-46 Hz. Two explanations arise for this peak. A blade mode is present at that frequency, which is modeled by BHawC but not by the structural model used by the EQLa method. Next to that, peaks are observed at exactly 2 and 3 times the main resonance peak. Because BHawC uses a nonlinear elastic soil model, generation of higher harmonics could also cause these extra peaks. The EQLa method assumes no higher harmonics are generated.

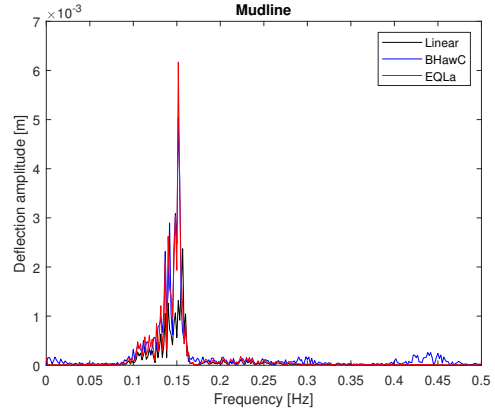

(a) 0-0.5 Hz

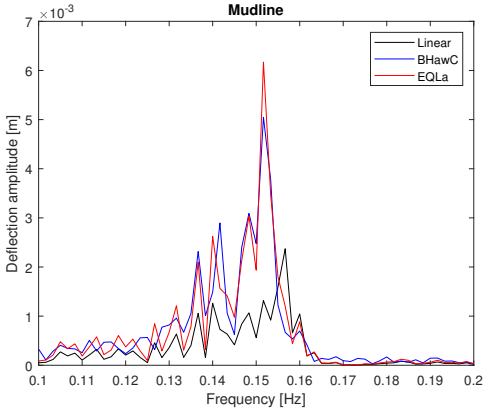

(b) 0.1-0.2 Hz

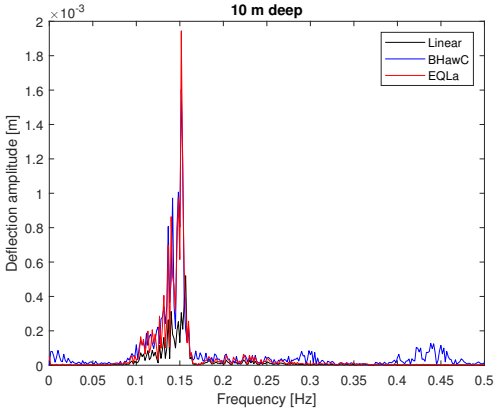

(c) 0-0.5 Hz

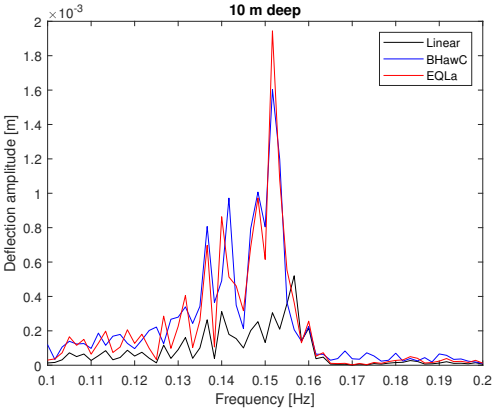

(d) 0.1-0.2 Hz

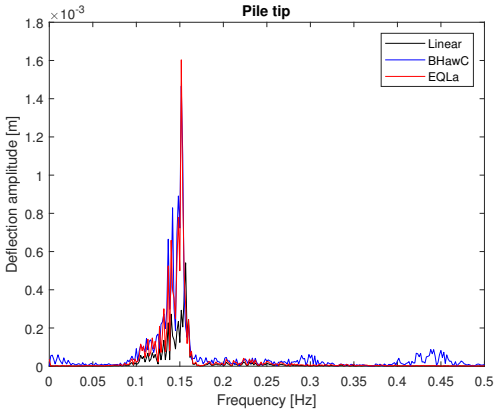

(e) 0-0.5 Hz

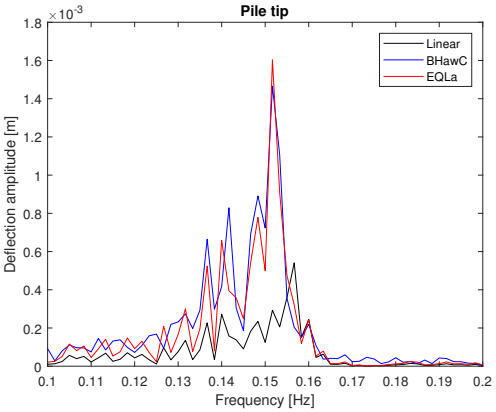

(f) 0.1-0.2 Hz

Figure 7.7: Comparing deflection spectra in foundation. Simulation 5.

7.4.2 Simulation 6

However, not all simulations showed such positive results. Figure 7.8 shows the deflections at mudline for Simulation 6.

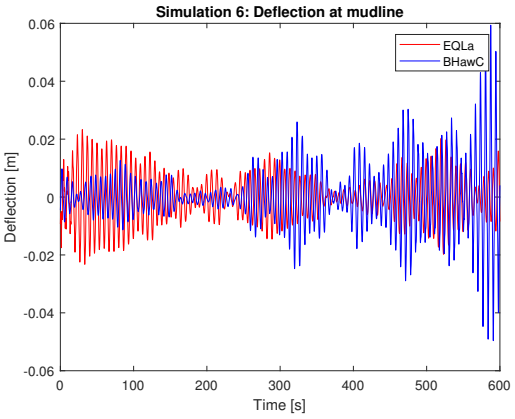

Figure 7.8: Deflection at mudline: Simulation 6.

With the EQL method, a single reference deflection amplitude $\mathbf{u}_{ref}$ is used to approximate the response over the full time domain. Figure 7.8 however shows different types of response. From 0-250s, smaller deflections (to about 10 mm) are observed. Nonlinearity in the soil is limited. The time span from 250-550s however shows larger deflections (20-30 mm) and therefore more nonlinearity. From 550-600s extreme deflections up to 60 mm are even observed. It is impossible to take one $\mathbf{u}_{ref}$ to describe the foundation behavior over the full time domain.

When looking at the cumulative distribution of deflections at mud-line, Figure 7.9, we see that the EQLa results indeed do not resemble the BHawC results. The observed maximum deflection is significantly higher for BHawC and the top 10% of deflections for BHawC are between 20 mm and 60 mm, compared to 15-25mm for EQLa. However, even though the fit between EQLa and BHawC is not good, the Linear deflections are significantly lower.

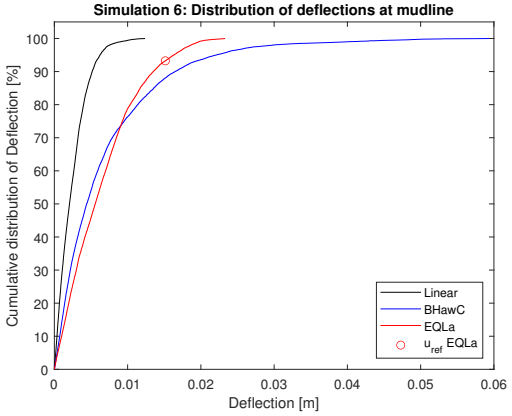

Figure 7.9: Cumulative distribution of the deflections at mudline: Simulation 6.

When comparing spectra at mud-line, which is shown in Figure 7.10, the same conclusions are found. Similar to Figure 7.7, spectra from BHawC show an extra peak around 0.42-0.46 Hz. This peak is more pronounced for this specific load file. This peak can again be attributed to both the presence of a blade mode and the generation of higher harmonics. The significant increase in relative size of this peak with respect to Figure 7.7 can not be explained by just the presence of a blade mode. The larger contribution of higher harmonics due to the larger degree of nonlinearity in the foundation would fit this observation better.

Figure 7.10b shows that the EQLa method does not resemble the BHawC response that well around the 1st structural mode. However, the EQLa method still shows a better resemblance to the nonlinear time domain method than the Linear method.

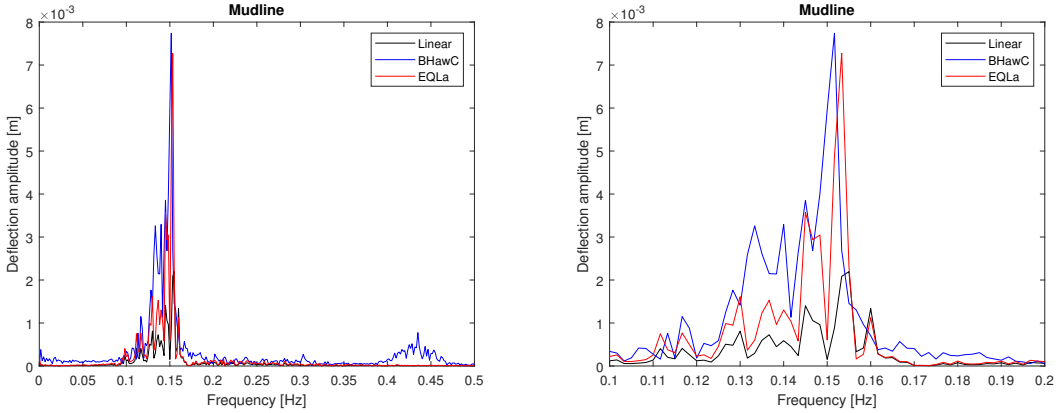

(a) 0-0.5 Hz

(b) 0.1-0.2 Hz

Figure 7.10: Deflection spectra at mudline: Simulation 6.

7.4.3 Performance of an EQL solution strategy

An EQL analysis of an OWT subjected to multiharmonic loading hinges on 2 important assumptions:

- The influence of higher on the response is limited (allowing for the separate calculation of each frequency component each EQL iteration).
- A single reference deflection amplitudes $\mathbf{u}_{ref}$ can represent the foundation behavior over the full time window.

With respect to the first assumption, the analyses of OWTs show that higher harmonics do not play a critical role in the response of the full system at the investigated load level.

The second assumption brings a bigger limitation to the effectivity of EQL analysis. One of the 6 simulations that was analyzed showed significantly larger deflections (and therefore nonlinearity) for a short part of the time window. An EQL method can not reproduce large differences in foundation behavior over time, putting a limit on the load level of the analysis. A relatively simple metric was used to identify a reference response amplitude (65 % of the maximum in the time domain). A different method of finding a reference response amplitude could extend the applicability of an EQL analysis, like a measure defined by the distribution of deflections instead of just the observed maximum. However, the EQL method would still require one reference response amplitude. If the foundation behavior can not be defined by one value, no technique of defining a reference response amplitude can solve that issue.

We have to stress however the performance of the EQL strategy with respect to a the Linear strategy. For the load level applied in these analyses, an EQL analysis yields closer results to a nonlinear time-history analysis than a Linear analysis.

Further research is necessary to obtain the limit of applicability of an EQL method, focused on more runs at the applied load level related to a wind speed of 25 m/s and more runs at lower wind speeds. Our expectation is however that, because the applied load case is on the high side of FLS (long-term average wind speeds in the North Sea are around 10 m/s), EQL methods are suitable for most FLS load cases. Especially in concept design, where quick results are sometimes needed, an EQL method would provide a better estimation of nonlinear time-history analyses than a Linear method would.

7.5 Using an Equivalent Linear solution strategy in fatigue damage calculations

As the main goal of OWT simulations is to calculate the fatigue life time of the structure, this section explains how an Equivalent Linear solution strategy could fit into that procedure. As explained in Section 1.5, fatigue damage calculations can be done in both the time domain and the frequency domain.

An EQL solution strategy requires a time-history of the forcing applied to the system, which means the most direct connection to a fatigue damage calculation would be through a rainflow counting algorithm. As S-N curves for OWTs are often set up on a cross-sectional level, shear forces and moments have to be added as output from the simulations. An EQL method can then be used instead of a computationally less efficient nonlinear time domain method.

The combination with the Dirlik method, a fatigue damage calculation taking a probabilistic approach in the frequency domain, is more difficult to combine with an EQL method. Because the input of the Dirlik method uses load spectra, no time-history information about the load is used. The underlying assumption of the Dirlik method is also a linear system. However, an EQL method can be used to find an appropriate linearization of the foundation response to be used in the Dirlik method. By using several EQL simulations, a representative linearization for a specific load level can be found. For each load case analyzed however, a different linearization is needed.

Figure 7.11 shows the comparison of deflection spectra at mud-line for BHawC and the EQLb method. Two factors play a role in the global dynamic response of the OWT: the place of the resonance peak and the global damping ratio.

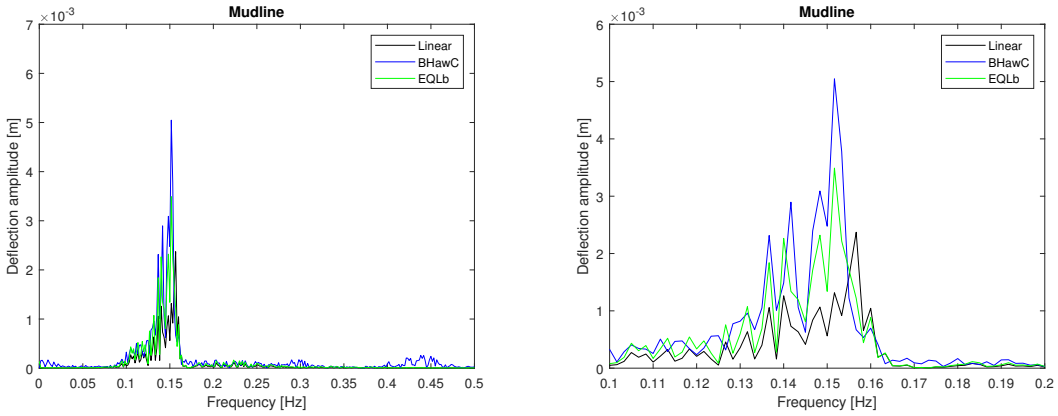

(a) 0-0.5 Hz

(b) 0.1-0.2 Hz

Figure 7.11: Deflection spectra at mudline, comparing BhawC and EQLb: Simulation 5.

The results of the EQL method show a similar main frequency of the first resonance peak as the results of BHawC (which is about 2 % lower than the first natural frequency of the system). Because the resonance peak is shifted to lower frequencies and both wind and wave spectra are generally situated at lower frequencies (see Figure 1.1), a higher fatigue damage is predicted. [Schafhirt et al., 2016] did an investigation into the effects of a lower foundation stiffness on the fatigue damage calculation of an OWT. A lower foundation stiffness that causes a shift of the resonance peak of 2 % increases the fatigue damage at mud-line by about 5 %. Important to take

into account however, is that an EQL method changes the foundation properties per load case. This means that for lower loads, this shift in the resonance peak of the first mode (and therefore the increase in fatigue damage) is less pronounced.

The other contributing factor is the global damping ratio. An EQL formulation where local response-amplitude dependent hysteretic damping is applied (EQLb) shows larger global soil damping ratios than BHawC. The increase in foundation damping is 0.4 - 0.6 % critical. The direct influence of this higher global soil damping can be seen in Figure 7.11 as well. The deflections at mud-line are lower for the EQLb case than for BHawC. Although a calculation of the moments and shear forces at mud-line is necessary, the expectation is that EQL simulations finds lower fatigue damage at mud-line than BHawC simulations. This hypothesis is strengthened by [Aasen et al., 2017], where the addition of 0.3 % critical damping reduced total fatigue damage at mud-line by 13 %.

In [Aasen et al., 2017], the inclusion of a nonlinear hysteretic foundation model (through a macro-element instead of through a distrubuted foundation stiffness like in this thesis) is evaluated under varying load conditions related to wind speeds from 2 - 30 m/s. This analysis showed a decrease in total fatigue damage at mud-line of 11 % with respect to a p-y formulation. In line with this research, we expect that an EQL analysis would also show a lower total fatigue damage. Using a calibrated linear foundation with the right amount of damping would also result in similar results, but would need a recalibration for each load level. The big advantage of a response-amplitude dependent formulation of the foundation, as stated by [Aasen et al., 2017], is that the need for recalibration of the foundation for different load cases is reduced.

Section 8

Conclusions and Recommendations

8.1 Project overview

The main research question of this project is: *How to combine a nonlinear hysteretic constitutive soil model with a frequency-domain analysis to improve simulations of Offshore Wind Turbines on a monopile foundation under Fatigue Limit State conditions?* In order to answer this question, 7 goals are defined.

- To **compare** different solution strategies in the frequency domain based on their ability to represent hysteretic behavior.
- To **evaluate** the solution strategies on their ability to be used in a full FE model under multiharmonic excitation.
- To **fit** hysteretic constitutive models to available soil reaction data.
- To **set up** an FE formulation that includes the suggested solution strategy and constitutive model.
- To **verify** the FE formulation with an available structural model of an OWT on a monopile foundation.
- To **quantify** the change in foundation response (in stiffness, damping and deflection shape) between a conventional frequency-domain analysis and the suggested solution strategy.
- To **compare** the suggested frequency-domain solution strategy to a time-domain strategy which uses a p-y formulation for the monopile foundation. The focus lies on the behavior of the monopile foundation.

In this Section, conclusions are drawn with respect to the main research question first. Afterwards, conclusions found considering the choice of solution strategy are elaborated on. We then state conclusions made regarding the modeling decisions related to the soil. Lastly, recommendations are given for future research.

8.2 Conclusions to the main research question

The main conclusions we find to answer the main research question are the following:

- An Equivalent Linear solution strategy in combination with a nonlinear hysteretic soil model improves frequency-domain analyses of OWTs under FLS conditions by capturing the dependency of the foundation on the response amplitude. That way, frequency-domain analyses can approximate nonlinear time-integration methods up to higher load levels.
- Results found through an EQL method closely resemble nonlinear time-integration results. Both the deflection spectra in the foundation and the distribution of deflections in the foundation are very similar. This only holds provided the variability of the response of the foundation over the time window is not very large and the influence of generated higher harmonics is limited (to be at least an order of magnitude smaller than the 1st harmonic).
- The possibility of adding local hysteretic response amplitude-dependent damping through an EQL method allows for a more realistic incorporation of the soil damping. In the case study, soil damping ratios found in the 1st structural mode (of 0.64-0.80 % critical / 4-5% log. dec.) are close to numerical and experimental case studies with similar OWT design and loading. The accuracy of the applied damping is however directly linked to the quality of the Equivalent Linear hysteretic damping curves.

8.3 Conclusions related to the solution strategy

Several conclusions were found related to analyzing the different solution strategies for incorporating a hysteretic constitutive model into a frequency-domain method:

- In 1DOF, the Alternating Frequency-Time Harmonic Balance Method (AFTHBM) can be used to solve the response of a nonlinear hysteretic constitutive soil model. The response amplitude-dependency of the behavior of the element is captured. At higher load levels, higher harmonics are generated. These higher harmonics also cause superharmonic resonance when the element is connected to a mass and a viscous damper. The generated hysteresis loops match nonlinear time integration results, as long as enough higher harmonics are taken into account.

- However, using AFTHBM to solve the response of a full OWT FE model under multiharmonic loading is computationally challenging. Complexity of the algorithm with respect to both degrees of freedom and analysis frequencies is $O(n^3)$, because of a necessary inversion of a fully populated Jacobian in the method.

- When we neglect the generation of higher harmonics and solely focus on the response amplitude-dependency of the hysteretic element, the solution strategy can be simplified into an Equivalent Linear Analysis. The system is solved iteratively by alternating between calculating the response and updating the stiffness and hysteretic damping of the element. These simplifications allow for the analysis frequencies to be solved separately in each iteration, significantly speeding up calculations. In the comparison between EQL and AFTHBM when applied to a Bouc-Wen element, similar results are found under harmonic loading, as long as the higher harmonics of the response are at least an order of magnitude smaller than the response in the 1st harmonic.

- The complexity of the EQL strategy with respect to degrees of freedom becomes $O(n^2)$ due to the use of sparse matrices. The complexity with respect to analysis frequencies even goes down to $O(nlog(n))$ because the calculations can be split up per analysis frequency. The analysis of FE models with of a full OWT under multiharmonic loading is computationally possible, which is why the EQL strategy is implemented in the rest of the thesis.

- To define an $\mathbf{u}_{ref}$ when a multiharmonic load is applied to the system, the metric of 65% of the maximum observed response in the time domain is chosen. An EQL analysis in combination with this metric, commonly used in earthquake engineering, is shown to get a response spectrum that fits with a nonlinear time integration result.

- An EQL strategy is able to be combined with a fatigue damage calculation. A time-domain calculation can directly be performed through a rainflow counting algorithm. Otherwise, the EQL strategy can provide the appropriate linearization to be used in the Dirlik method, for a specified load level.

- For the investigated case study, the EQLb analysis (with both response-amplitude dependent soil stiffness and hysteretic damping) is shown to create a 2% decrease of the 1st resonance peak (which is also observed in a nonlinear time-history analysis). A 0.4-0.6% increase of critical damping in the 1st structural mode is found when compared to the global damping applied in the nonlinear time-history analysis. Based on these results in combination with [Aasen et al., 2017], our expectation is that calculated fatigue damage through an EQLb analysis is lower than through an analysis which uses p-y curves.

8.4 Conclusions related to the soil modeling

In the setup of a representative FE model of the foundation, we have fit our constitutive soil model to available data. The following conclusions were drawn:

- A Bouc-Wen model of hysteresis is fitted to a set of p-y curves (which are based on a monotonic 3D FE analysis and subsequently reduced by a factor to take cyclic loading into account). In monotonic loading, the original Bouc-Wen model can indeed be fitted to these p-y curves. In cyclic loading however, hysteresis loops are generated with too high hysteretic damping ratios at medium to large strains. The hysteretic damping ratio reaches levels of up to 70% at medium strains, while literature ([Beuckelaers, 2017] and [Yniesta and Brandenberg, 2015]) suggests hysteretic damping ratios at medium strains of 5-15%. Maximum hysteretic damping ratios at large strains are observed up to 20%. The original Bouc-Wen model of hysteresis is therefore not suitable for the use in foundation modeling where medium to large strains are reached.

- A Masing model is also fitted to a set of p-y curves. Stiffness properties (in both monotonic and cyclic loading) match perfectly to the used backbone p-y curve. Hysteretic damping ratios at medium strains of the hysteresis loops generated through the Masing model are between 5 and 15%, which fits relevant literature. However, at large strains the hysteresis loops show hysteretic damping ratios of up to 50%. This large hysteretic damping ratio of the Masing element is also described in other literature [Yniesta and Brandenberg, 2015]. In order to not apply too much damping at large strains, a cap of 20% is applied to the hysteretic damping ratio of the EQL Masing element.

- From testing a nonlinear hysteretic constitutive soil model in dynamic conditions under harmonic loading as well as multiharmonic loading, an EQL approximation is shown to find accurate results as long as nonlinearities are limited. The most important influencing factors are the response amplitude-dependent secant stiffness and hysteretic damping of the generated hysteresis loops.

- In the EQLb procedure, the applied damping is hysteretic (rate-independent), which models the material damping of the soil. The implemented EQL procedure in the frequency domain can model this type of damping efficiently through applying a complex-valued soil stiffness. Time-domain methods do not have the possibility to apply a complex-valued soil stiffness and have to resort to equivalent viscous damping if local damping is applied in the foundation. Viscous damping is dependent on frequency however, which has the downside of providing too much damping for higher frequencies. This effect causes overdamping of higher modes. Although in the load case of this thesis no higher modes are activated, the benefit of representing soil material damping through hysteretic damping instead of equivalent viscous damping is present for other load cases like earthquake loading.

8.5 Recommendations

Our recommendations for future research are as follows:

- The comparison between EQL and nonlinear time-history results has been performed for one load case, with only 6 load simulations. To investigate the upper limit of applicability of an EQL method, this analysis has to be repeated for many different load cases, and for many more load simulations. In that way, one can statistically express the effectiveness of the EQL method. An EQL strategy can only be used when large permanent deformations do not occur. Therefore, the response to ULS load cases can not be accurately modeled through an EQL method.

- Fatigue damage calculations were not performed in this thesis. In Section 7.5, a prediction is made on what the effect of an EQL solution strategy combined with a nonlinear hysteretic soil model will be on the fatigue damage. This prediction is based on the change in resonance peaks and critical damping ratios, in combination with literature. Nevertheless, it is recommended to perform fatigue damage calculations to check that prediction.

- The focus on this thesis was on the modeling of the monopile foundation. Deflection spectra in the foundation and the stiffness and damping properties of the foundation itself were compared. However, the modeling of the monopile itself also has an effect on the response of the rest of the structure. It is recommended to also compare the response (and the fatigue damage) at locations in the structure other than in the foundation.

- The AFTHBM procedure shown in Section 2 is a force-controlled method. The behavior of the Bouc-Wen element can be modeled in dynamic conditions, but only to a certain response amplitude. Afterwards, the element yields. To find the behavior at higher response amplitudes, it is suggested to use an amplitude-controlled method (like in [Wong et al., 1994a] and [Wong et al., 1994b]). For an accurate representation of the frequency response function at larger load levels, a combination of a force-controlled and an amplitude-controlled method is needed.

- As discussed in Section 4.4, the original Bouc-Wen model of hysteresis reaches hysteretic damping ratios at medium strains as high as 70%. [Gerolymos and George, 2005] shows a method of changing the Bouc-Wen model to control the hysteretic damping properties. By uniformly scaling the Bouc-Wen parameters κ, β and γ (Named A, g and b respectively) as a function of response amplitude, the relative size of the hysteresis loop is controlled. The combination of this altered Bouc-Wen model with an AFTHBM procedure is straightforward, as only Equations 2.27, A.6, A.7 and A.8 require a small change when compared to the implementation of the original Bouc-Wen model.

- When multiharmonic loading (like wind and wave loading) is applied, the EQL method needs a representative response amplitude $\mathbf{u}_{ref}$ for calculating the equivalent linear foundation response. While in this project a relatively simple metric was used (65 % of the observed maximum deflections), a more sophisticated metric could extend the robustness of the EQL method. It is suggested to look into a metric which uses the distribution of deflections in the time domain.

- The EQL method requires the input of stiffness degradation and hysteretic damping curves. While these curves are frequently used as a function of strain in the soil, the 1D foundation model with a distributed soil stiffness requires curves as a function of deflection in the foundation. [Zhang et al., 2021] suggests a method for finding these curves by directly looking at 3D FE. The specific method used is only applicable to slender piles however. With a method like in [Zhang et al., 2021], fitted p-y curves are not required as intermediate results anymore.

- The identification of soil properties (to be used in the setup of the 3D FE model of the soil medium) is commonly based on static tests like a CPT test or a triaxial test. To take into account cyclic and dynamic loading, reduction factors are used and a nonlinear hysteretic model like the Masing model is implemented (like in this thesis). However, in the case of analyzing an OWT foundation, the soil is loaded under dynamic conditions. It is recommended that the dynamic soil properties are identified through a dynamic soil test. For example, a resonant column test [Cavallari, 2016] or a dynamic torsional shear test [Gabryś et al., 2016] could be used.

- The formulation of most nonlinear hysteretic constitutive soil models is focused on capturing the shape of the hysteresis loops as best as possible. However, as discussed in Section 1.3, linearized stiffness and damping properties are sufficient to model the dynamic response of a large structure with limited nonlinearities. Section 3 shows that at local element level response-amplitude dependent stiffness reduction and hysteretic damping curves are sufficient as well (when the nonlinearity in the system is limited). It is therefore recommended that future research looks into identifying these stiffness reduction and hysteretic damping curves as accurately as possible. For dynamic analysis of large structures with limited nonlinearities, accuracy of the linearized properties contributes more to realistic modeling of the full structure than the accuracy of the specific shape of the hysteresis loops.

- The foundation model that is applied in this thesis is rate-independent. Rate-dependent effects are also present in the soil response. These effects are generally neglected for the analysis of OWTs subjected to wind and wave loading because of the frequency of wind and wave loading typically being below 1 Hz ([Malekjafarian et al., 2021]). However, for other load cases like earthquake loading these effects can play a significant role. Resonance of the soil medium and radiation damping are examples of these frequency-dependent effects. ([Hasper, 2021]) looks into including these effects in a 1D approach, with the assumption of a linear constitutive soil model. More research is needed into how these effects could be added to an EQL formulation.

Bibliography

[Aasen et al., 2017] Aasen, S., Page, A. M., Skau, K. S., and Nygaard, T. A. (2017). Effect of foundation modelling on the fatigue lifetime of a monopile-based offshore wind turbine. *Wind Energy Science*, 2(2):361–376.

[Abadie, 2015] Abadie, C. N. (2015). *Cyclic Lateral Loading of Monopile Foundations in Cohesionless Soils*. PhD thesis, University of Oxford.

[Bayton and Black, 2016] Bayton, S. M. and Black, J. A. (2016). Evaluating the p – y curve method of analysis for large-diameter monopiles using centrifuge modelling. In *Geo-Chicago 2016*. American Society of Civil Engineers.

[Beuckelaers, 2017] Beuckelaers, W. (2017). *Numerical modelling of laterally loaded piles for offshore wind turbines*. PhD thesis, University of Oxford.

[Bratosin and Sireteanu, 2002] Bratosin, D. and Sireteanu, T. (2002). Hysteretic damping modelling by nonlinear kelving-voigt model. *Proceedings of the Romanian Academy*, 3(3).

[Byrne et al., 2017] Byrne, B., Mcadam, R., Burd, H., Houlsby, G., Martin, C., Beuckelaers, W., Zdravkovic, L., Taborda, D. M. G., Potts, D., Jardine, R., Ushev, E., Liu, T., Abadias, D., Gavin, K., Igoe, D., Doherty, P., Gretlund, J., Pacheco Andrade, M., Wood, A., and Plummer, M. (2017). Pisa: New design methods for offshore wind turbine monopiles. In *8th International Conference for Offshore Site Investigation and Geotechnics*.

[Cavallari, 2016] Cavallari, A. (2016). Resonant column testing challenges. In *1st IMEKO TC-4 International Workshop on Metrology for Geotechnics*.

[Charalampakis, 2010] Charalampakis, A. E. (2010). Parameters of bouc-wen hysteretic model revisited. *International Congress on Mechanics*, 9.

[Chen and Duffour, 2018] Chen, C. and Duffour, P. (2018). Modelling damping sources in monopile-supported offshore wind turbines. *Wind Energy*, 21(11):1121–1140.

[Chiang, 1999] Chiang, D.-Y. (1999). The generalized masing models for deteriorating hysteresis and plasticity. *Applied Mathematical Modelling*, 23:847–863.

[Corciulo et al., 2017a] Corciulo, S., Zanoli, O., and Pisanò, F. (2017a). Supporting the engineering analysis of offshore wind turbines through advanced soil-structure 3d modelling. In *Volume 9: Offshore Geotechnics: Torgeir Moan Honoring Symposium*. American Society of Mechanical Engineers.

[Corciulo et al., 2017b] Corciulo, S., Zanoli, O., and Pisano, F. (2017b). Transient response of offshore wind turbines on monopiles in sandrole of cyclic hydro-mechanical soil behaviour. *Computers and Geotechnics*, 83:221–228.

[Dilas, 2018] Dilas, L. (2018). Estimation of soil damping contribution on offshore monopiles using plaxis 3d approach. Master's thesis, TU Delft University of Technology.

[DNV, 2019] DNV (2019). *DNVGL-RP-C212*. DNV GL.

[Dornhelm et al., 2019] Dornhelm, E., Seyr, H., and Muskulus, M. (2019). Vindby—a serious offshore wind farm design game. *Energies*, 12(8):1499.

[Gabryś et al., 2016] Gabryś, K., Sas, W., Soból, E., and Głuchowski, A. (2016). Torsional shear device for testing the dynamic properties of recycled material. *Studia Geotechnica et Mechanica*, 38(4):15–24.

[Gerolymos and George, 2005] Gerolymos, N. and George, G. (2005). Constitutive model for 1-d cyclic soil behaviour applied to seismic analysis of layered deposits. *Japanese Geotechnical Society: Soils and Foundations*, 45(3):147–159.

[Guilherme and Correia, 2016] Guilherme, A. and Correia, J. A. (2016). A user-friendly tool for fatigue assessment of steel structures according to eurocode 3. In *5th International Conference: Integrity - Reliability - Failure*.

[Hasper, 2021] Hasper, Y. (2021). An efficient 1d time-domain model accounting for the 3d frequency-dependent dynamic soil stiffness. Master's thesis, TU Delft.

[Hoogstraten, 2019] Hoogstraten, S. (2019). The macro-element method for integrated analyses of offshore wind turbines. mathesis, TU Delft.

[Kallehave et al., 2015] Kallehave, D., Byrne, B. W., Thilsted, C. L., and Mikkelsen, K. K. (2015). Optimization of monopiles for offshore wind turbines. *Philosophical Transactions of the Royal Society A: Mathematical, Physical and Engineering Sciences*, 373(2035):20140100.

[Krack and Gross, 2019] Krack, M. and Gross, J. (2019). *Harmonic balance for nonlinear vibration problems*. Springer-Verlag GmbH.

[Krathe and Kaynia, 2016] Krathe, V. L. and Kaynia, A. M. (2016). Implementation of a non-linear foundation model for soil-structure interaction analysis of offshore wind turbines in FAST. *Wind Energy*, 20(4):695–712.

[Lacarbonara and Vestroni, 2003] Lacarbonara, W. and Vestroni, F. (2003). Nonclassical responses of oscillators with hysteresis. *Nonlinear Dynamics*, 32:235–258.

[Madhukar et al., 2018] Madhukar, S., Reddy, B. R. H., Kumar, G. A., and Naik, R. P. (2018). A study on improvement of fatigue life of materials by surface coatings. *International Journal of Current Engineering and Technology*, 8(01).

[Malekjafarian et al., 2021] Malekjafarian, A., Jalilvand, S., Doherty, P., and Igoe, D. (2021). Foundation damping for monopile supported offshore wind turbines: A review. *Marine Structures*, 77:102937.

[Massopust, 2002] Massopust, P. R. (2002). A short note on hysteresis and odd harmonics.

[Matsuishi and Endo, 1968] Matsuishi, M. and Endo, T. (1968). Fatigue of metals subjected to varying stress. *Japan Society of Mechanical Engineering*.

[Pruiksma, 2016] Pruiksma, J. (2016). Nonlinear and equivalent linear site response analysis for the groningen area. Technical report, TNO.

[Qi and Gao, 2014] Qi, W.-G. and Gao, F.-P. (2014). Physical modeling of local scour development around a large-diameter monopile in combined waves and current. *Coastal Engineering*, 83:72–81.

[Ramirez et al., 2020] Ramirez, L., Fraile, D., and Brindley, G. (2020). Offshore wind in europe. key trends and statistics 2019. Technical report, Wind Europe.

[Schafhirt et al., 2016] Schafhirt, S., Page, A., Eiksund, G. R., and Muskulus, M. (2016). Influence of soil parameters on the fatigue lifetime of offshore wind turbines with monopile support structure. *Energy Procedia*, 94:347–356.

[Sobczyk et al., 2010] Sobczyk, K., Perros, K., and Papadimitriou, C. (2010). Fatigue reliability of multidimensional vibratory degrading systems under random loading. *Journal of Engineering Mechanics*, 136(2):179–188.

[Stockhert, 2015] Stockhert, F. (2015). *Fracture Mechanics applied to Hydraulic Fracturing in Laboratory Experiments*. PhD thesis, Ruhr University Bochum.

[van der Esch, 2020] van der Esch, I. (2020). Modelling the steady-state response of a soil column with nonlinear hysteretic damping under periodic excitation using a harmonic balance method. mathesis, TU Delft University of Technology.

[Versteijlen et al., 2018] Versteijlen, W., de Oliveira Barbosa, J., van Dalen, K., and Metrikine, A. (2018). Dynamic soil stiffness for foundation piles: Capturing 3d continuum effects in an effective, non-local 1d model. *International Journal of Solids and Structures*, 134:272–282.

[Versteijlen et al., 2011] Versteijlen, W., Metrikine, A., Hoving, J., Smid, E., and de Vries, W. (2011). Estimation of the vibration decrement of an offshore wind turbine support structure caused by its interaction with soil. *Knowledge, Technology and Policy*.

[Versteijlen et al., 2016] Versteijlen, W., Metrikine, A., and van Dalen, K. (2016). A method for identification of an effective winkler foundation for large-diameter offshore wind turbine support structures based on in-situ measured small-strain soil response and 3d modelling. *Engineering Structures*, 124:221–236.

[Versteijlen et al., 2017] Versteijlen, W., Renting, F., van der Valk, P., Bongers, J., van Dalen, K., and Metrikine, A. (2017). Effective soil-stiffness validation: Shaker excitation of an in-situ monopile foundation. *Soil Dynamics and Earthquake Engineering*, 102:241–262.

[Villalobos and Romanel, 2019] Villalobos, M. and Romanel, C. (2019). Seismic response of soft soil deposit using simplified models. *E3S Web of Conferences*, 92:16008.

[Wells, 2009] Wells, G. N. (2009). *The Finite Element Method: An Introduction*. University of Cambridge and Delft University of Technology.

[Wilson, 2000] Wilson, E. (2000). *Three dimensional static and dynamic analysis of structures : a physical approach with emphasis on earthquake engineering*. Computers and Structures, Berkeley, Calif.

[Wong et al., 1994a] Wong, C., Ni, Y., and Lau, S. (1994a). Steady-state oscillation of hysteretic differential model. i: Response analysis. *Journal of Engineering Mechanics*, 120(11):2271–2298.

[Wong et al., 1994b] Wong, C., Ni, Y., and Lau, S. (1994b). Steady-state oscillation of hysteretic differential model. ii: Performance analysis. *Journal of Engineering Mechanics*, 120(11):2299–2325.

[Yniesta and Brandenberg, 2015] Yniesta, S. and Brandenberg, S. (2015). Unloading-reloading rule for nonlinear site response analysis. In *6th International Conference on Earthquake Geotechnical Engineering*.

[Zhang et al., 2020] Zhang, J., Sulollari, E., Fărăgău, A. B., Pisanò, F., van der Male, P., Martinelli, M., Metrikine, A. V., and van Dalen, K. N. (2020). Harmonic balance method for the stationary response of finite and semi-infinite nonlinear dissipative continua: Three canonical problems. In *Advanced Structured Materials*, pages 255–274. Springer International Publishing.

[Zhang et al., 2021] Zhang, Y., Aamodt, K. K., and Kaynia, A. M. (2021). Hysteretic damping model for laterally loaded piles. *Marine Structures*, 76:102896.

Appendix A

Derivation of the Jacobian used for solving the Bouc-Wen model of hysteresis through AFTHBM

The derivation of the Jacobian is based on the procedure by [Wong et al., 1994a], but is rederived because of the different definition of the parameters of the Bouc-Wen model. Also, this Appendix shows the derivation steps. The discrete-time residual function of the Bouc-Wen element is:

$$\mathbf{r} = \dot{\mathbf{z}} - \dot{\mathbf{u}} \circ (\kappa - [\gamma + \beta \cdot sgn(\dot{\mathbf{u}}) \circ sgn(\mathbf{z})] \circ |\mathbf{z}|^{\circ n}) \tag{A.1}$$

Although the Jacobian $\hat{\mathbf{J}}$ has to be defined in the time domain. firstly the Jacobian $\mathbf{J}$ is calculated for each sample in the time domain. The chain rule of differentiation is used to split up the problem into 6 different derivatives:

$$\mathbf{J} = \frac{\delta \mathbf{r}}{\delta \hat{\mathbf{u}}} = \frac{\delta \mathbf{r}}{\delta \dot{\mathbf{u}}} \cdot \frac{\delta \dot{\mathbf{u}}}{\delta \hat{\mathbf{u}}} + \frac{\delta \mathbf{r}}{\delta \mathbf{z}} \cdot \frac{\delta \mathbf{z}}{\delta \hat{\mathbf{u}}} + \frac{\delta \mathbf{r}}{\delta \dot{\mathbf{z}}} \cdot \frac{\delta \dot{\mathbf{z}}}{\delta \hat{\mathbf{u}}} \tag{A.2}$$

By using mathematical software (Maple), the 3 derivatives related to the residual function are calculated:

$$\frac{\delta \mathbf{r}}{\delta \dot{\mathbf{u}}} = -\kappa + (\gamma + \beta \cdot sgn(\dot{\mathbf{u}}) \circ sgn(\mathbf{z})) \circ |\mathbf{z}|^n + \beta \cdot \dot{\mathbf{u}} \circ \frac{\delta}{\delta \dot{\mathbf{u}}}(sgn(\dot{\mathbf{u}})) \circ sgn(\mathbf{z}) \circ |\mathbf{z}|^n \tag{A.3}$$

$$\frac{\delta \mathbf{r}}{\delta \mathbf{z}} = \dot{\mathbf{u}} \circ \left(\beta \cdot sgn(\dot{\mathbf{u}}) \circ \frac{\delta}{\delta \mathbf{z}}(sgn(\mathbf{z})) \circ |\mathbf{z}|^{\circ n} + \frac{(\gamma + n \cdot \beta \cdot sgn(\dot{\mathbf{u}}) \circ sgn(\mathbf{z})) \circ |\mathbf{z}|^{\circ n} \circ \frac{\delta}{\delta \mathbf{z}}(|\mathbf{z}|)}{|\mathbf{z}|} \right) \tag{A.4}$$

$$\frac{\delta \mathbf{r}}{\delta \dot{\mathbf{z}}} = \mathbf{1} \tag{A.5}$$

where $\mathbf{1}$ is defined to be a vector with all ones.

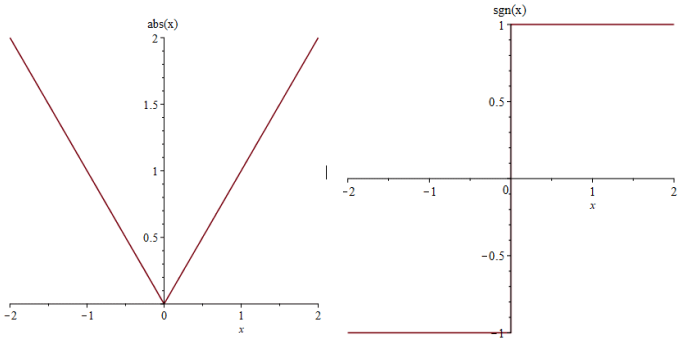

(a) Absolute function (b) Signum function

Figure A.1: Absolute function and the signum function.

Two functions of which a derivative is present in the equations are the absolute function and the signum function. Figure A.1 shows these functions. Both functions have a well-defined derivative, apart from an input value of 0. The derivative of the absolute function is the signum function (apart from x=0), and the derivative of the signum function is 0 (apart from x=0). To circumvent numerical issues at later stages, a value is assigned to x=0 (for both functions the derivative at x=0 is assigned as 0). The singularity at $\mathbf{z} = 0$ is also removed from Equation A.4 by simplifying the denominator, again to avoid numerical issues. These approximations simplify the derivatives of $\mathbf{r}$ to:

$$\frac{\delta \mathbf{r}}{\delta \dot{\mathbf{u}}} = -\kappa + (\gamma + \beta \cdot sgn(\dot{\mathbf{u}}) \circ sgn(\mathbf{z})) \circ |\mathbf{z}|^{\circ n} \tag{A.6}$$

$$\frac{\delta \mathbf{r}}{\delta \mathbf{z}} = \dot{\mathbf{u}} \circ \Big((\gamma + n \cdot \beta \cdot sgn(\dot{\mathbf{u}}) \circ sgn(\mathbf{z})) \circ |\mathbf{z}|^{\circ (n-1)} \circ sgn(\mathbf{z}) \Big) \tag{A.7}$$

$$\frac{\delta \mathbf{r}}{\delta \dot{\mathbf{z}}} = \mathbf{1} \tag{A.8}$$

The next derivative to solve is related to $\dot{\mathbf{u}}$. To find the derivatives of $\dot{\mathbf{u}}$ with respect to the state vector $\hat{\mathbf{u}}$, the Fourier representation of $\mathbf{u}$ is recalled. After taking a derivative with respect to time, the derivatives with respect to the state vector $\hat{\mathbf{u}}$ can be isolated:

$$\mathbf{u} = \sum_{\mathrm{k}=0}^{H} \hat{c}_{\mathrm{k}} cos(\mathrm{k}\Omega \mathbf{t}) + \hat{d}_{\mathrm{k}} sin(\mathrm{k}\Omega \mathbf{t}) \tag{A.9}$$

$$\frac{\delta \dot{\mathbf{u}}}{\delta \hat{c}_0} = \mathbf{0} \tag{A.10}$$

$$\frac{\delta \dot{\mathbf{u}}}{\delta \hat{c}_{\mathrm{k}}} = -\mathrm{k}\Omega sin(\mathrm{k}\Omega \cdot \mathbf{t}) \tag{A.11}$$

$$\frac{\delta \dot{\mathbf{u}}}{\delta \hat{d}_{\mathrm{k}}} = \mathrm{k}\Omega cos(\mathrm{k}\Omega \cdot \mathbf{t}) \tag{A.12}$$

where $\mathbf{0}$ is defined to be a vector with all zeros.

Next up, we take a look at the derivative with respect to $\mathbf{z}$. This derivative is split up into 2 parts. To find the derivatives of $\mathbf{z}$ with respect to the state vector $\hat{\mathbf{z}}$, the Fourier representation of $\mathbf{z}$ is recalled. The derivatives with respect to the state vector $\hat{\mathbf{z}}$ can be isolated:

$$\frac{\delta \mathbf{z}}{\delta \hat{\mathbf{u}}} = \frac{\delta \mathbf{z}}{\delta \hat{\mathbf{z}}} \cdot \frac{\delta \hat{\mathbf{z}}}{\delta \hat{\mathbf{u}}} \tag{A.13}$$

$$\mathbf{z} = \sum_{\mathrm{k}=0}^{H} \hat{p}_{\mathrm{k}} cos(\mathrm{k}\Omega \mathbf{t}) + \hat{q}_{\mathrm{k}} sin(\mathrm{k}\Omega \mathbf{t}) \tag{A.14}$$

$$\frac{\delta \mathbf{z}}{\delta \hat{p}_0} = \mathbf{1} \tag{A.15}$$

$$\frac{\delta \mathbf{z}}{\delta \hat{p}_{\mathrm{k}}} = cos(\mathrm{k}\Omega \cdot \mathbf{t}) \tag{A.16}$$

$$\frac{\delta \mathbf{z}}{\delta \hat{q}_{\mathrm{k}}} = sin(\mathrm{k}\Omega \cdot \mathbf{t}) \tag{A.17}$$

For the derivative of the state vector $\hat{\mathbf{z}}$ with respect to $\hat{\mathbf{u}}$, Equation 2.20 is recalled:

$$\hat{\mathbf{z}} = \left((1-\alpha)k_i \check{\nabla}^{\mathbf{0}}\right)^{-1} \cdot \left(\hat{\mathbf{f}}_{\mathbf{ex}} - \left(m\Omega^2 \check{\nabla}^{\mathbf{2}} + c\Omega \check{\nabla}^{\mathbf{1}} + k\check{\nabla}^{\mathbf{0}} + \alpha k_i \check{\nabla}^{\mathbf{0}}\right) \cdot \hat{\mathbf{u}}\right) \tag{A.18}$$

Taking the derivative with respect to $\hat{\mathbf{u}}$ creates the last part of $\frac{\delta \mathbf{z}}{\delta \hat{\mathbf{u}}}$:

$$\frac{\delta \hat{\mathbf{z}}}{\delta \hat{\mathbf{u}}} = \left((1-\alpha)k_i \check{\nabla}^{\mathbf{0}}\right)^{-1} \cdot \left(-\left(m\Omega^2 \check{\nabla}^{\mathbf{2}} + c\Omega \check{\nabla}^{\mathbf{1}} + k\check{\nabla}^{\mathbf{0}} + \alpha k_i \check{\nabla}^{\mathbf{0}}\right)\right) \tag{A.19}$$

The last derivative to find is related to $\dot{\mathbf{z}}$. A split of the derivative is again needed. To find the derivatives of $\dot{\mathbf{z}}$ with respect to the state vector $\hat{\mathbf{z}}$, the Fourier representation of $\mathbf{z}$ is recalled. After taking a derivative with respect to time, the derivatives with respect to the state vector $\hat{\mathbf{z}}$ can be isolated:

$$\frac{\delta \dot{\mathbf{z}}}{\delta \hat{\mathbf{u}}} = \frac{\delta \dot{\mathbf{z}}}{\delta \hat{\mathbf{z}}} \cdot \frac{\delta \hat{\mathbf{z}}}{\delta \hat{\mathbf{u}}} \tag{A.20}$$

$$\mathbf{z} = \sum_{\mathrm{k}=0}^{H} \hat{p}_{\mathrm{k}} cos(\mathrm{k}\Omega \mathbf{t}) + \hat{q}_{\mathrm{k}} sin(\mathrm{k}\Omega \mathbf{t}) \tag{A.21}$$

$$\frac{\delta \dot{\mathbf{z}}}{\delta \hat{p}_0} = \mathbf{0} \tag{A.22}$$

$$\frac{\delta \dot{\mathbf{z}}}{\delta \hat{p}_{\mathrm{k}}} = -\mathrm{k}\Omega sin(\mathrm{k}\Omega \cdot \mathbf{t}) \tag{A.23}$$

$$\frac{\delta \dot{\mathbf{z}}}{\delta \hat{q}_{\mathrm{k}}} = \mathrm{k}\Omega cos(\mathrm{k}\Omega \cdot \mathbf{t}) \tag{A.24}$$

Equation A.19 is reused to create the last part of $\frac{\delta \dot{\mathbf{z}}}{\delta \hat{\mathbf{u}}}$.

With all parts of $\mathbf{J}$ defined, the Jacobian can be transformed to the frequency domain. A custom DFT is used:

$$\frac{\delta \hat{v_0}}{\delta \hat{\mathbf{u}}} = \frac{1}{M} \cdot \mathbf{J}^T \cdot \mathbf{1} \tag{A.25}$$

$$\frac{\delta \hat{v_\mathrm{k}}}{\delta \hat{\mathbf{u}}} = \frac{2}{M} \cdot \mathbf{J}^T \cdot cos(\mathrm{k}\Omega\mathbf{t}) \tag{A.26}$$

$$\frac{\delta \hat{w_\mathrm{k}}}{\delta \hat{\mathbf{u}}} = \frac{2}{M} \cdot \mathbf{J}^T \cdot sin(\mathrm{k}\Omega\mathbf{t}) \tag{A.27}$$

Appendix B

Response spectra for all 6 simulations of the case study OWT under FLS conditions

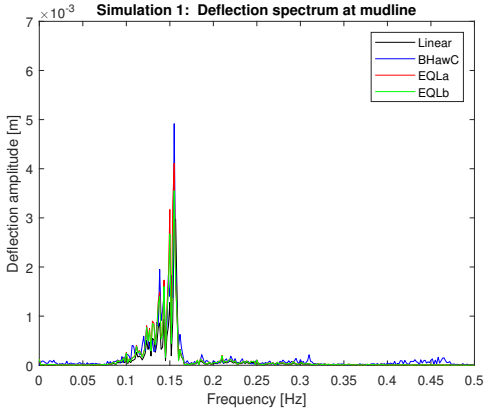

(a) 0-0.5 Hz

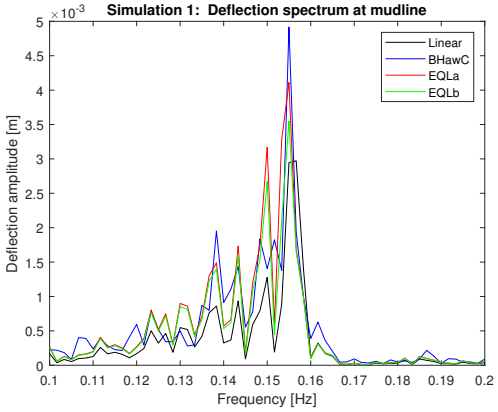

(b) 0.1-0.2 Hz

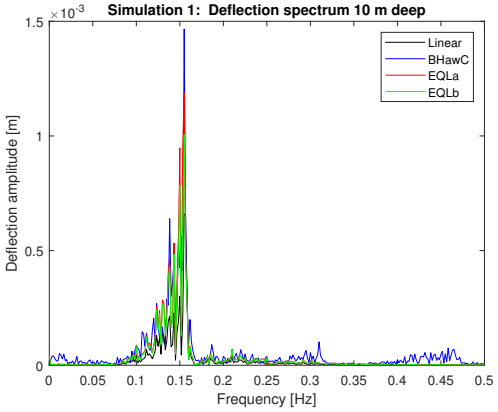

(c) 0-0.5 Hz

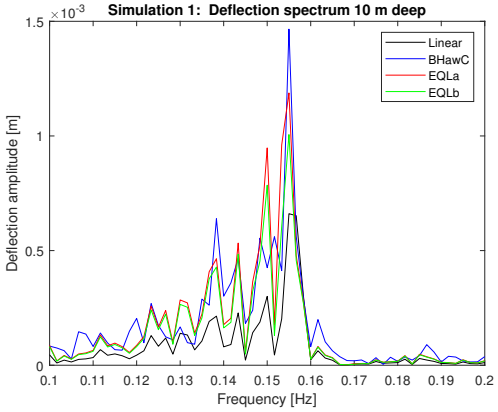

(d) 0.1-0.2 Hz

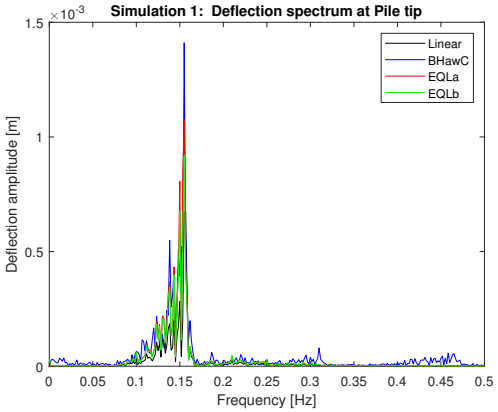

(e) 0-0.5 Hz

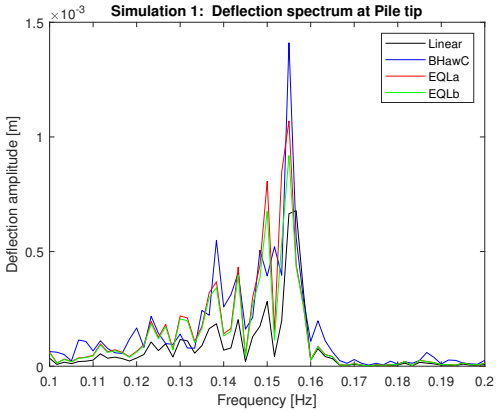

(f) 0.1-0.2 Hz

Figure B.1: Comparing deflection spectra in foundation. Simulation 1.

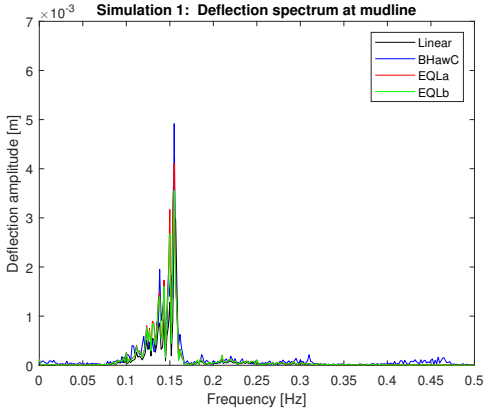

(a) 0-0.5 Hz

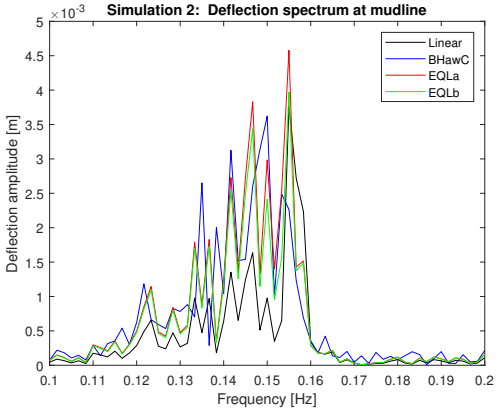

(b) 0.1-0.2 Hz

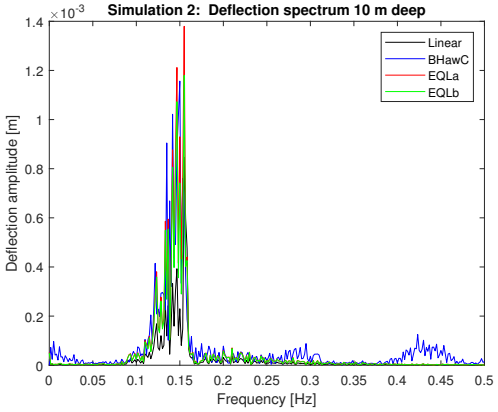

(c) 0-0.5 Hz

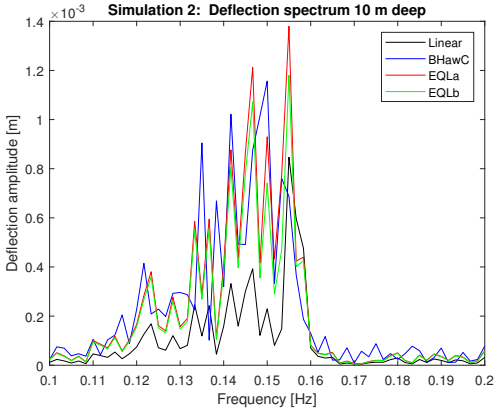

(d) 0.1-0.2 Hz

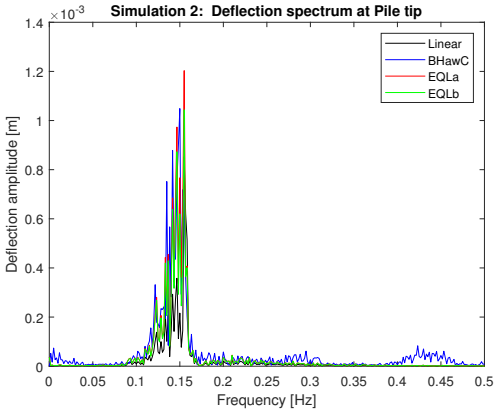

(e) 0-0.5 Hz

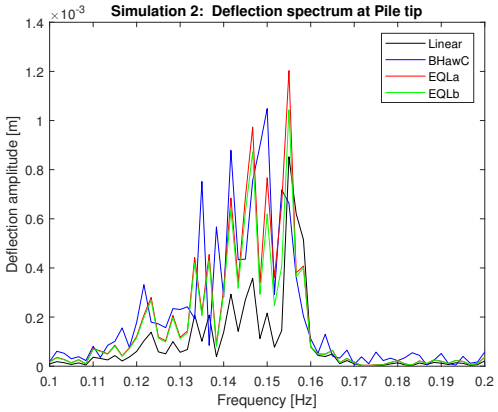

(f) 0.1-0.2 Hz

Figure B.2: Comparing deflection spectra in foundation. Simulation 2.

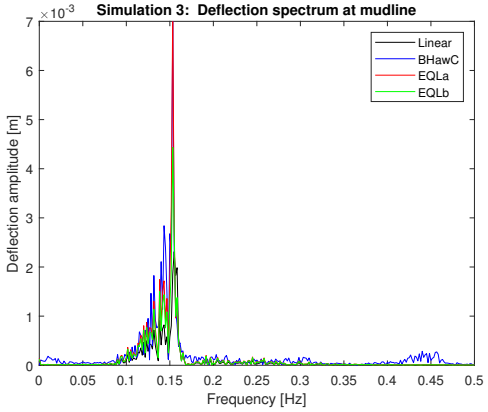

(a) 0-0.5 Hz

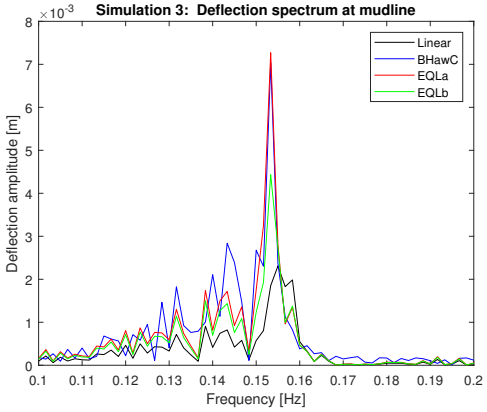

(b) 0.1-0.2 Hz

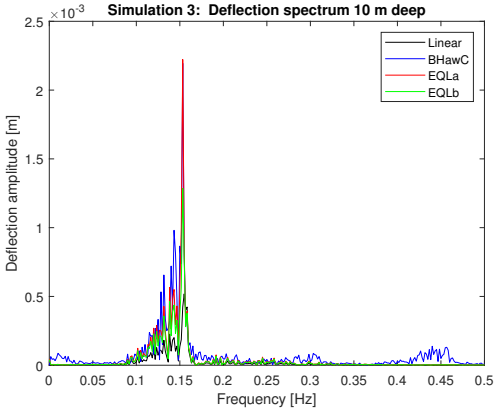

(c) 0-0.5 Hz

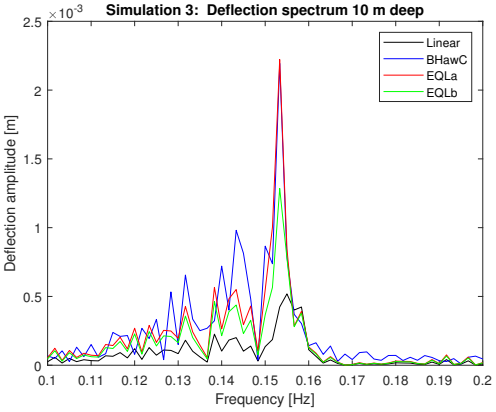

(d) 0.1-0.2 Hz

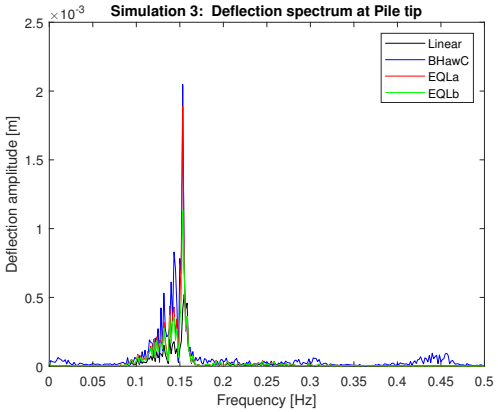

(e) 0-0.5 Hz

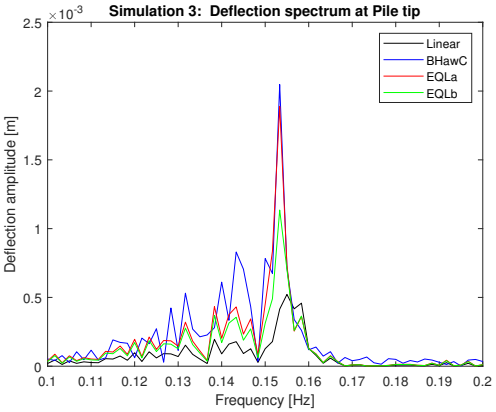

(f) 0.1-0.2 Hz

Figure B.3: Comparing deflection spectra in foundation. Simulation 3.

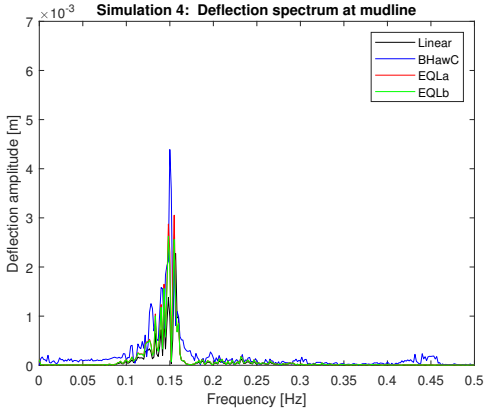

(a) 0-0.5 Hz

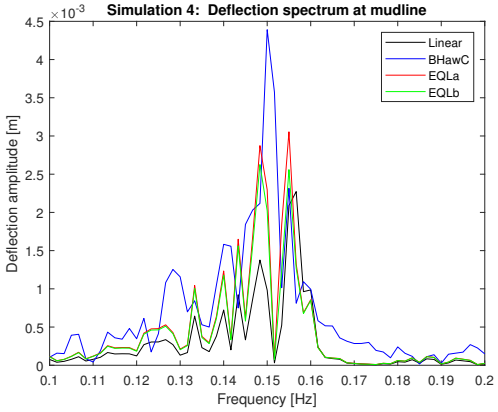

(b) 0.1-0.2 Hz

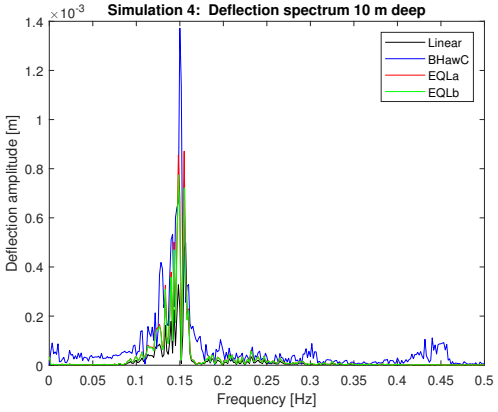

(c) 0-0.5 Hz

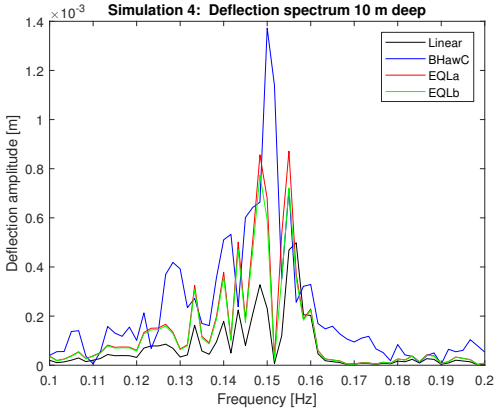

(d) 0.1-0.2 Hz

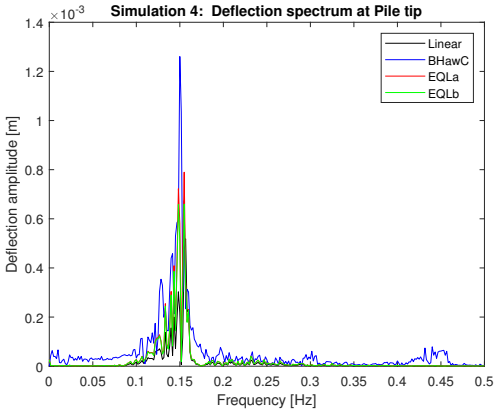

(e) 0-0.5 Hz

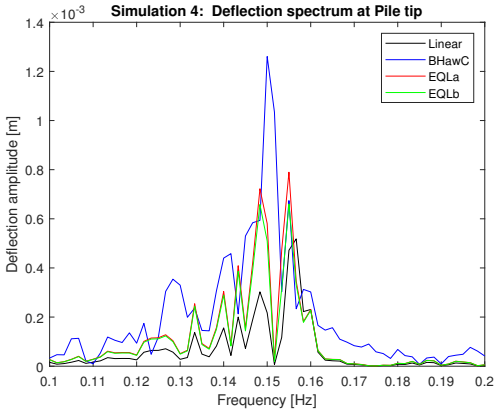

(f) 0.1-0.2 Hz

Figure B.4: Comparing deflection spectra in foundation. Simulation 4.

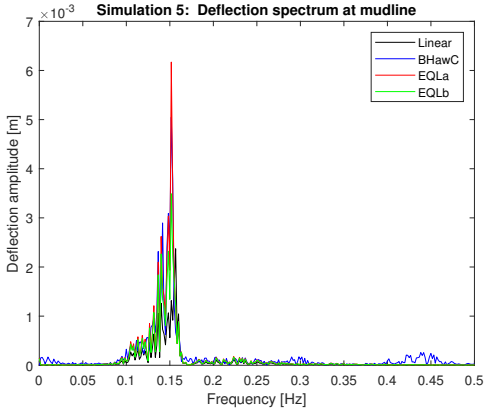

(a) 0-0.5 Hz

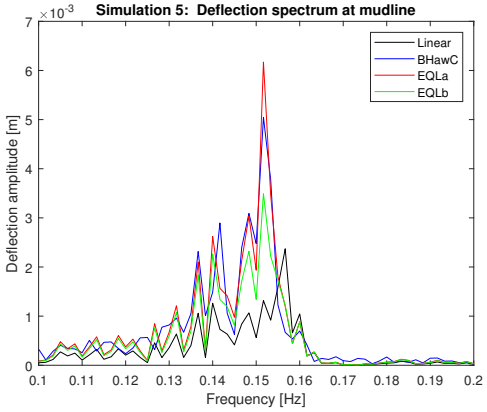

(b) 0.1-0.2 Hz

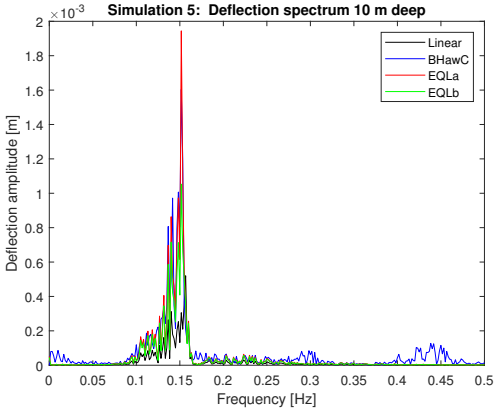

(c) 0-0.5 Hz

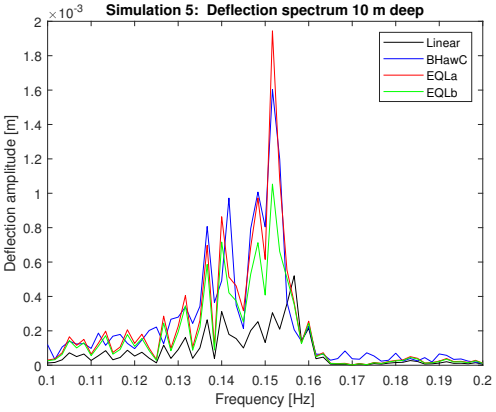

(d) 0-0.2 Hz

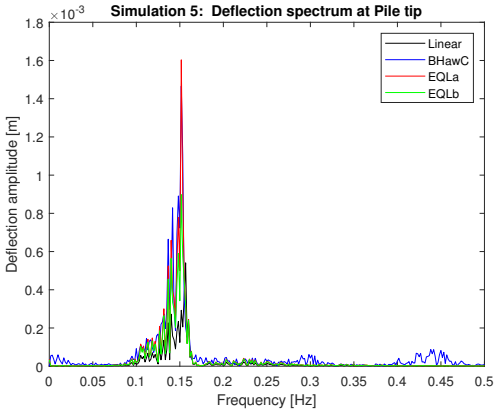

(e) 0-0.5 Hz

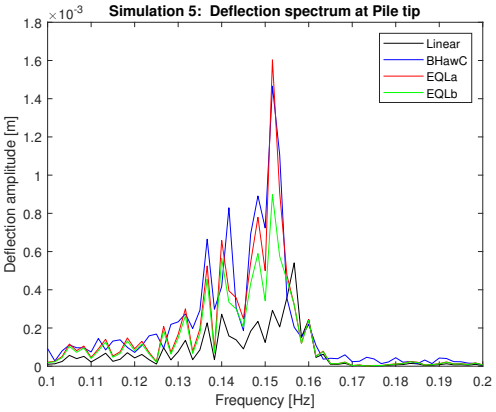

(f) 0-0.2 Hz

Figure B.5: Comparing deflection spectra in foundation. Simulation 5.

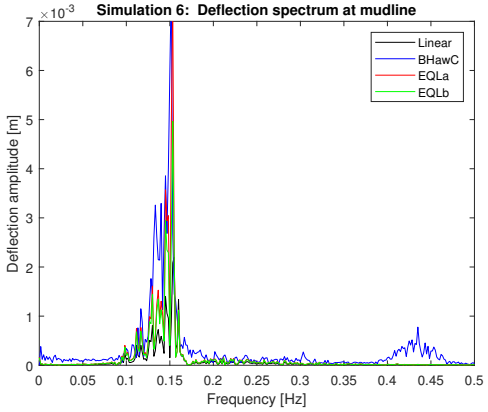

(a) 0-0.5 Hz

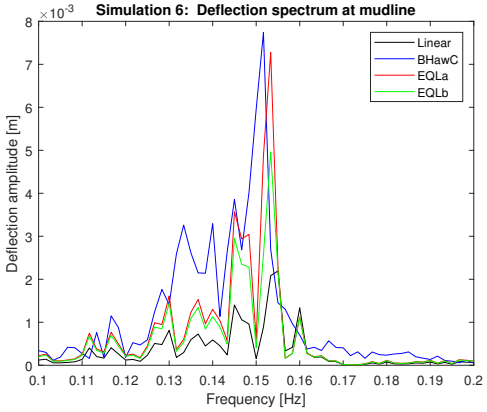

(b) 0.1-0.2 Hz

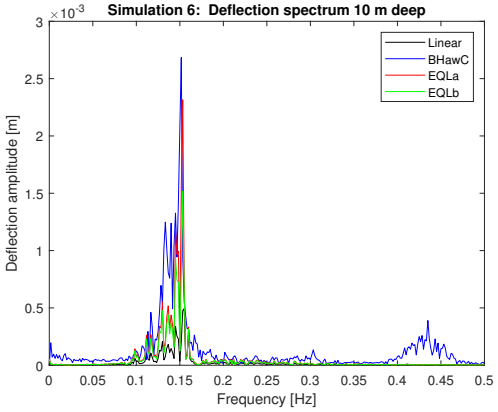

(c) 0-0.5 Hz

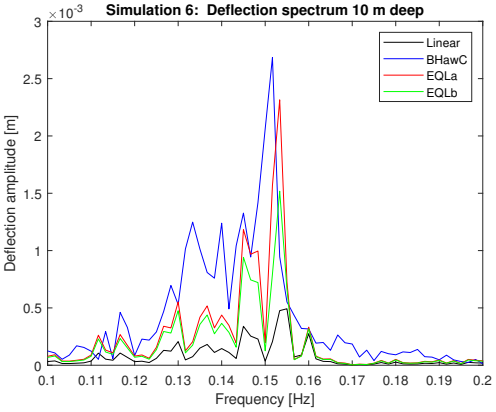

(d) 0.1-0.2 Hz

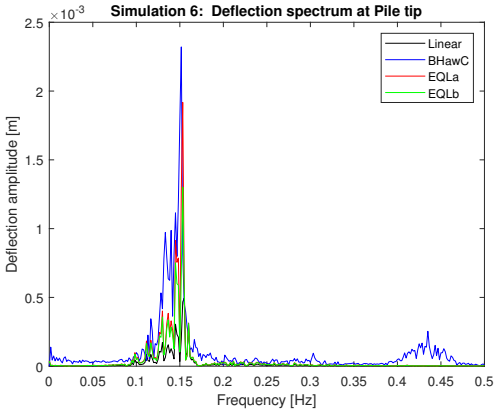

(e) 0-0.5 Hz

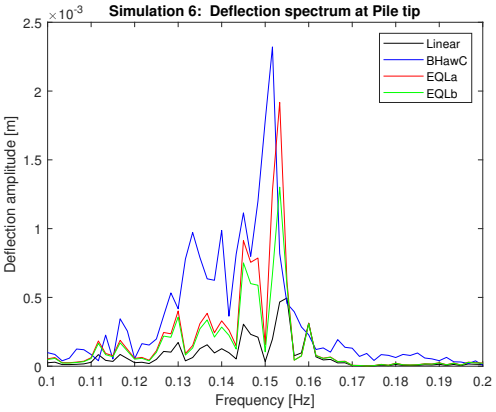

(f) 0.1-0.2 Hz

Figure B.6: Comparing deflection spectra in foundation. Simulation 6.